

(2) (42)

WT-1623(EX)  
EXTRACTED VERSION

## OPERATION HARDTACK—PROJECT 2.6

Neutron Flux from Very-High-Altitude Bursts

T. D. Hanscome, Project Officer  
P. B. Alers                      H. D. Holmgren  
P. A. Caldwell                E. C. Jones  
R. J. Drachman              C. A. Pearse  
S. G. Gorbics                R. C. Waddel  
Naval Research Laboratory  
Washington, DC

31 May 1961

### NOTICE:

This is an extract of WT-1623, Operation HARDTACK, Project 2.6.

Approved for public release;  
distribution is unlimited.

Extracted version prepared for  
Director  
DEFENSE NUCLEAR AGENCY  
Washington, DC 20305-1000

1 September 1985

DTIC  
ELECTRONIC  
MAR 14 1986  
E

86 3 13 010

AD-A995 383

DTIC FILE COPY

Destroy this report when it is no longer needed. Do not return to sender.

PLEASE NOTIFY THE DEFENSE NUCLEAR AGENCY,  
ATTN: STTI, WASHINGTON, DC 20305-1000, IF YOUR  
ADDRESS IS INCORRECT, IF YOU WISH IT DELETED  
FROM THE DISTRIBUTION LIST, OR IF THE ADDRESSEE  
IS NO LONGER EMPLOYED BY YOUR ORGANIZATION.



UNCLASSIFIED

SECURITY CLASSIFICATION OF THIS PAGE

AD A995383

REPORT DOCUMENTATION PAGE				Form Approved OMB No 0704 0188 Exp Date Jun 30, 1986	
1a REPORT SECURITY CLASSIFICATION UNCLASSIFIED			1b RESTRICTIVE MARKINGS		
2a SECURITY CLASSIFICATION AUTHORITY N/A since Unclassified			3 DISTRIBUTION AVAILABILITY OF REPORT Approved for public release; distribution is unlimited.		
2b DECLASSIFICATION/DOWNGRADING SCHEDULE N/A since Unclassified					
4 PERFORMING ORGANIZATION REPORT NUMBER(S)			5 MONITORING ORGANIZATION REPORT NUMBER(S) WT-1623(EX)		
6a NAME OF PERFORMING ORGANIZATION Naval Research Laboratory		6b OFFICE SYMBOL (If applicable)		7a NAME OF MONITORING ORGANIZATION Defense Atomic Support Agency	
6c ADDRESS (City, State, and ZIP Code) Washington, DC				7b ADDRESS (City, State, and ZIP Code) Washington, DC	
8a NAME OF FUNDING SPONSORING ORGANIZATION		8b OFFICE SYMBOL (If applicable)		9 PROCUREMENT INSTRUMENT IDENTIFICATION NUMBER	
8c ADDRESS (City, State, and ZIP Code)		10 SOURCE OF FUNDING NUMBERS			
		PROGRAM ELEMENT NO		PROJECT NO	TASK NO
					WORK UNIT ACCESSION NO
11 TITLE (Include Security Classification) OPERATION HARDTACK—PROJECT 2.6 Neutron Flux from Very-High-Altitude Bursts, Extracted Version					
12 PERSONAL AUTHOR(S) Hanscome, T.D.; Project Officer; Alers, P.B.; Caldwell, P.A.; Drachinan, R.J.; Gorbics, S.G.; Holmgren, H.D.; Jones, E.C.; Pearse, C.A.; and Waddel, R.C.					
13a TYPE OF REPORT		13b TIME COVERED FROM TO		14 DATE OF REPORT (Year, Month, Day) 610531	
				15 PAGE COUNT 97	
16 SUPPLEMENTARY NOTATION This report has had sensitive military information removed in order to provide an unclassified version for unlimited distribution. The work was performed by the Defense Nuclear Agency in support of the DoD Nuclear Test Personnel Review Program.					
17 COSATI CODES			18 SUBJECT TERMS (Continue on reverse if necessary and identify by block number)		
FIELD	GROUP	SUB-GROUP	HARDTACK Teak Shot		
18	3		Neutron Flux Orange Shot		
18	11		High Altitude Bursts		
19 ABSTRACT (Continue on reverse if necessary and identify by block number)					
<p>The primary objective of this project was to measure neutron flux and gamma-ray flux versus range and time from missileborne, megaton nuclear detonations at high altitudes by means of instrumented pods that were to be ejected, during the missile thrust period, at times that were selected to position the pods at predetermined distances from the burst.</p> <p>Specific objectives were: (1) neutron flux versus time was to be measured at each of three pod positions during each shot and (2) a measurement of gamma-ray dose rate versus time was sought from each pod during each shot.</p>					
20 DISTRIBUTION AVAILABILITY OF ABSTRACT <input checked="" type="checkbox"/> UNCLAS. SEC. UNLIMITED <input type="checkbox"/> SAME AS RPT <input type="checkbox"/> DTIC USERS			21 ABSTRACT SECURITY CLASSIFICATION UNCLASSIFIED		
22a NAME OF RESPONSIBLE INDIVIDUAL Mark D. Flohr			22b TELEPHONE (Include Area Code) (202) 325-7559		22c OFFICE SYMBOL DNA/ISCM

DD FORM 1473, 54 MAR

85 APR edition may be used until exhausted  
All other editions are obsoleteSECURITY CLASSIFICATION OF THIS PAGE  
UNCLASSIFIED

OPERATION HARDTACK—PROJECT 2.6

NEUTRON FLUX FROM VERY-HIGH-ALTITUDE BURSTS

T. D. Hanscome, Project Officer  
P. B. Alers            H. D. Holmgren  
P. A. Caldwell        E. C. Jones  
R. J. Drachman       C. A. Pearse  
S. G. Gorbics •       R. C. Waddel

U. S. Naval Research Laboratory  
Washington, D. C.

Accession For	
NTIS GRA&I	<input checked="checked" type="checkbox"/>
DTIC TAB	<input type="checkbox"/>
Unannounced	<input type="checkbox"/>
Justification	
By _____	
Distribution/	
Availability Codes	
Dist	Avail and/or Special
A-1	



UNANNOUNCED

## FOREWORD

Classified material has been removed in order to make the information available on an unclassified, open publication basis, to any interested parties. The effort to declassify this report has been accomplished specifically to support the Department of Defense Nuclear Test Personnel Review (NTPR) Program. The objective is to facilitate studies of the low levels of radiation received by some individuals during the atmospheric nuclear test program by making as much information as possible available to all interested parties.

The material which has been deleted is either currently classified as Restricted Data or Formerly Restricted Data under the provisions of the Atomic Energy Act of 1954 (as amended), or is National Security Information, or has been determined to be critical military information which could reveal system or equipment vulnerabilities and is, therefore, not appropriate for open publication.

The Defense Nuclear Agency (DNA) believes that though all classified material has been deleted, the report accurately portrays the contents of the original. DNA also believes that the deleted material is of little or no significance to studies into the amounts, or types, of radiation received by any individuals during the atmospheric nuclear test program.

## ABSTRACT

The primary objective was to measure neutron flux and gamma-ray flux versus range and time from missileborne, megaton nuclear detonations (Shots Orange and Teak) at high altitudes by means of instrumented pods that were to be ejected, during the missile thrust period, at times that were selected to position the pods at predetermined distances from the burst.

For each shot, a Redstone missile carried aloft along with three instrumentation pods that were ejected ballistically at predetermined times.

The neutron spectrum of the device was measured by the time-of-flight method. Plastic scintillators were used for measuring the fast-fusion neutrons;  $\text{Li}^6\text{I}$  scintillators, the slower, fission neutrons; normal  $\text{LiI}$  scintillators, the gamma-ray background;  $\text{CsI}$  scintillators, the prompt gamma-ray integral;  $\text{KBr}$  detectors, the integrated gamma-ray dose; and nonscintillator blanks, any interfering signals such as electromagnetic or gamma-ray background effects.

Neutron data was obtained from Pods 3 and 4 during Shot Teak and Pod 4 during Shot Orange, which were at slant ranges of 15.84, 53.74, and 29.45 km, respectively, at the times of detonation. The peak 14-Mev neutron flux rate at Teak Pod 3 was found

The measured flux of neutrons, with energies between 3 and 12 Mev, for Teak Pod 3 was

Similarly, the measured 3-to-12-Mev neutron flux at Teak Pod 4 was about and at Orange Pod 4 was

With a conversion factor of  $5.5 \times 10^{-8}$  rep/(n/cm<sup>2</sup>) for the 3-to-12-Mev region and with a relative biological effectiveness (RBE) factor of 10, the fast-neutron dose at Teak Pod 4 (22.8-km altitude) is found

and at Orange Pod 4 (20.01-km altitude) The altitudes of both of these pods are, of course, accessible to manned aircraft.

Total gamma doses from 0 to 12 msec were measured at Teak Pods 2, 3, and 4, respectively. Orange Pod 4 over the same time interval received a gamma-ray dose

Telemetry ( $\approx 240$  Mc) signal strengths of all pods were measured during their lifetimes.

The signal levels of Pods 4, for both shots, recovered to their preshot levels within 0.1 second after burst. The signals from Pods 2 and 3 were blacked out (fell below noise level) for approximately 45 seconds for Shot Teak and 20 seconds for Shot Orange.

## FOREWORD

This report presents the final results of one of the projects participating in the military-effect programs of Operation Hardtack. Overall information about this and the other military-effect projects can be obtained from ITR-1660, the "Summary Report of the Commander, Task Unit 3." This technical summary includes: (1) tables listing each detonation with its yield, type, environment, meteorological conditions, etc.; (2) maps showing shot locations; (3) discussions of results by programs; (4) summaries of objectives, procedures, results, etc., for all projects; and (5) a listing of project reports for the military-effect programs.

## PREFACE

The authors planned originally to participate in Shot Yucca (VHA-Project 2.7) only; however, the inclusion of Shots Teak and Orange led to the establishment of Project 2.6 using similar instrumentation techniques.

Personnel of the Nucleonics Division of the U. S. Naval Research Laboratory (NRL) planned the experiment, designed and produced most of the experimental equipment, and staffed the field project. The valuable assistance provided by the Instrumentation Branch of the Radiation Division of NRL (G. Wall, P. Schifflett, W. Weedman, G. Brotzman, and L. Bowles), which afforded the timely completion of the many printed circuits, is greatly appreciated. The pod mechanisms were designed and fabricated under the supervision of the Army Ballistic Missile Agency (ABMA). Assistance and advice on the use of the pods as instrument carriers are greatly appreciated.

The authors express their appreciation to the following individuals for discussions that were especially helpful in the planning and analysis phases of this experiment: to Drs. B. Watt and J. Malik of the Los Alamos Scientific Laboratory (LASL) for their very helpful comments with regard to possible effect and results; to Dr. G. Bing of the University of California Radiation Laboratory (UCRL) for discussions and information in connection with the neutron energy spectrum of the ; and to Dr. W. Biggers, LASL, who gave generously of his time in discussing the calculation of the air-scattering of neutrons using the Monte Carlo method.

The help of Mr. E. Cutler, NRL, with the many numerical computations in the final analysis of the neutron calculations, is greatly appreciated.

## CONTENTS

ABSTRACT .....	5
FOREWORD .....	6
PREFACE .....	6
CHAPTER 1 INTRODUCTION .....	11
1.1 Objectives .....	11
1.2 Historical and Experimental Background .....	11
1.3 Theory .....	12
CHAPTER 2 PROCEDURE .....	14
2.1 Operations .....	14
2.2 Instrumentation .....	14
2.2.1 Pods .....	14
2.2.2 Receiving Installations .....	14
2.2.3 System Calibration .....	14
2.2.4 Redundancy .....	15
2.3 Data Requirements .....	15
2.3.1 Reliability .....	15
2.3.2 Recording Methods .....	15
CHAPTER 3 RESULTS AND DISCUSSION .....	18
3.1 General Performance .....	18
3.2 Pod and Missile Trajectories .....	18
3.3 Estimate of Overall Success .....	19
3.4 Neutron Measurements .....	19
3.4.1 Experimental Results .....	19
3.4.2 Comparison with Theoretical Estimates .....	20
3.4.3 Neutron Dose at Altitudes Accessible to Manned Aircraft .....	21
3.5 Gamma-Ray Measurements .....	21
3.5.1 Gamma Radiation from Shot Teak .....	21
3.5.2 Gamma Radiation from Shot Orange .....	22
3.6 RF Attenuation .....	22
CHAPTER 4 CONCLUSIONS AND RECOMMENDATIONS .....	33
4.1 Conclusions .....	33
4.2 Recommendations .....	33
APPENDIX A THEORY .....	34
A.1 The Radiation Source .....	34
A.2 Transport of Neutrons to a Detector .....	34
A.3 Neutron-Scattering Calculations .....	35
A.3.1 Calculation of $K(E', T)$ Single Scattering .....	35
A.3.2 Multiple-Scattering Calculations .....	37



A.3.3 Comparison of the Results of the Single- and Multiple-scattering Calculations-----	40
A.3.4 Results of Scattering Calculations for Shot Yucca (Project 2.7)-----	40
APPENDIX B DETECTORS-----	47
B.1 Background-----	47
B.2 Calibration-----	48
B.3 Detector Configuration for Pods-----	49
APPENDIX C INSTRUMENTATION-----	51
C.1 Pods 2 and 3-----	51
C.1.1 CsI-----	51
C.1.2 Pilot B-----	51
C.1.3 Li <sup>6</sup> I-----	52
C.1.4 LiI-----	52
C.1.5 Blank Detector-----	52
C.2 Pod 4, Shot Teak-----	52
C.2.1 CsI, Detector 1-----	52
C.2.2 Pilot B, Detector 2-----	52
C.2.3 Pilot B, Detector 3-----	53
C.2.4 Pilot B, Detector 4-----	53
C.2.5 Blank, Detector 5-----	53
C.3 Pod 4, Shot Orange-----	53
C.4 General Design Techniques-----	53
C.5 Internal Timing for Detector Electronics-----	53
C.6 Internal Detector Program-----	54
C.7 Detector Data Outputs-----	54
C.8 Magnetic-Tape Recorder-----	55
C.9 Telemetry Transmitter-----	56
C.10 Pod Construction and Antenna System-----	56
C.11 Internal Power Supply-----	56
C.12 Receiving Antenna-----	57
C.13 Receiver-Discriminator System-----	57
C.14 Data-Reduction System-----	57
APPENDIX D CALIBRATION-----	87
D.1 Pod Calibration-----	87
D.1.1 Log-R Calibration-----	87
D.1.2 CsI Integrator Calibration-----	87
D.1.3 Pilot B, Detector 2B, Calibration for Total Dose in the Real-Time Channel-----	88
D.1.4 Pilot B, Detector 2B, Fast-Neutron Integral Channel-----	88
D.1.5 Pilot B, Detector 2B, Fast-Neutron Peak-Reader Calibration-----	88
D.1.6 Pilot B, Detector 2A, Calibration for the Radiation Time History PCO Channel-----	88
D.1.7 Pilot B, Detector 2A, Calibration for the Radiation Time History VCO Channel-----	88
D.1.8 Pilot B, Detector 2A, Fast-Neutron Analog Record Channel-----	88
D.1.9 Li <sup>6</sup> I, Detector 3, LiI, Detector 4, and Blank Detector 5-----	88
D.1.10 Potassium Bromide, Detector 6, Gamma-Ray Integral Channel-----	88
D.2 Recorder Calibration-----	88
D.2.1 VCO-Sensitivity Adjustment-----	88

D.2.2 VCO-Output-Signal-Amplitude Adjustment-----	89
D.2.3 Tape-Pressure-Pad Adjustment-----	89
D.2.4 Tape-Speed Adjustment-----	89
D.3 Data-Reduction Calibration-----	89
D.4 In-Flight System Checkout-----	89

REFERENCES-----	91
-----------------	----

#### TABLES

2.1 Actual Pod and Missile Positions at Burst-----	16
3.1 General Performance-----	23
3.2 Slant Ranges and Programed Gate Times-----	23
3.3 Results of Gamma-Ray Measurements, Shot Teak-----	23
A.1 Neutron Energy Spectrum-----	41
C.1 Planned Internal Program Time Intervals-----	58
D.1 Graphing Points for Log-R Calibration-----	89

#### FIGURES

2.1 Instrumented pod with center shell removed-----	17
3.1 Pod and missile trajectories for Shot Teak-----	24
3.2 Pod and missile trajectories for Shot Orange-----	24
3.3 Pilot-B detector current from Pod 3, Shot Teak-----	25
3.4 LII detector current from Pod 3, Shot Teak-----	25
3.5 Pilot-B detector current from Pod 4, Shot Teak-----	26
3.6 Pilot-B detector current from Pod 4, Shot Orange-----	26
3.7 Neutron flux rate versus time as measured with Pilot-B and LII detectors at Pod 3, Shot Teak-----	27
3.8 Composite measured neutron flux rate versus time at Pod 3, Shot Teak, compared with calculated values for the same position-----	27
3.9 Measured detector currents due to neutrons at Pod 4, Shot Teak, compared with calculated values-----	28
3.10 Measured detector currents due to neutrons at Pod 4, Shot Orange, compared with calculated values-----	28
3.11 Antenna pattern and pod positions at time of burst, Shot Teak-----	29
3.12 Antenna pattern and pod positions at time of burst, Shot Orange-----	29
3.13 Early time signal strength, Shot Teak-----	30
3.14 Early time signal strength, Shot Orange-----	30
3.15 Signal strength versus time for the lifetimes of the pods, Shot Teak-----	31
3.16 Signal strength versus time for the lifetimes of the pods, Shot Orange-----	32
A.1 Neutron energy spectrum-----	42
A.2 Single-scattering calculation geometry-----	42
A.3 Ratio of currents due to singly scattered and direct 14-Mev neutrons versus time for Pod 3, Shot Teak-----	43
A.4 Ratio of currents due to singly scattered and direct 14-Mev neutrons versus time for Pod 4, Shot Teak-----	43
A.5 Detector current due to scattered neutrons at Pod 4, Shot Teak-----	44
A.6 Detector current due to scattered neutrons at Pod 4, Shot Orange-----	44
A.7 Comparison of the results of the single- with the multiple-scattering calculations-----	45
A.8 Detector current due to indirect neutron flux-----	45
A.9 Detector current due to direct neutron flux-----	46
A.10 Ratio of indirect to direct detector currents-----	46

B.1 Calibration curves for L11, L1 <sup>1</sup> , and Pilot B	50
B.2 Calibration curve for KBr detector	50
C.1 Detector electronics, Pods 2 and 3, Shots Teak and Orange	59
C.2 Detector electronics, Pod 4, Shot Teak	60
C.3 Detector electronics, Pod 4, Shot Orange	61
C.4 Detector cathode follower	62
C.5 Signal limiter	63
C.6 Log-R circuit	64
C.7 Peak reader (normally open)	65
C.8 Peak reader (normally closed)	66
C.9 Integrate-and-hold circuit	67
C.10 Timing circuit	68
C.11 Mixer-gate circuit	69
C.12 PCO circuit, low frequency	70
C.13 PCO circuit, high frequency	71
C.14 Calibrator circuit	72
C.15 Voltage regulator	73
C.16 Log-R chassis	75
C.17 PCO chassis, high frequency	75
C.18 Timer chassis	76
C.19 Timer chassis	76
C.20 Peak reader	77
C.21 Peak-reader-and-hold chassis	77
C.22 Integrate-and-hold chassis	78
C.23 Detector cathode follower	79
C.24 Pod chassis rack	79
C.25 Pod chassis rack	80
C.26 Completed pod racks, front	81
C.27 Completed pod racks, rear	81
C.28 Definitions of timing values	82
C.29 Block diagram of a frequency channel, shown in record mode	83
C.30 Block diagram of an amplitude channel in record mode	84
C.31 Block diagram of transfer channel	84
C.32 Vertical field pattern for four-turn helical telemetering antenna	85
C.33 Horizontal field pattern for four-turn helical telemetering antenna	85
C.34 Block diagram of receiving station	86
D.1 Calibration equipment	90
D.2 Log-R calibration curve	90

## Chapter 1

### INTRODUCTION

#### 1.1 OBJECTIVES

The primary objective was to measure neutron flux and gamma-ray flux versus range and time from missileborne, megaton nuclear detonations (Shots Orange and Teak) at high altitudes by means of instrumented pods that were to be ejected, during the missile thrust period, at times that were selected to position the pods at predetermined distances from the burst.

Specific objectives were as follows:

1. Neutron flux versus time was to be measured at each of three pod positions during each shot. The two upper pods (Pods 2 and 3) in each case were to be close enough to the burst points (Orange  $\approx 100,000$  feet and Teak  $\approx 250,000$  feet) to be essentially free of atmospheric scattering effects. The lower pods (Pods 4) were to be at altitudes accessible to manned aircraft. Neutron time-of-flight techniques could be used on the neutron-versus-time data from the upper two pods to obtain the neutron energy spectrum of the device. In the case of the lower pods, atmospheric scattering would be appreciable and time-of-flight techniques would be possible only during times which are comparable with the time of arrival of the 14-Mev neutrons. At later times the lower pods were to be used only to obtain information about the neutron dose rate.
2. A measurement of gamma-ray dose rate versus time was sought from each pod during each shot. Provisions were made for measurement of the integral gamma-ray dose received before the arrival of the 14-Mev neutrons, the integral dose occurring within the first 120 msec, and the dose rate versus time from the time of gamma-ray arrival until the pods fell into the sea. Detectors with similar gamma-ray sensitivity but with different neutron sensitivities were included in order to separate gamma-ray and neutron effects.

#### 1.2 HISTORICAL AND EXPERIMENTAL BACKGROUND

Early predictions of the effects of nuclear weapons detonated at high altitudes resulted in the high-altitude (HA) shot during Operation Teapot (Reference 1). Further studies and calculations showed the feasibility and the desirability of testing large-yield devices at higher altitudes (References 2 and 3). The plans for Shots Teak and Orange resulted from service requirements based on estimates of military effectiveness of high-altitude detonations.

Although only a small part of the energy of a nuclear detonation appears as nuclear radiation, the low atmospheric density at high altitudes permits both gamma rays and neutrons to penetrate great distances. The effects of the neutron flux will be substantial at altitudes now accessible to manned aircraft. Although theoretical estimates (References 1, 2, and 3) have been made of these effects, it was desirable to make measurements to provide check points and to give confidence in the calculations.

Because the information from the pods was to be telemetered to a ground station, it was necessary to consider the effects of the detonation on the transmission path. If the period during which the transmission is blacked out extends beyond the time of arrival of the 14-Mev neutron component, it is necessary to delay the transmission until blackout recovery.

From the telemetry records of the shock and blast information during the HA shot of Operation Teapot, the ionization produced by the nuclear and thermal radiation absorbed the signal from the closest canister for a substantial period of time (References 4 and 5). Early feasibility studies for testing nuclear devices at high altitudes (Reference 2) included a consideration of the effects of ionization on radio wave propagation. The magnitude and duration of attenuation were calculated on the basis of three-body recombination and on estimated values of the collision frequency. However, because this calculation did not consider three-body attachment of electrons to oxygen molecules, it was inadequate for estimation of blackout duration.

Project 6.6 of Operation Redwing (Reference 6) made a measurement of radio wave attenuation versus time, with 1- $\mu$ sec resolution, along a radial path at sea level. The analysis of the results of this measurement, utilizing results of recent measurements of the three-body electron attachment coefficient (Reference 7), indicated an electron removal time of from 1 to 5 shakes (1 shake =  $10^{-8}$  second). The essential uncertainty in this value is due to the uncertainty involved in scaling the gamma-ray output of nuclear devices with yield.

Project 2.7 of Operation Plumbbob (Reference 8) was established to gain information on radiation-detector design, which would be valuable in the development of detectors for the present project and to field-test telemetry equipment in nuclear radiation environments. Measurements of attenuation versus time were made simultaneously with gamma-ray measurements, in order to remove gamma-ray scaling uncertainties in the deduced value for the electron removal times.

From considerations that can be found in Reference 6, it was shown that the measured attenuation at sea level could be accounted for by assuming that electrons, after having been thermalized, are removed by three-body attachment to oxygen molecules. Because this is a three-body removal process, the electron removal rate is proportional to the square of the pressure. In the worst possible case—the telemetry link from the upper pod—the blackout time can be estimated as follows. The ratio of the pressures between sea level and 65 km (the altitude of the upper pod was  $\sim 67$  km) is  $0.67 \times 10^4$ . If the removal time as found in the Redwing and Plumbbob data is multiplied by the square of this ratio, the electron removal time at 65 km is about 1.4 second. Consequently, the blackout period could be of the order of seconds, and it was therefore necessary for each pod to contain a data-storage system that could record the data and read it out after blackout recovery.

### 1.3 THEORY

The high altitudes chosen for Shots Teak and Orange made the use of time-of-flight techniques feasible for measuring the neutron energy spectrum of the device. Under these circumstances, it can be assumed that the neutrons from the device are emitted in a time period that is short compared with the time required for them to reach the detectors. Then the transit time ( $\tau$ ) from the device to a detector for an unscattered neutron of energy  $E$  is,

$$\tau = l(m/2E)^{1/2} \quad (1.1)$$

Where:  $l$  = distance of detector from the device  
 $m$  = the mass of a neutron

If scattering is neglected and  $dN(E)/dE$  is the number of neutrons emitted from the source per unit energy range and into unit solid angle, then the number of neutrons that arrive at the location of the detector per unit time per unit solid angle is given by

$$\frac{dN(T)}{dT} = \frac{dN(E)}{dE} \frac{l^3 m}{\tau^3} = \frac{dN(E)}{dE} \frac{(2E)^{3/2}}{lm^{3/2}} \quad (1.2)$$

Because the measured quantity in this experiment is  $N(\tau)$ , the energy spectrum of the device,  $N(E)$ , can be found.

The fiducial marker, relative to which neutron arrival times ( $T$ ) are measured, was chosen to be the arrival at a pod of the prompt gamma-ray pulse. If the distance ( $l$ ) from a pod to the

burst point is known, the neutron transit time ( $\tau$ ) is

$$\tau = T + l/c \quad (1.3)$$

where  $c$  is the velocity of light.

A complication in the interpretation of the measurement arises from the detection of scattered neutrons that arrive at times not simply related to their energies. In order to estimate the fraction of the total signal from the neutron detectors due to scattering effects, it was necessary to perform a Monte Carlo calculation of the intensity of scattered neutrons as a function of time. A description of this program and a summary of the results are given in Appendix A.

The interpretation of the experimental results is further complicated by the fact that the efficiency of a detector is a function of neutron energy. Because of this, a basic part of the calibration of the neutron detectors was a measurement of the sensitivity as a function of neutron energy. The results of this calibration are given in Appendix B.

The high-frequency response requirements of the data-handling systems are dictated by the rise time of the 14-Mev neutron pulse at the detectors. This group of neutrons, which are a product of the  $H^3(d,n)He^4$  reaction, have an energy width due to the nuclear temperature of the reacting mass (References 9, 10, and 11). The half width at half maximum of the 14-Mev neutron distribution function is shown in Reference 11 to be given in Mev by  $\Delta E = 5.59 \sqrt{kT}$ , where  $kT$  is a measure of the nuclear temperature. If it is assumed that  $kT =$  for the device, the rise times of the 14-Mev signal at the different pods vary from at the uppermost pod to at the lowest pod.

## Chapter 2

### PROCEDURE

#### 2.1 OPERATIONS

Field equipment installations were planned for operational readiness on 15 July 1958. Operations in the field were closely coordinated with those of the Army Ballistic Missile Agency (ABMA). One of three instrumentation vans was located near the ABMA bunker and contained support materials and instruments for the telemetry receiving station. This van was also used to develop telemetry records. The receiving station facilities, supplied and operated by the Cooper Development Corporation, were installed within the blockhouse. The other two vans contained the pod-checkout equipment and were located at a special ramp north of the launching site. On the ramp between the two vans, an insulated, air-conditioned Butler building was built by project personnel. The pods were delivered to the field with the Redstone shipments and were prepared for use in the Butler building.

Four pods were carried aloft by a Redstone missile for each shot. On both shots, Pod 1 (closest to the detonation) was allocated to Project 8.6 for X-ray studies. Pods 2, 3, and 4 were used by Project 2.6 for nuclear radiation measurements. Table 2.1 contains the positions at burst times of the pods and missiles for Shots Teak and Orange.

#### 2.2 INSTRUMENTATION

The instrumentation in the pods consisted of detectors, a tape recorder, a commutator, a telemetry transmitter, and electronic circuits to encode the detector signals. Mechanical commutation was required to transmit the eight channels of magnetic-tape information in sequence. Electronic gating was used to record the portions of the signal for which each detector was designed. Appendix B describes the detector design and gives the signal levels to be expected. Appendix C describes the general instrumentation.

**2.2.1 Pods.** For both Teak and Orange, Pods 2 and 3, the near pods, were similar except for time constants. Pod 4, the far pod, during both shots had circuitry similar to the near pods, but was used differently because of the interference by scattered neutrons and late gamma rays from neutron interactions in the atmosphere. Eleven pods were supplied; three for Teak, three for Orange, and five spares. Two of the spares were not completely instrumented, but were so prepared that they could be adapted for use as either far or near pods by an appropriate choice of instrumentation in the field. An instrumented pod, with the center skin section removed, is shown in Figure 2.1.

**2.2.2 Receiving Installations.** The telemetry receiving facilities consisted of four operating receivers, a tape recorder, six oscilloscopes with recording cameras, data-reduction equipment, and oscillographs. Details of this system are given in Appendix C.

**2.2.3 System Calibration.** The detectors were calibrated in advance at the Naval Research Laboratory (NRL). Additional field calibration checks were made with a 5-curie polonium-beryllium neutron source and a 5-curie  $\text{Co}^{60}$  gamma-ray source. These calibrations, described in Appendix B, were used to convert detector currents to neutron flux and gamma-ray flux.



Calibration checks of all pod circuitry and receiver links were made in the field during the preparation phase (Appendix D). During the period between pod ejection and detonation time, a series of internally programed calibration signals were transmitted in order to check the calibration and the in-flight operation.

**2.2.4 Redundancy.** Redundant information channels are frequently added to telemetry systems to increase the probability of obtaining data. Channels are also frequently duplicated to increase the dynamic range. In the pods used during Operation Hardtack the number of channels was severely restricted by space and weight limitations. Some of the advantages of redundancy were gained by use of channel time sharing, by coding information in two or more ways, by direct recording of data, and by using detectors for primary and secondary purposes, e.g., the Pilot-B detector measured 14-Mev neutrons and prompt gamma rays. The use of more than one pod at each shot was the only redundancy that could be provided against system failure, such as power supply failure or failure of the internal pod program. This redundancy was available to a certain extent for Pods 2 and 3 on each shot, because scattering conditions were similar.

### 2.3 DATA REQUIREMENTS

**2.3.1 Reliability.** The first briefing received by Project 2.6 personnel concerning the possibilities of Teak and Orange shots was in February 1957. During the following weeks the project became established, and in April 1957, it was proposed that neutron flux be measured by time-of-flight methods, assuming that the instrumentation stations would be near the detonation and that atmospheric scattering would be negligible. Interest in neutron effects in the lower atmosphere, which grew out of the calculations in Reference 3, originally prompted the placement of two instrumented pods at altitudes accessible to manned aircraft. However, because a pod was transferred to Project 8.6 for use in an X-ray experiment, only Pod 4 remained for this service. The time-of-flight analysis of far-pod neutron data becomes somewhat complicated because of atmospheric scattering.

Data requirements fell into two groups: (1) those resulting from the original proposal for near stations (Pods 2 and 3) and (2) those for the far stations (Pod 4). For the former, the objective remained to measure the neutron energy spectrum by the time-of-flight method and the neutron flux as a function of time. The chief design problems involved the choice of appropriate sensitivities and dynamic ranges. This requirement made it imperative that good estimates of expected fluxes be made, channels with overlapping sensitivities be used, and a signal compression system be employed. Estimates of the expected signal are found in Appendix A. Because of weight and space limitations, the number of channels of overlapping sensitivity had to be kept to a minimum. Signal compression was obtained by the use of logarithmic load resistors on the detectors (Appendix C).

Complexities in the expected neutron signals for the far pods were such that no plans were made for a time-of-flight analysis of the whole spectrum. Because the scattering calculations (Appendix A) showed that the 14-Mev neutron signal would not be greatly complicated by scattered neutrons, this group could be measured and analyzed. At later times, the signal from scattered neutrons becomes comparable with the direct neutron signal, hence only dose measurements could be made.

Data required from ABMA consisted of predictions of pod locations at time zero, to  $\pm 10$  percent and postshot determinations of the actual locations of the pods to  $\pm 5$  percent.

**2.3.2 Recording Methods.** The standard telemetry transmitters in the pods were used in a nontypical fashion. Slow data (narrow band width) were transmitted on standard Research and Development Board (RDB) subcarriers of an FM/FM system and were recorded on an Ampex tape recorder in the receiver station. The data were analyzed with standard discriminators and plotted with an oscillograph. Rapidly varying signals (wide band width) frequency-modulated the transmitter directly. This information was presented on oscilloscopes and was photographed



with moving-film cameras. A third type of signal amplitude-modulated the transmitter 30 percent. This signal was extracted from the IF amplifier of the receiver, ahead of the discriminator, and was then amplified further, detected, and recorded with an oscillograph.

TABLE 2.1 ACTUAL POD AND MISSILE POSITIONS AT BURST

The origin for the coordinate system is the missile launch point.  
The coordinates and slant ranges are in kilometers.

Missiles and Pods	South	Altitude	West	Slant Range*
Teak missile	-0.97	76.31	0.69	—
Teak 2	-1.26	66.26	1.24	10.07
Teak 3	-0.61	60.47	1.18	15.84
Teak 4	-0.95	22.80	0.34	53.74
Orange missile	41.69	42.93	0.93	—
Orange 2	35.30	35.75	0.95	9.64
Orange 3	32.55	31.37	0.88	14.77
Orange 4	23.27	20.01	0.25	29.45

\* Slant range is with respect to the burst point.

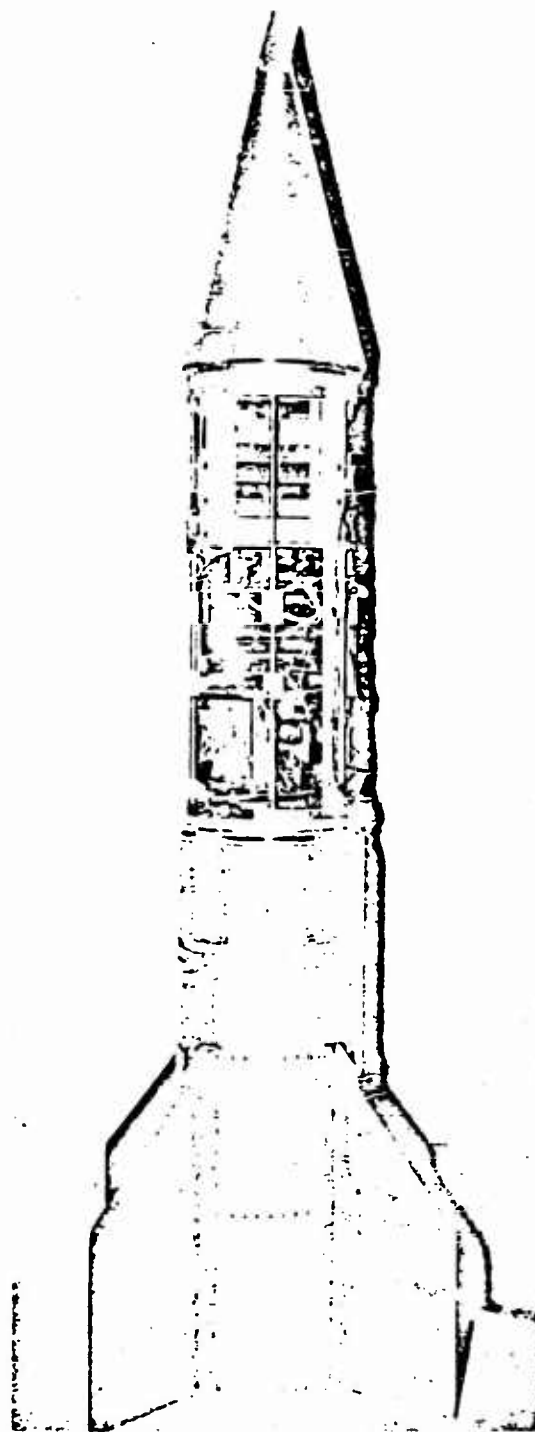


Figure 2.1 Instrumented pod with center shell removed.

## Chapter 3

### RESULTS AND DISCUSSION

#### 3.1 GENERAL PERFORMANCE

Telemetry signals were received from all six pods after the initial blackout period, and the signal strength as a function of time was recorded for each pod at the ground station. Because the signal channels that were to record the 14-Mev pulse shape contained only large uninterpretable fluctuations, useful 14-Mev pulse-shape information was not obtained from any pod. This failure may have been due to the fact that the 14-Mev neutron pulse was strongly reduced because of the marginal high-frequency response of the tape recorders, causing the signal to be obscured.

In general, the requirements for the measurement of gamma-ray intensities as a function of time were not met. The exact reasons for the loss of early (0 to 120 msec) gamma-ray time history are unknown, but may be attributed in part to excessive leakage currents, due to ionization, in the detector systems and to a malfunction of the high-frequency telemetry subcarriers. The failure of the late gamma-ray time history (120 msec to several seconds) was apparently due to lack of sensitivity. However, measurements of the integral of the gamma-ray intensity were made over three time intervals, and from these measurements, a coarse gamma-ray time history up to 120 msec can be constructed.

The remaining attempted measurements met with varying degrees of success as shown in Table 3.1.

With the exception of the general failures discussed above, Pods 3 and 4 during Shot Teak and Pod 4 during Shot Orange performed satisfactorily, and the data from these pods constitutes the major portion of the experimental results.

An apparent failure of the high-voltage supply in Pod 2 during Shot Teak caused the loss of all data dependent upon detectors which required this voltage; however, the KBr detector performed satisfactorily, because it did not require a high-voltage supply.

Pod 2 during Shot Orange yielded signals that indicated that it performed successfully, but large variations in the speed of the tape recorder made it impossible to recover any useful data.

The signals received from Pod 3 during Shot Orange indicated that the initiating trigger pulse was absent or ineffective; consequently, the pod remained in its preshot condition. Because the erase head was not disabled, any information that might have been recorded in this pod was immediately erased.

#### 3.2 POD AND MISSILE TRAJECTORIES

The pod and missile trajectories for Shot Teak are shown in Figure 3.1 and for Shot Orange in Figure 3.2. The numbers shown are times (in seconds) after launch. These trajectories are constructed from data taken from Chrysler Corporation Technical Reports AME-M48 and AME-M46.

A failure of the tilt program of the missile for Shot Teak caused it to have a nearly vertical trajectory and to place the instrumented pods almost directly to the rear of the warhead. However, the error introduced by this failure in the slant ranges of the pods was small enough that the arrival times of the 14-Mev neutron group fell within the programmed gate times. This failure caused a reduction in the radiation intensities at the pods, because it placed the rear compartment of the warhead between the device and the detectors.

From the point of view of this experiment, the missile for Shot Orange performed quite satisfactorily except for the incorrect placement of Pod 4 relative to the burst point. A malfunction in the vertical-guidance system caused the missile and Pods 2 and 3 to attain higher altitudes than had been predicted. However, because the ejection times of these pods were determined by the engine cutoff time, their positions relative to the burst were within the design tolerances of the pods' internal timing sequence and the gate width.

Because the ejection of Pod 4 was determined by a preset timer and did not depend on the engine cutoff time, the malfunction of the vertical-guidance system caused an error in the slant range; as a result, the 14-Mev neutron arrival time occurred after the gate had closed.

Table 3.2 lists the slant range between each pod and the burst point and the programed gate times for each pod.

### 3.3 ESTIMATE OF OVERALL SUCCESS

The overall success of this project is greater than may be indicated in Table 3.1, because the use of three pods at each shot gave a reasonably high degree of redundancy to the measurements. The two upper pods (2 and 3) at each shot were placed at ranges and altitudes that would make atmospheric scattering effects negligibly small, thereby allowing the neutron spectrum of the device to be deduced directly from the experimental data. One of these four high pods yielded neutron information sufficiently complete so that the objectives of the close-in measurement were met. It was expected that the neutron data from Pod 4 for each shot would not be useful in deducing the neutron spectrum of the device, because of the significant amount of neutron scattering caused by atmosphere between the detectors and the source, but it would nevertheless yield useful information about total neutron doses at altitudes accessible to manned aircraft. The data from these lower pods has been compared with the calculated detector currents, due to both direct and scattered neutrons, and was found to be in reasonable agreement.

### 3.4 NEUTRON MEASUREMENTS

The results of the neutron measurements are given in two sections. Section 3.4.1 deals with the data as recorded in terms of detector currents as a function of time, giving the results from each detector separately.

In Section 3.4.2 the detector currents from Pod 3 for Shot Teak are converted to a neutron flux versus time curve and compared with the calculated direct flux. This is permissible because the current due to scattered neutrons is a very small fraction of the measured current; hence, the energy versus time-of-arrival dependence is not obscured (Appendix A). However, direct conversion to a flux versus time curve is not possible in dealing with the data from Pod 4, because the contribution due to scattered neutrons is not negligible. The necessity of comparing currents rather than neutron flux rates is explained in Appendix A.

3.4.1 Experimental Results. Teak Pod 3. The currents, from the Pilot-B and Lil detectors, due to neutrons are shown in Figures 3.3 and 3.4. By use of the detector sensitivity versus energy curves (Appendix B), a neutron flux rate versus time curve can be constructed from 0.1 to 14 Mev, because the contribution from scattered neutrons can be neglected. These curves are constructed and discussed in Section 3.4.2.

This pod also yielded values for the peak flux rate and the integral flux in the 14-Mev neutron group.

The value for the peak flux rate is shown in Figure 3.8.

Teak Pod 4. In this pod the neutron detector consisted of only Pilot B. The detector current versus time data is shown in Figure 3.5.

Values for the peak neutron rate and total number of neutrons in the 14-Mev group were obtained. The results are discussed in Section 3.4.2.

Orange Pod 4. The instrumentation in this pod was similar to that in Teak Pod 4. The detector current versus time data is plotted in Figure 3.6.

Because the pod position was in error, the 14-Mev neutron group did not fall within the programmed gate times; therefore, neither the peak-reading nor integration circuits yielded information. Fortunately, information about the 14-Mev group was obtained from the time-history portion of the record, because the actual 14-Mev arrival time was later than the programmed gate closing.

**3.4.2 Comparison with Theoretical Estimates. Teak Pod 3.** Because the neutron data from this pod is free from atmospheric scattering, it could be converted to a neutron flux rate versus time plot. By use of the detector calibration curves from Appendix B, the detector currents from Figures 3.3 and 3.4 have been converted to neutron flux rates versus time and are shown in Figure 3.7. The differences between the results of the two detectors are within the estimated experimental error of each.

A composite curve which was constructed by averaging the results from both the Lil and Pilot-B detectors is shown in Figure 3.8. Two experimental points have been included for the peak flux rate of the 14-Mev neutron group. The upper point was the peak flux rate as measured by the peak-reading circuit. The lower point is the peak flux rate as calculated (Appendix A) from the measured integral value of the 14-Mev group, by assuming a nuclear reaction temperature

Also plotted in Figure 3.8 is the neutron flux rate versus time as calculated from Equation A.3 of Appendix A. As pointed out in Appendix A, the neutron energy spectrum of the device, used in this calculation, was obtained from Reference 16.

In the region from about the measured flux rates are seen to be about a third of the calculated values. Below the discrepancy increases from about a third to a fifth. This discrepancy between the measured and the expected flux is probably due to this pod's being directly below the warhead and less than 2 degrees off its axis, because of the failure of the missile tilt program. A 12-foot compartment containing various electronic control circuits, gyros, and the like, was between the device and the lower end of the warhead. If the neutron-stopping power of the odds and ends of equipment in this compartment is assumed to be equivalent to about 2 inches of steel, the discrepancy between the expected and measured flux can be resolved.

The upper measured point, in Figure 3.8, for the peak neutron flux rate of the 14-Mev neutron group does not seem consistent with the measured  $dN(T)/dT$  curve. Because this point was the result of a separate measurement, its reliability is difficult to estimate. The lower point, which was derived from the measured value of the integral number of 14-Mev neutrons and an assumed reaction temperature, seems to be consistent with the measured flux rate curve and is similarly low by a factor of 3 from the calculated peak.

As a possible check on this measurement, these results were compared with the measurements in Reference 12 and the measurements from Pod 1 as given in Reference 13. Because these measurements were made with neutron-threshold detectors that yield the total neutron flux above a threshold energy, these values have been compared with integrals over the appropriate region of  $dN(T)/dT$  curve of Figure 3.8. In particular, the total flux of neutrons whose energies are between 3 and 12 Mev can be obtained by taking the difference between the zirconium measurements (12-Mev threshold) and the sulfur measurements (3-Mev threshold).

The number of neutrons with energies between 3 and 12 Mev have been determined by integrating the appropriate regions of the curves in Figure 3.8. The results of these calculations along with the measurements from References 12 and 13, which have been normalized to the same slant range as Pod 3, are as follows:

**Teak Pod 4.** Because a large fraction (90 percent) of the detector current at Pod 4 is due to scattered neutrons, it is not possible to construct a neutron flux versus time curve from this data, as was done for Teak Pod 3. Consequently, the measured detector currents are com-

pared with expected detector currents resulting from the calculated direct and scattered flux. Figure 3.9 shows the experimental results, the expected detector currents without the contribution from the scattered neutrons, and the sum of the expected currents due to both direct and scattered neutrons. The experimental results do not extend below 3 Mev, because the sensitivity of the Pilot-B detector falls off rapidly below this energy.

The fact that this pod was within the shadow of the rear of the warhead does not reduce the measured neutron intensities by a factor of 3, as it does for Pod 3, because the major portion of the detector current is due to scattered neutrons, which do not emanate from a point source but rather from an extended source throughout the atmosphere.

There is order-of-magnitude agreement between the amplitudes of the measured and calculated curves. The reasons for the disagreement between the shapes of the two curves will be discussed in Chapter 4.

Orange Pod 4. Although this pod was closer to the device than Teak Pod 4, the total amount of atmosphere between the pod and the source was greater because of the higher atmospheric density at the lower altitude. The calculated detector current due to scattered neutrons is found to be about 100 times the current due to direct neutrons; therefore, it is not possible to convert the current versus time curve to a flux rate versus time representation. Figure 3.10 shows the measured current, the expected current from the direct neutrons, and the sum of the expected current from the direct and the scattered neutrons.

The agreement between the magnitudes of the measured and calculated detector currents is seen from Figure 3.10 to be within about a factor of 2 over the range of measurement. Possible reasons for the lack of agreement between shapes will be discussed in Chapter 4.

**3.4.3 Neutron Dose at Altitudes Accessible to Manned Aircraft.** Because the Pilot-B detector has an efficiency that falls off very rapidly below 3 Mev, it is possible to estimate the total number of fast (3 to 14 Mev) neutrons at the low pods. If the experimentally measured currents are integrated and the result converted to  $n/cm^2$ , the values are for Teak Pod 4 and for Orange Pod 4. With a value averaged over 3 to 14 Mev of  $5.5 \times 10^{-9}$  rep/( $n/cm^2$ ) for neutron flux to tissue dose conversion factor (Reference 14) and a relative biological effectiveness (RBE) factor of 10, the result is  $1 n/cm^2 \times 5.5 \times 10^{-8}$  rem for fast neutrons.

These values are seen to be higher by more than an order of magnitude than the corresponding gamma-ray dose up to 120 msec at these pod positions.

### 3.5 GAMMA-RAY MEASUREMENTS

Because of the failure of the early gamma-ray measurements discussed in Section 3.1, the only time history of gamma-ray intensities that was recovered consisted of a series of integrals, which were recorded on channels with poor high-frequency response.

The integral time ranges were: (1) from time zero (gamma-ray arrival) to a time just before the arrival of the 14-Mev neutron group at each pod; (2) from time zero to approximately 10 msec; and (3) from time zero to 120 msec. The gamma-ray intensity during the first interval was measured by integrating the current from a CsI detector from time zero to the gate opening time (Table 3.2). The integral intensity from the second and third time regions was measured by a KBr crystal, which darkens under the action of gamma radiation. The fast rise of the signal from the KBr detector was obscured, because the record was obtained from a low-frequency channel; however, the rate of rise of the integral at late times (30 to 120 msec) was extrapolated to determine the amount of prompt-gamma radiation incident on the detector.

**3.5.1 Gamma Radiation from Shot Teak.** Some information about integral gamma-ray intensities was obtained from each pod. The failure of the high-voltage power supply in Pod 2 did not affect the results of the KBr measurement, because it did not require a high-voltage supply. Table 3.3 is a summary of the integral gamma-ray results from Shot Teak.



The data from Pod 4 was noisy, and no estimate of the early gamma-ray dose from the KBr detector was possible. The CsI integral at Pod 3 appears to be too large when compared with the KBr data, which is probably more reliable.

If an inverse range-squared dependence for the gamma-ray intensity at Pod 2 and an isotropic source are assumed, it is possible to calculate the gamma-ray source strength of the device. The value for the integral gamma-ray dose at Pod 2 is equivalent to a flux which yields an integrated source strength of gamma rays of 1-Mev energy.

With the rule of thumb (Reference 15) that for each neutron escaping from a device, 0.1-Mev gamma radiation is produced, the calculated total number of escaping neutrons is: This value is to be compared with the total number of neutrons for the device (Reference 16). This agreement may be fortuitous, because the integral was taken only over the first 120 msec. However, this result may imply that a large fraction of the gamma radiation from the device has escaped within this time interval.

Assume that the gamma-ray intensity at the  $n^{\text{th}}$  pod,  $I_n$ , can be calculated by means of the well-known formula,

$$I_n = \frac{S_0 \exp \left[ - \int_{R_n} \frac{dr}{\lambda_\gamma(r)} \right]}{4\pi R_n^2} \quad (3.1)$$

Where:  $S_0$  = the total number of gamma rays emitted by the device

$R_n$  = the slant range from the device to the  $n^{\text{th}}$  pod

$\lambda_\gamma(r)$  = mean free path of 1-Mev gamma rays.

From this expression, it is possible to calculate the expected ratio of the intensities between Pods 2 and 3, and the result,  $I_2/I_3 = 2.55$ , can be compared with the ratio of the experimentally measured values, which is 1.69. Similarly, the calculated ratio between Pods 2 and 4,  $I_2/I_4 = 388$ , is to be compared with 12.33. The lack of agreement between these values indicates that a more detailed calculation to account for the gamma-ray scattering by the atmosphere is required.

**3.5.2 Gamma Radiation from Shot Orange.** Gamma-ray integral intensity results were obtained only from Pod 4. The total gamma-ray dose from 0 to 120 msec from the KBr detector was found. The initial pulse integrated from 0 to 200  $\mu\text{sec}$  measured by the CsI detector.

### 3.6 RF ATTENUATION

Although the measurement of the received signal strength of the telemetry transmitter in each pod was not one of the objectives, oscillographic records of signal strength versus time were made in order to facilitate the data analysis. Because of the intense interest in propagation of electromagnetic radiation in the vicinity of a nuclear explosion and the fact that the pods were located at a variety of different ranges, as much as possible has been extracted from these records. The presentation of this section should be considered as a summary of the data and is not intended to be an analysis. Further reduction and analysis is underway at the present time and will appear as a separate report.

Details of the telemetry system can be found in Appendix C. Each of the pods contained a 3-watt transmitter, which operated on a frequency of about 240 Mc. The body of the pod constituted the transmitting antenna, which had a pattern that was nearly isotropic with narrow 15-db depressions around the nose and tail.

A helical antenna, with about a 40-degree beam width, was used at the receiving station. The current from the first limiter grid of each receiver was recorded by an oscillograph with a resolution of about 5 msec.

The position of each pod and the burst point relative to the ground station is shown in Figures 3.11 and 3.12 with the region between the half-power points of the receiving antenna superimposed as a shaded area.

Figures 3.13 and 3.14 show the signal strength from each pod for the first half second after the burst. After a short initial blackout, the output of the signal-level monitors for Pods 2 and 3 recovered rapidly to a measurable fraction of their preshot levels, fading out again in a few tenths of a second. Pod 4 on each shot recovered in less than 0.1 second and was unaffected thereafter.

The behavior of the signal strengths for the lifetimes of the pods is shown in Figures 3.15 and 3.16.

TABLE 3.1 GENERAL PERFORMANCE

Pod	Li + Li <sup>6</sup> Neutrons	Pilot-B Neutrons	14-Mev Group Peak	14-Mev Group Integral	KBr Gamma Integral 10 msec	KBr Gamma Integral 120 msec	CsI Gamma Integral to Gate
Teak 2	No	No	No	No	Yes	Yes	No
Teak 3	Yes	Yes	Yes	Yes	Yes	Yes	Yes
Teak 4	—	Yes	Yes	Yes	No	Yes	Yes
Orange 2	No	No	No	No	No	No	No
Orange 3	No	No	No	No	No	No	No
Orange 4	—	Yes	No*	No*	No	Yes	Yes

\* Indicates no results because of incorrect pod placement.

TABLE 3.2 SLANT RANGES AND PROGRAMED GATE TIMES

t = 0 at gamma-ray arrival

Pod	Slant Range Predicted	Slant Range Actual	Gate Opening Time	Gate Closing Time
	km	km	μsec	μsec
Teak 3	15.50	15.84	180	280
Teak 4	52.62	53.74	650	1,020
Orange 4	25.46	29.45	330	510



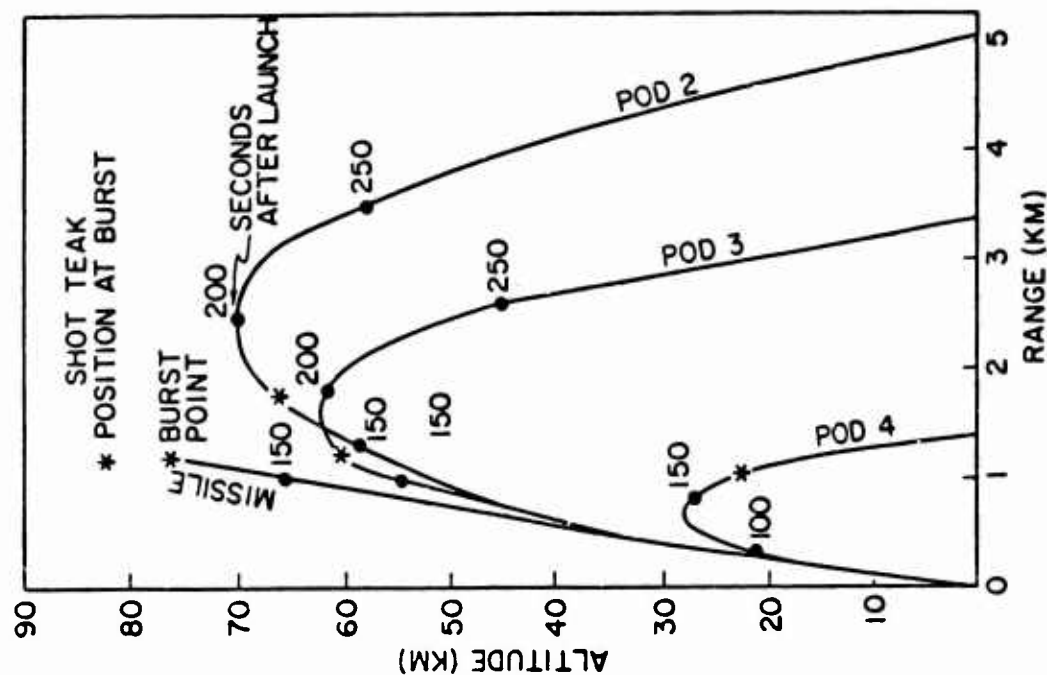


Figure 3.1 Pod and missile trajectories for Shot Teak.

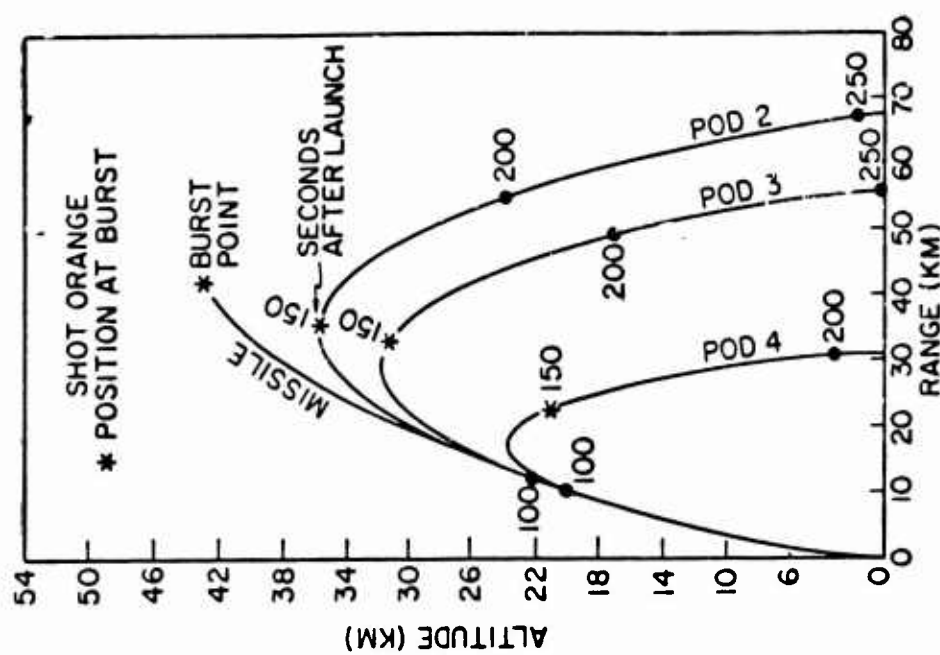


Figure 3.2 Pod and missile trajectories for Shot Orange.

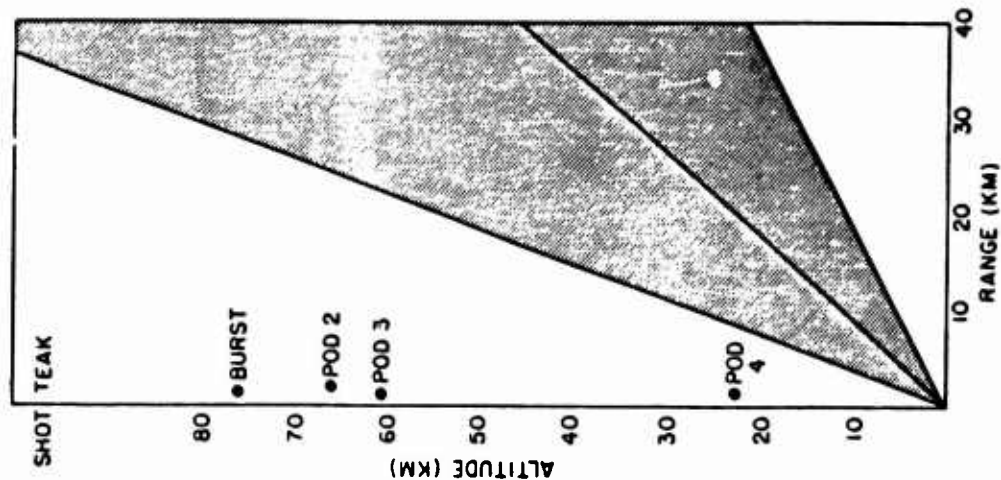


Figure 3.11 Antenna pattern and pod positions at time of burst, Shot Teak.

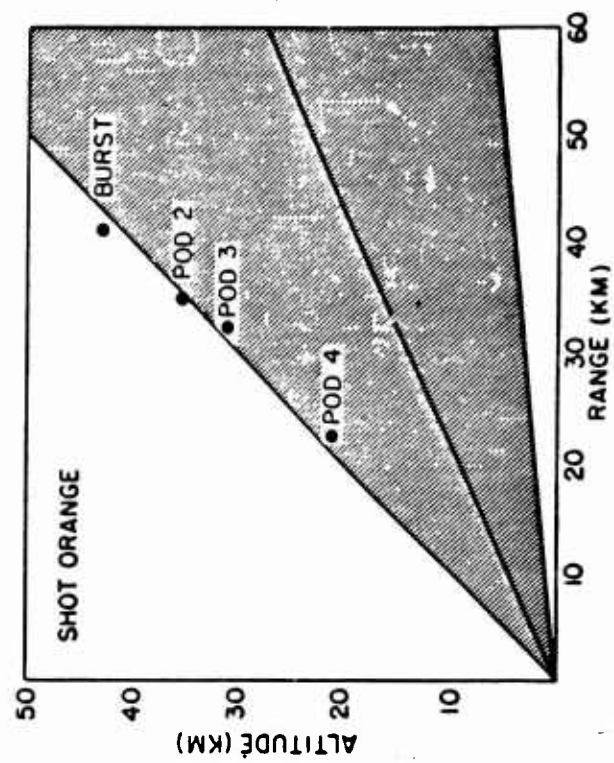


Figure 3.12 Antenna pattern and pod positions at time of burst, Shot Orange.

## Chapter 4

### CONCLUSIONS AND RECOMMENDATIONS

#### 4.1 CONCLUSIONS

The instrumentation for the time-of-flight method of measuring the neutron energy spectrum of a nuclear device has been shown to be feasible for detonations at high altitudes where atmospheric scattering effects can be neglected.

The use of the neutron energy spectrum for the (Reference 16) in computing expected neutron flux rates as a function of time gives results commensurate with the measured flux rates.

As was expected, the neutron flux at the low pods was due predominantly to scattered neutrons. However, with the Monte Carlo calculation outlined in Appendix A, it is possible to estimate the expected neutron flux rates at these altitudes with fair accuracy.

#### 4.2 RECOMMENDATIONS

Plans for future high-altitude tests should provide for instrumentation pods that are deployed by the weapon carrier; such pods present distinct advantages over independently placed rocket-borne instruments. The checkout procedure can be integrated into the weapon countdown, and any weapon placement error would also appear in the pod placement in such a way that a large part of the slant range error would be canceled. Passive pods also are easier to design and produce than rocket instruments.

The importance of time-resolved radiation measurements from high-altitude detonations will increase as the importance of high-altitude military operations increase. The possible vulnerability of AICBM and ICBM guidance systems to transient radiation effects should be studied further, and time-resolved radiation should be measured from nuclear devices at altitudes of operational interest.

## Appendix A

### THEORY

#### A.1 THE RADIATION SOURCE

The used for Shots Teak and Orange was similar to the nuclear device tested in Shot Predictions of radiation intensities were calculated using tested rules of thumb derived from information provided by B. E. Watt of the Los Alamos Scientific Laboratory (Reference 15). R. Lessler and G. Bing (Reference 16) of the University of California Lawrence Radiation Laboratory provided a neutron energy spectrum and the neutron angular distribution of the that proved very useful in making flux-rate estimates.

The neutron spectrum data in Reference 16 consisted of the total number of neutrons in each of several energy groups. For convenience, the total number of neutrons in each energy group was divided by the energy width of that group and the result was taken to be  $dN(E)/dE$  at the energy midpoint. The maximum of  $dN(E)/dE$  of the 14-Mev group was determined by fitting the integral number of neutrons in that group to a gaussian curve, the width of which was determined by a reaction temperature. This results in a full width at half maximum for the 14-Mev neutron group. This derived spectrum is shown in Figure A.1.

#### A.2 TRANSPORT OF NEUTRONS TO A DETECTOR

The interpretation of the measured currents from the detectors is complicated by two effects: the interaction of neutrons with the atmosphere and the variation of the detector efficiency with energy. It is necessary to account for those neutrons of a given energy that are lost from the direct beam and hence do not reach the detector, as well as those neutrons of higher energy that are scattered, arrive late, and simulate neutrons of a lower energy.

Let  $Q(E)$  be the average charge produced per neutron of energy  $E$  impinging upon the detector. Let  $A(E)$  be the attenuation factor of the direct neutron beam due to scattering and absorption. The function  $K(E', T)$  is defined as the number of scattered neutrons that are emitted from a unit source with an energy  $E'$  and arrive at the detector at a time  $T$  which corresponds to the direct arrival of neutrons of energy.

$$E = \frac{m r_{SD}^2}{2T^2} \quad (A.1)$$

Where:  $m$  = mass of the neutron

$r_{SD}$  = distance between the source and the detector

The expression for the detector current as a function of time is as follows;

$$I(T) = \frac{dN(T)}{dT} Q(E) A(E) + \int_E^\infty Q(E') K(E', T) \frac{dN(E')}{dE'} dE' \quad (A.2)$$

The factor  $dN(T)/dT$  is the number of neutrons that would be impinging on a detector per unit time if there were no atmospheric scattering or absorption. The first term on the right hand side of this equation is the contribution to the total detector current arising from unscattered neutrons, while the second term is the contribution from all neutrons that arrive at the detector after having been scattered. II

$$\frac{dN(T)}{dT} = \frac{(2E)^{1/2}}{r_{SD} m^{1/2}} \frac{dN(E)}{dE}$$

which was developed in Chapter 1, is substituted in Equation A.2, then

$$I(T) = \frac{(2E)^{1/2}}{r_{SD} m^{1/2}} Q(E) A(E) \frac{dN(E)}{dE} + \int_E^\infty Q(E') K(E', T) \frac{dN(E')}{dE'} dE' \quad (A.3)$$

### A.3 NEUTRON-SCATTERING CALCULATIONS

Equation A.3 is an integral equation and could be solved for  $dN(E)/dE$  providing  $I(T)$  and  $K(E', T)$  were known.  $I(T)$  is the experimentally measured detector current, so it remains only to evaluate  $K(E', T)$ . If only singly scattered neutrons are considered, the evaluation of the kernel  $K(E', T)$  is straightforward and gives a lower limit on the scattered neutron flux. This relatively simple calculation was done (Section A.3.1) in order to aid in the planning phases of the experiment. A more elaborate multiple-scattering calculation (Section A.3.2) was made to aid in the interpretation of the actual experimental results.

**A.3.1 Calculation of  $K(E', T)$ , Single Scattering.** A surface formed by the revolution of an ellipse about its major axis has the property that the sum of the distances,  $r_D + r_S$ , from each focus to a point on the surface is constant. Any neutron of a given energy that leaves the source (at the first focus) at  $T_0 = 0$  and reaches the detector (at the second focus) at a time  $T$  will have been scattered at the surface of an appropriate ellipsoid. This procedure is valid only if inelastic processes and the recoil of the air nuclei may be neglected.

Neutrons which travel the direct path from the source to the detector arrive at a time  $T = 2L/v$ , where  $v = (2E'/m)^{1/2}$  and  $2L$  is the distance between the source and the detector. Neutrons that leave the source in all other directions and reach the detector at a time  $T$  are scattered from a point on an ellipsoid having the property that  $r_S + r_D = vT$ . The equation of the scattering ellipsoid in cylindrical coordinates is seen to be

$$\frac{z^2}{L^2} + \frac{\rho^2}{(r^2 - 1)L^2} = 1$$

with the semimajor axis  $= L\tau$  and the semiminor axis  $= L(\tau^2 - 1)^{1/2}$  where  $\tau = T/T_0$ ,  $r_S + r_D = 2L\tau$ .

In order to determine the number of neutrons which arrive in the time interval between  $T$  and  $T + dT$ , it is necessary to consider the two elliptical shells shown in Figure A.2. The volume element shown lies between two  $z$  planes and the elliptical surfaces described by  $T$  and  $T + dT$  and is  $dV = 2\pi\rho d\rho dz$ . For a neutron source of unit strength per steradian, the number of neutrons of energy  $E'$  which arrive at the detector during the interval  $dT$  is given by

$$\begin{aligned} K(E', T) dT &= \int \alpha \left( \frac{A_S(r_S)}{r_S^2} \right) \left( \frac{A_D(r_D)}{r_D^2} \right) \sigma(\cos \theta) n(z') 2\pi\rho d\rho dz \\ &= 2\pi\alpha \int \sigma(\cos \theta) n(z) A_S(r_S) A_D(r_D) \left( \frac{\rho d\rho}{r_S^2 r_D^2} \right) dz \end{aligned}$$

Where:  $\alpha$  = area of the detector

$\sigma(\cos \theta)$  = differential cross section for elastic scattering in air of neutrons of energy  $E$ , in units of  $\text{cm}^2/\text{steradian}$

$n(z')$  = number of air molecules per cubic centimeter at an altitude of  $z' = z_0 + z$  above the ground

$$A_S(r_S) = \exp \left[ - \int_{z_S}^z \frac{dr_S}{\lambda(z')} \right]$$

$$A_D(r_D) = \exp \left[ - \int_z^{z_D} \frac{dr_D}{\lambda(z')} \right]$$

$$\lambda(z') = \text{neutron mean free path} = \frac{1}{\sigma_t n(z')}$$

$\sigma_t$  = total scattering cross section for neutrons in air

$z$  = height of dV relative to  $z_0$

$z_S$  = height of source relative to  $z_0$

$z_D$  = height of detector relative to  $z_0$

$A_S$  and  $A_D$  are the exponential attenuation factors for the paths  $r_S$  and  $r_D$  respectively. The integrals within these exponential terms are, for a given  $\tau$ , functions of  $z$  explicitly through  $\lambda(z')$  and the limits, and must be evaluated numerically for each value of the integrand of Equation A.1.

In order to put Equation A.1 into a more tractable form, we observe from the figure that

$$r_S^2 = \rho^2 + (z-L)^2$$

and

$$r_D^2 = \rho^2 + (z+L)^2$$

and upon subtraction of these relations from each other we obtain

$$r_D^2 - r_S^2 = 4Lz = (r_D - r_S)(r_D + r_S).$$

But since

$$r_S + r_D = 2L\tau,$$

we see that

$$r_D - r_S = 2z/\tau.$$

From these relationships we can obtain the following results,

$$r_D = L\tau + z/\tau$$

and

$$r_S = L\tau - z/\tau.$$

We may now express  $r_S$ ,  $r_D$  and  $r_S^2 + r_D^2$  in a form which is useful for substitution in Equation A.2, as follows,

$$r_S^2 + r_D^2 = 2 \left[ (L\tau)^2 + (z/\tau)^2 \right]$$

and

$$r_S r_D = \left[ (L\tau)^2 - (z/\tau)^2 \right].$$

From Figure A.1, it is observed that

$$\cos \theta = \frac{(2L)^2 - (r_S^2 + r_D^2)}{2 r_S r_D}$$

By use of the above expressions for  $r_S$ ,  $r_D$  and  $r_S^2 + r_D^2$ , the following is obtained.

$$\begin{aligned}\cos \theta &= \frac{2L^2 - [(L\tau)^2 + (z/\tau)^2]}{[(L\tau)^2 - (z/\tau)^2]} \\ &= \frac{2 - (\tau^2 + x^2)}{(\tau^2 - x^2)}\end{aligned}$$

where  $x = z/L\tau$ .

To determine the number of neutrons arriving in the interval  $dT$ , it is necessary to relate  $d\rho$  to  $d\tau$ . It can be seen from Figure A.1 that the element of area for a fixed  $z$  is proportional to  $d\rho$ . After the equation for the ellipse,

$$\rho^2 = (1 - 1/\tau^2)(\tau^2 L^2 - z^2),$$

is differentiated with respect to  $\rho$  and  $\tau$  ( $z$  held constant), the following is obtained.

$$\rho d\rho = [(\tau L)^2 - (z/\tau)^2] d\tau/\tau$$

With  $\tau = T/\bar{T}$ ,

$$d\tau = [(L\tau)^2 - (z/\tau)^2] dT/\bar{T}\tau$$

This expression can be solved for  $d\rho$  as a function of  $\tau$  and  $d\tau$ ; however, the quantity which occurs in the integrand of Equation A.2 is  $\rho d\rho$ .

After this expression is substituted in the equation,

$$K(E', T) dT = 2\pi\alpha \int \frac{\sigma(\cos \theta) n(z') A_S(z) A_D(z) [(L\tau)^2 - (z/\tau)^2]}{[(L\tau)^2 - (z/\tau)^2]^2 \bar{T}\tau} dT dz$$

If  $z = L\tau x$  and  $dz = L\tau dx$ , then

$$K(E', T) = \frac{2\pi\alpha}{\bar{T}L} \int_b^1 \frac{\sigma(\cos \theta) n(x) A_S(x) A_D(x)}{(\tau^2 - x^2)} dx$$

where  $b = 1$  or  $z_0/L\tau$ , whichever is the smaller.

These limits of integration have been chosen so that the complete shell is integrated. This requires that the limits on  $x$  be taken from  $+1$  to  $-1$ . If the ellipse touches the ground, it is assumed that the neutrons directed toward the ground are lost by absorption at  $-z_0$ , and  $b$  should have the value  $z_0/L\tau$ .

For a unit source strength, the expression  $K(E', T)$  is the number of scattered neutrons per unit time, of energy  $E'$ , which arrive at a time  $T$ . This integral was programmed for the IBM 704 at the National Bureau of Standards. The results for Pods 3 and 4 during Shot Teak with  $E'$  equal to 14 Mev are shown in Figures A.3 and A.4. From these results it was concluded that scattering would not interfere strongly with time-of-flight analysis of the near-pod data. A better estimate requires consideration of other neutron energies and multiple scattering.

**A.3.2 Multiple-Scattering Calculations.** A Monte Carlo program was developed to evaluate the integral in Equation A.3, which represents the contribution to the detector current due to neutrons that have been scattered. This program includes elastic, inelastic, and absorptive processes of oxygen and nitrogen in the atmosphere.

In this discussion, it is necessary to follow the time and energy history of neutrons that leave the source with an initial direction ( $\theta_0, \phi_0$ ) and with an initial energy ( $E_0$ ). Each neutron is initially weighted by the angular distribution of the source,  $F(\alpha)$ , by the energy of the neutron through the energy distribution function,  $dN(E)/dE$ , and by the solid angle into which it is projected,  $\sin \theta_0 \Delta\theta_0 \Delta\phi_0$ , as follows:



$$w_0 = F(\alpha) \left[ \frac{dN(E)}{dE} \right]_{E_0} \sin \theta_0 \Delta \theta_0 \Delta \phi_0 .$$

The probability that a neutron of energy  $E$  has undergone a collision in a distance  $R$  through the atmosphere is

$$P = 1 - e^{-\sigma_t^A(E) \int_R n(r) dr} \quad (A.4)$$

Where:  $\sigma_t^A(E)$  = total cross section for neutrons of energy  $E$  in air  
 $n(r)$  = number density of air nuclei along the path

The distance to the first collision is then determined by choosing a random number  $N$ , between zero and one, setting it equal to  $P$  and solving for  $R$ . The integral in Equation A.4 is calculated from a stored table of atmospheric densities, and  $\sigma_t^A(E)$  is taken from a stored table of cross sections versus energy.

At this point in the program, it is necessary to make a series of decisions. The first decision determines whether the collision is with oxygen or nitrogen. Next, for either case, it must be decided whether the collision is elastic or inelastic. If the collision is inelastic, the energy of the neutron is reduced by an amount appropriate for an N or O collision, and an outgoing direction is assigned in a random fashion, because the differential cross section is considered to be isotropic. For an elastic collision, the energy change is determined by the scattering angle, and this angle is chosen by the program through the use of the appropriate differential cross section. To account for the possibility that this neutron is absorbed in the collision, the weight of the outgoing neutron is reduced by the factor

$$\left( \frac{\sigma_{\text{absorption}}}{\sigma_{\text{total}}} \right)_{N \text{ or } O}$$

Before determining the next collision point, the probability that the neutron would go directly to the detector without further scattering is computed. The charge produced by the detector due to this neutron is stored into an appropriate time interval, and the number of collisions which it has undergone is recorded. The weight of the outgoing neutron is further reduced by the fractional solid angle subtended by the detector. It is now possible to continue this process and determine the distance to the next collision, starting with the new weight,  $w_N$ .

The atmosphere is here considered to be made up of four parts of nitrogen to one part of oxygen, and the total cross section in air, in terms of the total cross sections for nitrogen and oxygen  $\sigma_t^N$  and  $\sigma_t^O$ , is therefore,

$$\sigma_t^A = \frac{4 \sigma_t^N + \sigma_t^O}{5}$$

and the probability that a collision is with, say, oxygen is

$$\frac{\sigma_t^O}{5 \sigma_t^A}$$

Whether the collision is with oxygen or nitrogen is then decided by selecting a random number between 0 and 1. The collision is taken to be with oxygen if the number is smaller than  $\sigma_t^O/5 \sigma_t^A$ , or with nitrogen if the number is larger.

In order to determine whether a given collision is inelastic or elastic, the ratio of

$$\left( \frac{\sigma_{\text{inelastic}}}{\sigma_{\text{elastic}} + \sigma_{\text{inelastic}}} \right)_{N \text{ or } O}$$

is compared with a random number between 0 and 1. If this ratio is larger than the number, the collision is taken to be inelastic or taken to be elastic if this ratio is smaller than the number.



In the event that the collision is elastic, the exit direction to the next collision point is chosen in the following manner. The azimuthal angle,  $\phi$ , is selected randomly, because the scattering is axially symmetric. The scattering angle  $\theta$  is chosen by selecting two random numbers,  $N_1$  and  $N_2$ , between zero and one. The angle  $\theta$  is tentatively set equal to  $\pi N_1$ , and  $N_1$  is then compared with

$$\left( \frac{d\sigma(\pi N_1)}{d\Omega} \right)_{N \text{ or } O}$$

which has been normalized to unity at its maximum value. If  $N_1$  is larger than this quantity, then this pair of random numbers is rejected. New pairs are chosen until

$$N_1 < \left( \frac{d\sigma(\pi N_1)}{d\Omega} \right)_{N \text{ or } O}$$

In the event of an inelastic collision, both exit angles,  $\theta$  and  $\phi$ , are chosen randomly, because the scattering has been assumed to be isotropic. In both nitrogen and oxygen, only the first excited states have been considered with regard to determining the exit energy. For nitrogen, 2.3 Mev is subtracted from the entrance energy and 6.1 Mev is subtracted for oxygen.

If a neutron emerges from collision  $N$  with a weight  $w_N$  and an energy  $E_N$ , the contribution to the charge produced by the detector is seen to be

$$C_D = w_N Q(E_N) \frac{dP(\theta)}{d\Omega} \frac{A}{R^2} \cdot - \sigma_t A(E_N) \int_R n(r) dr$$

Where:  $Q(E_N)$  = charge produced in the detector by a neutron of energy  $E_N$

$A$  = area of the detector

$R$  = distance from the detector to the scattering point

and the function  $dP(\theta)/d\Omega$  is that differential scattering probability appropriate to the  $N^{\text{th}}$  collision, normalized such that

$$\int_0^{4\pi} \frac{dP(\theta)}{d\Omega} d\Omega = 1$$

The original neutron with modified parameters continues to make collisions until, (1) the time exceeds the time of interest, (2) the neutron energy falls below a cutoff value, or (3) the neutron weight becomes negligible. After a neutron has reached cutoff, the program recycles until it has scanned all initial directions.

In the program, the contribution to each of three pods of a given shot was obtained from every collision. Eight neutron energy groups were used—14, 10, 6, 3, 2, 1.25, 0.9, and 0.65 Mev—with a total of 1,296 neutrons in each group. This number of neutrons was found to be adequate to give statistical fluctuations in the results for the low pods of about  $\pm 30$  percent.

This routine was programed and carried out by Dr. Werner Reinbolt and Mr. John Maynard of the National Bureau of Standards.

It should be noted that, when (as in the Monte Carlo calculation) neutron energy loss in scattering is taken into account, there is no longer a direct correlation between a neutron's time of flight and its initial energy; consequently, it is not possible to measure the energy spectrum of neutrons that arrive at a detector. Although in principle it would have been possible to solve the integral Equation A.3 for the energy spectrum of the device  $dN(E')/dE'$ , using the Monte Carlo evaluation of the scattering integral, this was not felt to be justified. Instead a comparison of the experimental detector current with the calculated current was made, using the spectrum from Reference 16.

The results of these calculations for Pod 4 for both Shots Teak and Orange are shown in Figures A.5 and A.6. These curves were smoothed and are reproduced in Chapter 3 of this report and are seen to be in fair agreement with the experimentally measured currents.

A.3.3 Comparison of the Results of the Single- and Multiple-Scattering Calculations. In Figure A.7, a comparison is made between the results of the single-scattering calculations and the Monte Carlo multiple-scattering calculations for the 14-Mev neutron groups at Pod 4 for Shot Teak. The general agreement for early times is reasonably good and for later times, when multiple scattering is important, the Monte Carlo results are consistently higher.

A.3.4 Results of Scattering Calculations for Shot Yucca (Project 2.7). The scattering calculations required by the Project 2.7 participation in Shot Yucca were essentially identical to those called for by the Project 2.6 experiment and were performed with the same IBM 704 program. The results of these calculations are presented here. Additional information concerning Project 2.7 is given in Reference 18.

As in the mathematical determination, presented above, the detector sensitivities were folded into the calculation so that the results were obtained in forms of detector current. The following parameters apply: (1) Only one detector,  $\text{Li}^6\text{I}$ , was used; (2) the device burst at 25.30 km above sea level; and (3) the detector was positioned at 0.84 km below the burst.

Table A.1 is the neutron energy spectrum used to calculate the scattered flux.

The ratio of detector currents due to scattered and direct flux is of primary interest, because this allows an evaluation of the precision of the experimental measurement. The detector currents determined by the scattering calculation have been averaged over the time intervals corresponding to the arrival times of the neutron groups in the original spectrum. These averages are shown in Figure A.8. In this form, they may be compared directly with the detector currents due to the direct neutron flux. The attenuation in the direct path was calculated using the same total cross sections as in the IBM 704 scattering calculation. By use of the same detector sensitivities as for the scattering calculation, the detector currents due to direct neutrons may be found. These are shown in Figure A.9.

The ratio of detector current due to scattered neutrons to that due to direct neutrons is shown in Figure A.10. It is apparent that within the accuracy of the calculation this ratio is about 2 percent for the worst case. A statistical analysis of some of the scattered flux groups has shown that they probably are in error by no more than a factor of 2. This implies that, for neutron energies above 0.025 Mev, the error introduced in the experimental measurement by neglecting the scattered neutron flux would have amounted to only about 2 percent. This is considerably less than that expected from other sources of error, e. g., detector calibration and recording and telemetering systems.

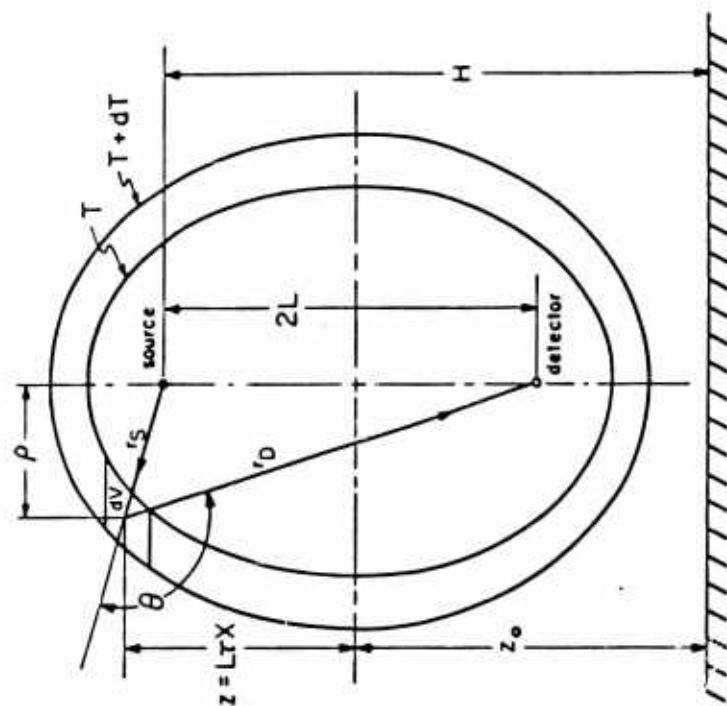


Figure A.2 Single-scattering calculation geometry.

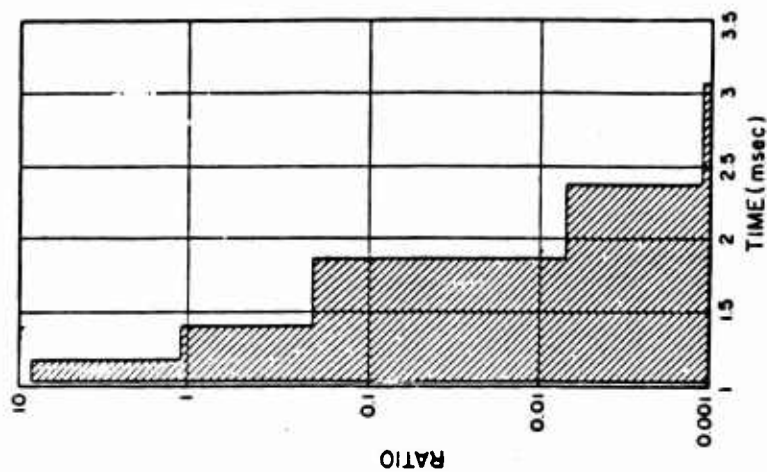


Figure A.4 Ratio of currents due to singly scattered and direct 14-Mev neutrons versus time for Pod 4, Shot Teak.

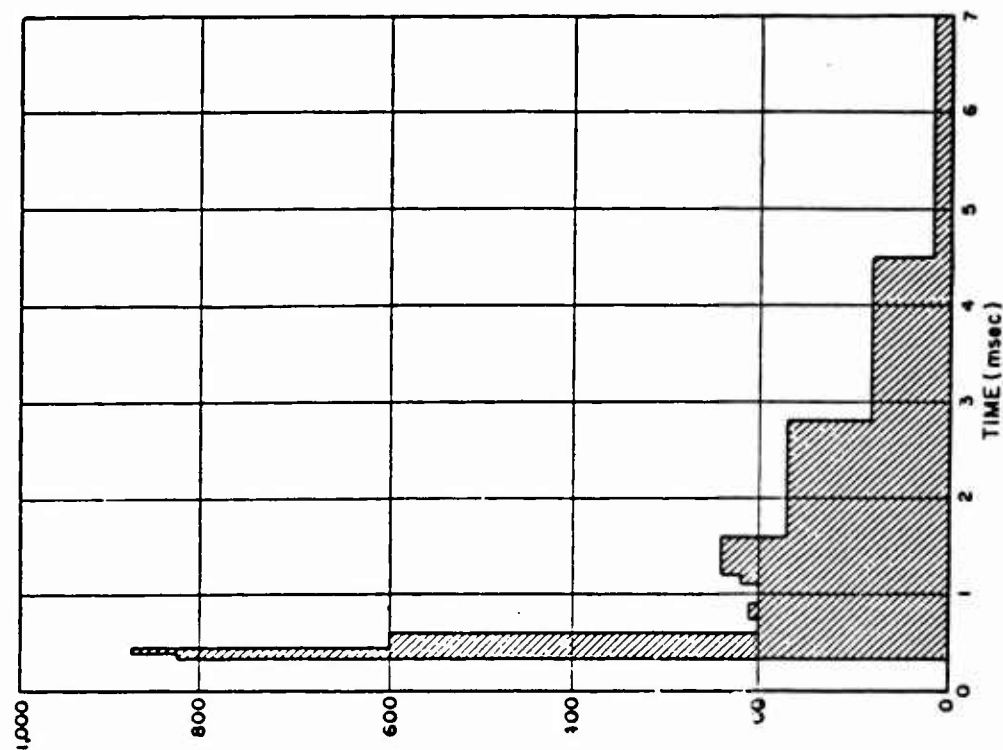


Figure A.3 Ratio of currents due to singly scattered and direct 14-Mev neutrons versus time for Pod 3, Shot Teak.

## Appendix B

### DETECTORS

#### B.1 BACKGROUND

The early work of the detector group was devoted to a thorough study of the properties and characteristics of a large number of existing neutron detectors and to a calculation of the neutron intensities expected (on the basis of the estimated yield of the device) as a function of time. It was found necessary to use a combination of several detectors in order to make the desired measurements.

One of the prime considerations in the selection of the neutron detectors was their relative sensitivity to neutrons and gamma rays. Because the number of gamma rays that arrive at a detector, during the time the neutrons arrive, was uncertain by at least several orders of magnitude for nuclear detonations at very high altitudes, it was necessary to make the ratio of neutron sensitivity to gamma-ray sensitivity as large as possible. In the neutron-energy range from 3 to 14 Mev, the study of neutron-detector properties indicated that this ratio was largest for organic scintillators. Because of its low cost and convenience of handling, the Pilot-B scintillator was selected for the high-energy neutron detectors. Because the light output per neutron decreases rapidly with neutron energy, the sensitivity ratio decreases at a similar rate and becomes rather poor for neutrons below 1 Mev. This decrease occurs because the average energy of the recoil protons in the scintillator decreases with energy, and the light output of the scintillator saturates with increasing rate of energy loss of a particle.

The sensitivity ratio of a  $\text{Li}^6\text{I}$  scintillation crystal was found to be highest in the region of fission neutrons and to increase with decreasing neutron energy, because the  $\text{Li}^6(n, \alpha)\text{T}$  reaction has a large  $Q$  (4.8 Mev) and the cross section increases rapidly (proportional to  $1/v$  as the neutron energy decreases). A large resonance at 0.25 Mev helps to make the cross section relatively large even up to 6 Mev; thus,  $\text{Li}^6\text{I}$  crystals appear to be excellent detectors for neutrons below 6 Mev. Because  $\text{LiI}$  has a rather high efficiency for detecting gamma rays, it was necessary to use a normal  $\text{LiI}$  detector in order to determine the gamma-ray background in the enriched  $\text{Li}^6\text{I}$  crystal.

The detector sensitivities of these three crystals were too large to record the initial burst of gamma rays; thus, a less-sensitive gamma-ray detector (small  $\text{CsI}$  crystal detector) was built for this purpose.  $\text{CsI}$  was selected because of the long decay time of its light output, which allows the sharp peak in the gamma-ray intensity to be averaged over an interval of time of about 1  $\mu\text{sec}$ . The peak detector currents are thus lowered without reducing the value of the integral of the detector current. A detector channel containing no crystal was included to monitor currents resulting from the effects of nuclear and electromagnetic radiations on the detector circuits.

Another detector was used to determine the total gamma-ray dosage measured over a period of 120 msec. This detector consisted of a crystal of  $\text{KBr}$  treated so as to color under the action of gamma rays. The resulting change in light transmission was measured by means of a lamp and a small (1P42) photodiode. The sensitivity of the crystal was such that dosages ranging from 50 to 2,000 r were easily detectable.

Calculations of the attenuation of the neutrons in the atmosphere for Pod 4 for both Shots Teak and Orange showed that time-of-flight measurements in these pods would be meaningless except for the 14-Mev group. For this reason, only the Pilot-B detector was used in these pods for

time-of-flight information. Because the Pilot-B detector gives information about the biological effect of both neutrons and gamma rays, the integral of this detector current was telemetered as a function of time until the pods fell into the water.

## B.2 CALIBRATION

The calibration of the neutron detectors was for the purpose of establishing the relationship between the neutron flux passing through the detectors and the corresponding output currents of the photodiodes. Because it was necessary to calibrate the detectors over a considerable range of energies, the NRL 2-Mev Van de Graaff generator was used to produce monoenergetic neutrons from the following reactions:  $T(p,n)He^3$  (0.15, 0.25 and 0.36 Mev neutrons),  $D(d,n)He^3$  (4.25 Mev neutrons), and  $T(d,n)He^4$  (15.0 Mev neutrons). A photomultiplier was used to observe individual events in the crystals, because the neutron fluxes available were too small to permit direct observation by a photodiode of the light from the LiI. The photomultiplier produced a series of pulses, which were recorded with a 256-channel pulse-height analyzer.

Because the channel number of each event was proportional to the light output of the crystal for that event, a quantity  $P(E_N)$ , representing the total light output at a given neutron energy  $E_N$ , could be defined as

$$P(E_N) = \sum_{j=1}^{256} j m_j$$

Where:  $j$  = channel number

$m_j$  = number of counts in that channel

At higher neutron energies, reactions other than those listed above began to take place, namely,  $Li^6(n,dn)He^4$  and  $Li^7(n,d)He^6$ , as well as gamma activity arising from the inelastic scattering of neutrons on iodine. All of these processes contributed to the light output of the crystal and formed a continuous background, which increased with increasing energy.

The total neutron flux  $N$  was determined with the aid of a calibrated long counter, which subtended the same solid angle at the neutron source as the detector. The quantity  $P(E_N)/N$  was then proportional to the average light output per unit of neutron flux.

It was then necessary to establish a relationship between the crystal's light output and the sensitivities of the photomultiplier and the photodiode. This determination was complicated by the fact that the spectral response of these two tubes was different. Therefore, a single crystal was used as a light source for both, and X rays from the NRL 21-Mev betatron were sufficiently intense to be used for excitation.

By measurement of the charge released by the photodiode when a high intensity betatron pulse was incident upon the crystal and comparison of it with that produced by the photomultiplier from a low-intensity pulse, it was possible to establish the desired relationship between the tube sensitivities.

The calibration formula could then be expressed as

$$Q_N^{PD}(E_N) = \frac{\gamma_{PM}}{\gamma_{PD}} \frac{[P(E_N)/N]}{p_\beta} Q_\beta^{PD}$$

The value  $Q_N^{PD}(E_N)$  = average charge released by the photodiode per unit of neutron flux of energy  $E_N$  striking the crystal

$\gamma_{PM}$  and  $\gamma_{PD}$  = radiation dosages per burst at the low and high levels, respectively

$p_\beta$  = height of the pulse produced by the photomultiplier for a low-intensity betatron burst in units of  $P(E_N)$ , and

$Q_\beta^{PD}$  = charge released by the photodiode for a high-intensity burst,

where  $P(E_N)/N$  was defined above.

Figure B.1 shows  $1/Q_N^{PD}(E_N)$  as a function of energy for both  $Li^6I$  and normal  $LiI$ . By use of the measured current outputs of the photodiodes in conjunction with these curves and conversion of the time-of-flight information to energy, it was thus possible to determine the neutron energy spectrum.

The calibration of the gamma-ray detectors consisted of determining, in one case, the charge liberated by a photodiode as a result of the scintillations of a small crystal of  $CsI$  and, in the other case, the change in light transmission of a crystal of  $KBr$ .

The  $CsI$  detector was calibrated by its exposure to a calibrated gamma-radiation field produced by a  $Co^{60}$  source. The output currents of the photodiode were measured with a vibrating-reed electrometer.

The  $CsI$  detectors were also exposed to  $1/4$ - $\mu$ sec bursts of X rays from the NRL betatron. The charge produced by the photodiode as a result of an X-ray burst striking the crystal was measured. From the known radiation dose in each burst, it was possible to obtain a value of the photodiode current for a given radiation rate. It was found that the calibration figure in coulombs per roentgen for the  $Co^{60}$  source was about 32 percent higher than that for the betatron. This can be understood when it is realized that a larger percentage of incident gamma energy is deposited in a small crystal when the energy is low. The X rays from the betatron were much more energetic than those from the  $Co^{60}$ . Because the energy spectrum of the  $Co^{60}$  more nearly approximated that expected from the device, the  $Co^{60}$  results were weighted more heavily.

The calibration figure for the tube and crystal used here was  $0.7 \times 10^{-10}$  coulomb/r.

The  $KBr$  detector was also calibrated by exposure of the crystal to the  $Co^{60}$  source. The output current of the photodiode was measured as a function of time, and from the known radiation rate and the photodiode current, the light transmission (defined as the ratio of photodiode currents before and after exposure) of the crystals could be expressed as a function of total gamma dose. The curve of transmission ( $I/I_0$ ) as a function of dosages is given in Figure B.2.

### B.3 DETECTOR CONFIGURATION FOR PODS

The detectors for Pods 2 and 3 for Shots Teak and Orange were as follows: (1) a  $CsI$  scintillator with a photodiode with its sensitivity adjusted to measure the prompt-gamma rays, (2) a Pilot-B plastic scintillator with a dual photodiode system to provide the integral of the 14-Mev neutrons, their peak intensity, and a time history of total dose, (3) a  $Li^6I$  scintillator with photodiodes to provide the neutron time history, (4) a normal  $LiI$  scintillator to give the same type of information as the  $Li^6I$ , but with a different neutron sensitivity so that gamma-ray background could be measured and gamma-ray corrections made in the  $Li^6I$  detector current, (5)  $KBr$  detector, and (6) a blank detector photodiode.

The detectors for Pod 4 for Shots Teak and Orange consisted of: (1) a  $CsI$  scintillator for prompt-gamma-ray measurement, (2) a Pilot-B plastic scintillator to read 14-Mev neutron data, (3) and (4) two Pilot-B plastic scintillators to measure the time history of total dose at two sensitivities for the period after the 14-Mev group, (5) a  $KBr$  detector, and (6) a blank detector similar to the ones in Pods 2 and 3.



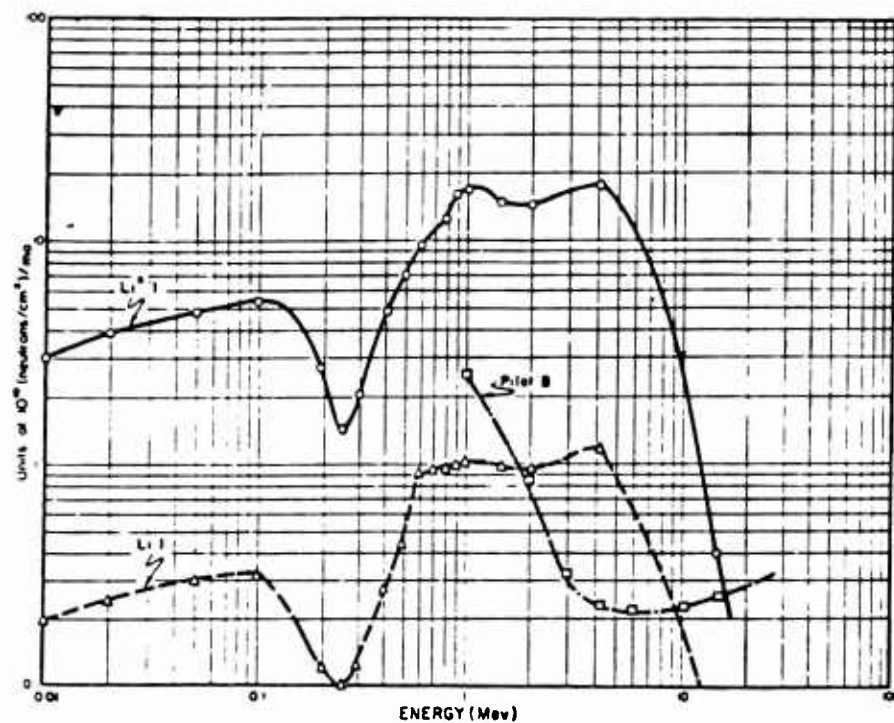


Figure B.1 Calibration curves for LiI, Li<sup>6</sup>I, and Pilot B.

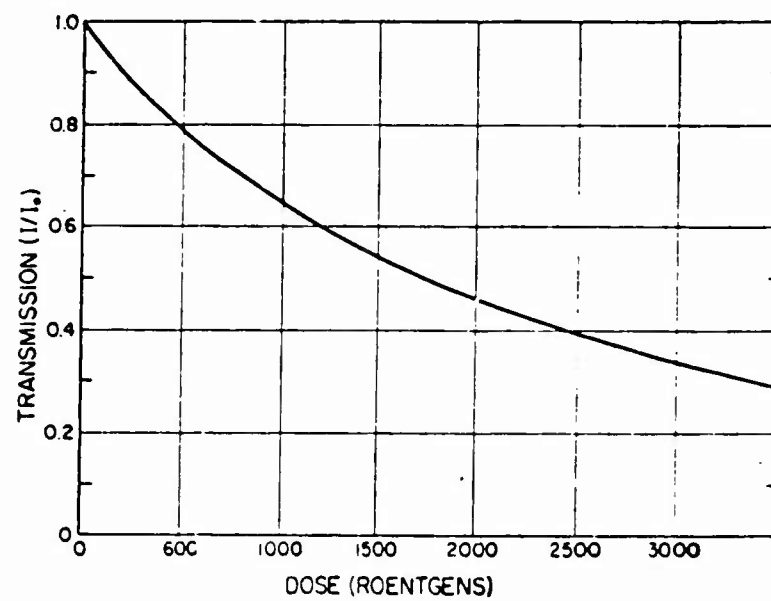


Figure B.2 Calibration curve for KBr detector.



## Appendix C

### INSTRUMENTATION

The pod instrumentation consisted of detectors, detector electronics, data recorder, program unit and telemetry transmitter, and power supplies. The detectors and their calibration are described in Appendix B.

The detectors were designed to provide current signals of amplitude suitable for coding and recording. The technical limitations imposed by the state of the recording art required careful electronic treatment prior to recording. The pod instrumentation is described below, starting with the detector outputs, and follows the path of the signals to the final data record in the ground receiving station.

Figures C.1, C.2, and C.3 show the detector electronics used in Pods 2 and 3 for both Shots Teak and Orange, Pod 4 for Shot Teak, and Pod 4 for Shot Orange, respectively.

#### C.1 PODS 2 AND 3

**C.1.1 CsI.** Detector 1 was a CsI crystal chosen to give a measurable signal from the prompt-gamma-ray spike. It consisted of the CsI crystal fixed to the face of a single photodiode (Type 926). The prompt-gamma-ray signal spike followed two paths.

For purposes of timing, the signal was applied to a timing circuit that provided the gates for electronic commutation of all the detector signals (Figure C.1). For purposes of the integrated prompt-gamma measurement, the gamma-ray signal was applied to a peak-reading circuit. The timing circuit (marked "timer," "limiter," "delay," and so forth, on Figure C.1) provided a gate signal at 110  $\mu$ sec, a pedestal 70- $\mu$ sec-wide beginning at the 110- $\mu$ sec gate signal, and a series of three 10- $\mu$ sec pulses at gamma-ray arrival time  $H$ ,  $H + 110 \mu$ sec, and  $H + 180 \mu$ sec (these times vary with pod positions). These latter three signals were recorded directly on Tape Channel T-1. The 110- $\mu$ sec gate signal closed the normally open gamma-ray peak-reading circuit at 110  $\mu$ sec for the duration of the measurement. The peak-reading circuit registered the maximum value of the voltage on the condenser shown above the block for the circuit in Figure C.1. The voltage on the condenser was the integral of the detector current. The peak value of the condenser voltage was applied to the voltage-controlled-oscillator (VCO) Channel 10. Subcarrier VCO's are discussed below in the section on the tape recorder.

**C.1.2 Pilot B.** The Pilot-B scintillator Detectors 2A and 2B were included to provide adequate sensitivity for fast neutrons, particularly the 14.2-Mev neutron group. The light output of this scintillator was measured by two groups each consisting of three photodiodes.

The photodiode current from Group 2B was used for two measurements. The first of these was the total dose versus time measurement for which the current pulse was integrated by a pulse-controlled oscillator (PCO), shown as the "LF converter" on the block diagram. The PCO pulses drove a binary-modulator circuit that directly modulated the transmitted carrier amplitude to 30-percent depth. This was a real-time link that operated from detonation time throughout the flight of the pod.

The second use of Detector 2B current was for the measurement of the integral of the 14.2-Mev neutrons. The normally closed (NC) integrate-and-hold block (Figure C.1) represents this function. The integrating process was controlled by the gate pedestals from the timer. Integration occurred during the period from 110 to 180  $\mu$ sec after gamma-ray arrival. The

value of this integral, expressed as a voltage, was applied by a holding circuit to VCO Channel 11. The purpose of the holding circuit was to keep the voltage, which represents the integral, constant for a period long enough for the VCO to respond.

Detector Group 2A was also used for two measurements. The first use of this detector group was to obtain the time dependence of the fast neutron flux. The output of the Log-R circuit was applied to a PCO labeled "HF converter." The purpose of the Log-R circuit was to compress the dynamic range of the detector current to a range that could be handled by the recording circuitry. The Log-R output was applied to VCO Channel E and through a high-pass filter to the gated mixer that selected the 110- to 180- $\mu$ sec section for recording directly on Tape Channel T-2. The Detector 2A current that was applied to the PCO was encoded by the latter, and the PCO signal recorded on Tape Channel T-2 from 180  $\mu$ sec throughout the rest of the measurement.

The second use of the Detector 2A current was for the measurement of the peak value of the 14.2-Mev neutron flux. This measurement was made by the normally closed peak reader on the compressed 14.2-Mev neutron signal from Log-R output, was held, and then was applied to VCO Channel 12.

**C.1.3  $\text{Li}^6\text{I}$ .** The  $\text{Li}^6\text{I}$  scintillator was used to provide neutron detection in the energy region below about 6 Mev. The signal amplitudes versus energy differed from the Pilot-B signals but contained the same general features for the flux spectrum measured. The signal current from the  $\text{Li}^6\text{I}$  detector was handled in the same way as for the Pilot-B and Detector 2A currents, except that no peak reading was made. Tape Channel T-3 was used for the gated signals (compressed 14.2-Mev period and PCO-coded), and VCO Channel C was used for the time record of the entire compressed signal.

**C.1.4  $\text{LiI}$ .** A normal  $\text{LiI}$  scintillator, Detector 4, was included to measure background-gamma rays. The data from this detector was used to compensate for the effect of the gamma-ray sensitivity of the  $\text{Li}^6\text{I}$  detector. The signal currents from the latter received the same treatment as did the  $\text{Li}^6\text{I}$  detector currents. Tape Channel T-4 and VCO Channel A were used to record this signal.

**C.1.5 Blank Detector.** Detector 5, the blank detector, was identical with the other detectors except that no scintillator was present. The detector was used to measure any direct-radiation effects or electromagnetic-signal effects on the circuits and photodiodes themselves. Signal treatment was identical with that for Detectors 3 and 4. Tape Channel T-6 and VCO Channel 13 were used for this signal.

## C.2 POD 4, SHOT TEAK

This pod was placed at a range of approximately 170,000 feet below the burst. At this low altitude, the time-of-flight method breaks down. Furthermore, because the flux levels drop off as the inverse time of arrival cubed ( $t^{-3}$ ), the radiation intensities and hence the detector currents are small. In order that the detector signal voltage could be large enough, a high impedance load was required. The Log-R compressors used in Pods 2 and 3 presented low-impedance loads and thus could not be used. It was necessary to provide enough range of sensitivity to bracket the uncertainties in estimated fluxes and in distance to burst by the use of multiple detector channels.

**C.2.1  $\text{CsI}$ , Detector 1.** This detector integrated the prompt-gamma rays. Its signal was impressed on VCO Channel 11 through the normally open gate of a peak reader, which was controlled by the timer (Figure C.2). In contrast to Pods 2 and 3, the timer program was initiated by the gamma-ray signal from the Pilot B Detector 2B.

**C.2.2 Pilot B, Detector 2.** The Pilot-B scintillator in this detector contained approximately

three times the volume of scintillator material in the Pilot-B detectors for Pods 2 and 3. This increase in volume was required to give additional sensitivity. Two of the photodiodes viewing the scintillator constituted Detector 2B. The integral and the peak value of the signal from Detector 2B were measured by the normally closed integrate-and-hold circuit and by the ordinarily closed peak reader. The gamma-ray signal from Detector 2B was used to initiate the timer program. The latter accomplished the following functions: (1) closed the gate of the normally open gamma-ray integrator circuit at 650  $\mu$ sec (these are typical times) after gamma-ray arrival time; (2) opened the normally closed gates for Detector 2B at 650  $\mu$ sec for a period of 370  $\mu$ sec to permit measurement of 14.2-Mev neutron flux; and (3) operated the gated mixers to select the direct signal for neutron arrival and PCO code for the balance of the measurement (see Detectors 3, 4, and 5, below). Detector 2A consisted of four photodiodes. Its signal was integrated by a PCO whose output amplitude modulated the transmitter directly. This detector channel measured the total dose accumulated during the flight of the pod.

**C.2.3 Pilot B, Detector 3.** Detector 3 consisted of a scintillator similar to that in Detectors 2A and 2B, except that all six photodiodes were used in parallel to provide maximum sensitivity. The neutron-signal current was presented to VCO Channel E. The signal was also recorded directly on Tape Channel T-2 for a period of 370  $\mu$ sec, which started 650  $\mu$ sec after gamma-ray arrival. From this total time lapse of 1,020  $\mu$ sec to the end of the measurement, the neutron signal was measured by the PCO and recorded also on Tape Channel T-2.

**C.2.4 Pilot B, Detector 4.** This detector channel was identical to the channel in Detector 3, except that its sensitivity was a factor of 6 smaller. Tape Channel T-3 and VCO Channel C were used for Detector 4.

**C.2.5 Blank, Detector 5.** This detector channel duplicated the channels in Detectors 3 and 4, except that no scintillator was used. Its output was a measure of interfering signals resulting from gamma-ray and electromagnetic effects on the detector circuitry and photodiodes.

### C.3 POD 4, SHOT ORANGE

This pod was identical to Pod 4 for Shot Teak, except for differences in timing. The gate signal operated 330  $\mu$ sec after gamma-ray arrival, at which time it provided a pedestal 180  $\mu$ sec long (Figure C.3).

### C.4 GENERAL DESIGN TECHNIQUES

Printed-circuit techniques were used for all of the detector electronics. Figures C.4 through C.15 are schematics of the various circuits indicated in the block diagrams of Figures C.1 through C.3. Figures C.16 through C.27 are photographs of the individual printed-circuit components and the chassis-mounting arrangements. The calibration of the overall system including the calibration of the detector electronics is discussed in Appendix D.

### C.5 INTERNAL TIMING FOR DETECTOR ELECTRONICS

The measurements made in the pods employed electronic switching in order to make maximum use of the available information channels. The times at which the switches operated were determined from neutron-flight times. Because these times were different for each pod, it was convenient to define certain time intervals in terms of the time of flight:

- $t_{\gamma}$  = time of arrival of prompt-gamma-ray pulse; all times in the pod are measured from this time
- $t_{14}$  = time of arrival of a 14.2-Mev neutron
- $\Delta t_{14}$  = full width of 14.2-Mev neutron pulse

$T_1$  = delay time from  $t_\gamma$  to a time before  $t_{14}$  chosen so that all neutrons arrive after  $t_\gamma + T_1$ . The value for  $T_1$  was made short enough to allow for pod position errors of  $\pm 10$  percent.

$$= t_{14} - t_\gamma - \Delta t_{14} - t_{14}/10$$

$\Delta T_1$  = time interval chosen to include the 14-Mev neutron group; the width of this time interval was made large enough to go from  $T_1$  to a time that would include all the direct 14.2-Mev neutrons with a pod position error of  $\pm 10$  percent.

$$= 2 \left[ (\Delta t_{14}) + (t_{14}/10) \right]$$

$\Delta T_2$  = total time of the neutron measurement;  $\Delta T_2$  extends from  $T_1$  to the end of the measurement as determined by the recorder program.

In terms of the velocities of the gamma rays and neutrons, the difference in arrival time is:

$$t_{14} - t_\gamma = R_{km} \frac{c - v_{14}}{c v_{14}} = 16.12 R_{km} \mu\text{sec}$$

Where:  $R_{km}$  = slant range from detonation point  
 $c$  = gamma-ray velocity  
 $v_{14}$  = velocity of 14.2-Mev neutron

then,

$$\Delta t_{14} = \frac{17.7}{9} R_{km} \mu\text{sec} = 1.962 R_{km} \mu\text{sec}.$$

#### C.6 INTERNAL DETECTOR PROGRAM

The internal program for the detector circuits was operated from the prompt-gamma-ray pulse. This pulse initiated a delay  $T_1$  (Table C.1 and Figure C.28) from the gamma-ray pulse to a time just before the first neutron arrivals from the 14-Mev group. The delay  $T_1$  was different for each pod and was made short enough to allow for pod-position errors. At the end of the delay, a univibrator was fired, providing a gate  $\Delta T_2$  that shut off the prompt-gamma-ray integral gate for the remainder of the measurement time. The  $T_1$  signal also actuated a univibrator of duration  $\Delta T_1$ , chosen to encompass the arrival of the 14-Mev neutron group. The signal was used to open the gate for the 14-Mev neutron integral and peak measurements. It also operated the gated mixers by switching the open gate to the output of the Log-R for the 14-Mev signal and back to the 100-kc PCO for sampling the output during the neutron time history after the 14-Mev group. The timing signals were all presented to a 10- $\mu\text{sec}$  univibrator and recorded on Tape Channel T-1.

#### C.7 DETECTOR DATA OUTPUTS

The outputs from the detector electronics in Pods 2 and 3 were as follows:

RDB Channel E, neutron time history from Pilot B  
 RDB Channel C, neutron time history from  $\text{Li}^7$   
 RDB Channel A, neutron time history from normal  $\text{LiI}$   
 RDB Channel 10, prompt-gamma-ray integral from  $\text{CsI}$   
 RDB Channel 11, 14-Mev neutron integral from Pilot B  
 RDB Channel 12, 14-Mev neutron peak from Pilot B  
 RDB Channel 13, time history from blank detector  
 Direct Tape Channel T-1, time-signal record  
 Direct Tape Channel T-2, 14-Mev direct signal plus the PCO record of neutron history from Pilot B

Direct Tape Channel T-3, same from Li<sup>4</sup>I  
 Direct Tape Channel T-4, same from normal LiI  
 Direct Tape Channel T-5, same from blank detector  
 Direct Tape Channel T-6, calibration for VCO's  
 Direct Tape Channel T-7, VCO composite from summing amplifier  
 Direct Tape Channel T-8, spare

The real-time output amplitude modulated the transmitter directly and continuously.

### C.8 MAGNETIC-TAPE RECORDER

The data was collected during a period in which total blackout was expected. Reliability of the telemetry link required the use of a data-storage device. The purpose of the magnetic-tape recorder was to overcome the limitations inherent in the use of real-time telemetry, namely, blackout susceptibility, limited-frequency band width in RDB channels, and limited number and kind of channels.

The pod data-recording system was composed of several subcomponents including electronic data-coding devices, a continuous-loop magnetic tape recorder, a self-programming system playback amplifier, and a commutator. The tape-recorder unit consisted of a continuous loop (about 10 inches in circumference) running at 60 in/sec. The total recording time was about 160 msec. There were eight data tracks on the magnetic tape. A high-frequency (350 kc) bias signal was provided, amplified, and mixed with the data signal. The same signal was used to drive the erase amplifier (Figure C.29). Seven impedance-converter channels were used to prepare signals for recording and to provide proper recording current to the recording heads. Five of the impedance-converter channels were compensated to emphasize low-frequency response, which was required for the direct recording of detector currents. The remaining two channels were linear mixers, one of which constituted the RDB subcarrier complex and its calibration and the other the direct timing signal.

Eight RDB VCO's were used in multiplex to provide eight channels of narrow-band-width information. A 100-kc reference signal was included in the RDB complex to supply a means for compensating tape-transport speed fluctuations.

A linear impedance converter impressed the RDB data complex on one track and the RDB calibration complex on a second track. The remaining six tape tracks were used for the more rapidly varying signal currents, which required greater frequency band width than that afforded by the RDB subcarrier. These last six tracks could record signals with rise times shorter than 10  $\mu$ sec. The five compensated impedance converters were used for data channels. The remaining linear impedance converter was used for the timing record. An integrated control system permitted exterior manual control of functions and transfer to interior automatic control.

Figure C.29 is a simplified block diagram of the RDB recording channel shown in the record mode. The VCO is calibrated by impressing a regulated 3-volt-dc signal to swing the VCO output frequency. The VCO is adjusted to a predetermined frequency deviation for this condition. Another calibration point is the preset center-frequency output, or arbitrary zero point. Information signals vary the VCO output frequency in proportion to the instantaneous input-signal amplitudes. The output signal is added to the bias-oscillator signal (350 kc) and is applied to the magnetic tape through the record head. The summing amplifier is a linear amplifier used to combine the many VCO outputs introducing intermodulation distortion in the mixing process. During the playback mode, the record and erase heads are short-circuited. The playback system operates continuously.

A separate record-erase-playback head combination is used for establishing the calibrated output from the VCO. Prior to actual use of the head, an external calibration-erase switch is actuated to erase any spurious signals present on the tape.

Figure C.30 is a simplified block diagram of an amplitude channel shown in the record mode. The information input and bias signal (350 kc), after being processed in the impedance converter and the isolation amplifier, are added in their common input to the record head. The erase

head continuously erases, except when the recorder is in the playback mode. The ganged relay contacts shown in Figure C.30 are transferred for playback-mode operation.

Figure C.31 illustrates, in simplified block-diagram form, the basic system transfer channel that controls the tape recorder so that it is automatically transferred from record to playback mode. The transfer initiating pulse causes two one-shot multivibrators to change operating conditions in sequence so that Relay K 310 removes energizing current from the record-playback Relays K 411, K 412, K 413, and K 414 at the completion of the data-recording interval. The relays ground the inputs of the record heads. The playback condition then continues for repeated playback of the recorded information. The holding contacts of K 310 are available for control by an external program. This makes it possible to make trial runs of the recorder prior to the actual test measurement and also provides the means to calibrate the amplitude channels just before the actual run.

The input signals presented to the equipment must be limited to 7 volts, peak to peak. The input impedance is about 100,000 ohms in the compensated channels and about 500,000 ohms in the uncompensated channels.

Three types of program control of the recorder were provided in the pods. A stepping relay (ledex) energized through the umbilical connector at the bottom of the pod, provided a choice of three conditions: internal power (batteries), external power, and off. The second program control was initiated at ejection, and after suitable delays, the recorder and all other components in the pod were put through the automatic in-flight self-calibration sequence. The third program control was initiated by the gamma-ray signal, which triggered the one-shot multivibrators which, in turn, transferred the recorder from record to playback mode.

#### C.9 TELEMETRY TRANSMITTER

The transmitter used to telemeter the information presented by the recorder was a modification of the Tele-Dynamics 1002A. The transmitters were crystal-controlled at frequencies of 237, 239, 241, and 245 Mc.

#### C.10 POD CONSTRUCTION AND ANTENNA SYSTEM

The instrumentation described above was adapted to pods designed and tested by ABMA during the test-launching of Missile 45 at Cape Canaveral. Minor structural modifications within the pod were necessary to accommodate the instruments, and a special umbilical closure system, to maintain the integrity of the electromagnetic shield, was added. The tail section of the pod was insulated from the main instrument portion. The transmitter output (unbalanced to ground) was connected with the instrument section as ground and the tail section as the driven element. In effect, the pod became a half-wave dipole driven at the center. The use of a shorted stub tuning element, adjusted for proper loading, gave the added advantage of preventing the entry of electromagnetic signals. The electromagnetic-wave impedance across the insulated section was nearly a short circuit for all frequencies below the transmitter operating frequency. Because the frequency spectrum of the electromagnetic effect had negligible components above 100 Mc, the pod was an effective shield against such effects. The pods were tuned individually for minimum-standing-wave ratio prior to use.

The instrumentation was designed for operation at one atmosphere, thus requiring that the pods be pressurized. All pod joints were provided with gaskets to maintain atmospheric pressure. Suitable valves were installed to permit pressure testing and flushing with dry nitrogen. This flush removed the air and yielded an inert atmosphere inside the pod. During discharge, the batteries generated hydrogen gas and the nitrogen atmosphere prevented an explosion, which could occur if air remained in the pods.

#### C.11 INTERNAL POWER SUPPLY

Several types of batteries were considered for use in the pods. From among those giving



the maximum energy per cubic inch, the Yardney silver cells were chosen, because they had a form factor compatible with the available spaces within the pod.

The Yardney cells were rechargeable and were prepared for use as follows: (1) Cells were filled and allowed to stand for 72 hours. (2) A forming charge was given the cells. (3) The cells were discharged. (4) The cells were given the final charge as near flight time as possible.

Each pod contained battery packs as follows: (1) B-supply made of four packs of 34 and four packs of 30 Yardney HR-02 cells, all in series; (2) supply for filaments and motors made of three packs of 14 Yardney HR-01 cells, in series parallel; (3) C-supply for regulator reference and circuit bias made of six 30-volt Burgess U-20 dry cells; (4) C-supply for Log-R bias made of two packs of 30 Yardney HR-02 cells; and (5) high-voltage supply power source made of five Yardney HR-02 cells.

The high voltage required by the detector photodiodes was provided by a transistorized 2,500-volt supply manufactured to NRL specifications. Semiconductor devices are susceptible to damage by large neutron and gamma-ray fluxes. In order to avoid the effects of transient neutron damage, the high-voltage supply was used to charge a bank of filter condensers chosen large enough to provide all the detector current without dropping below the detector-voltage saturation level. Rectification in the transistorized supply was effected by use of vacuum diodes instead of the customary semiconductor diodes. The use of vacuum diodes was necessary to avoid power-supply shorting that could result from neutron and gamma-ray damage to semiconductor devices.

#### C.12 RECEIVING ANTENNA

A standard 4-turn helical antenna was used for telemetry reception. The directivity gave a gain of approximately 10 decibels. The major lobe measured approximately 20 degrees half angle in both vertical and horizontal planes (with the antenna pointed in a horizontal direction). Figures C.32 and C.33 give the vertical and horizontal field patterns.

The three receivers (one for each pod) were all coupled to the single antenna by means of a multicoupler which isolated each receiver and prevented interaction between them.

#### C.13 RECEIVER-DISCRIMINATOR SYSTEM

Telemetry receivers 1670E, supplied by the Nems-Clark Company, were used. The IF band width of this model is 500 kc, and the noise figure is 10 decibels. The signal-level current was brought out of the receiver for recording on the oscillograph (Figure C.34). The video signals from all receivers were recorded directly on the tracks of an Ampex FR-100 tape recorder. One of the receiver outputs was connected to the data-reduction discriminators during the flight of the pod. The video signal from all the receivers was recorded on film by means of six Tektronix 541 oscilloscopes and six DuMont 321-A continuous-motion film-strip cameras. Two oscilloscopes with cameras were used for each receiver channel.

During Shot Teak, film speeds and sweep rates were chosen to give a raster on the film, each sweep of which was fast enough to resolve the data. The total film time was long enough to follow the pod from burst time to the end of its flight.

During Shot Orange, the shorter pod-flight times permitted the use of the film motion for the sweep, and the signal merely deflected the scope spot. The two scope camera units per pod were used to provide backup in case of camera failure.

#### C.14 DATA-REDUCTION SYSTEM

The data-reduction system provided for the field installation was incomplete, including only the minimum necessary components for purposes of preliminary data reduction. Figure C.34 gives the block diagram for preliminary reduction of RDB subcarrier data. The discriminators selected the subcarriers and decoded them. The data output of the discriminators was recorded



on a Consolidated oscillograph. The data on the oscillograph paper had to be further reduced in the field by direct manual methods.

The tape-speed-compensation system is an integral part of the data-reduction equipment. A crystal-controlled oscillator provided a stable 100-kc signal record on the pod tape recorder during the record cycle. The signal was transmitted as a part of the RDB complex and was separated at the ground station by the 100-kc discriminator. The output of the latter was a measure of all tape-speed variations and was added as a speed-compensating correction. The preliminary data available in the field was obtained by manual measurement of the received signals, which appeared on the oscillograph print and on the camera film.

TABLE C.1 PLANNED INTERNAL PROGRAM TIME INTERVALS

Pod	Slant Range	$t_{14} - t_7$	$\Delta t_{14}$	$t_{14}/10$	$T_1$ Calculation	$T_1$ Setting	$\Delta T_1$ Calculation	$\Delta T_1$ Setting
	km	$\mu\text{sec}$	$\mu\text{sec}$	$\mu\text{sec}$	$\mu\text{sec}$	$\mu\text{sec}$	$\mu\text{sec}$	$\mu\text{sec}$
Teak 2	9.48	152.8	18.6	18.2	116	110	73.6	70
Teak 3	15.50	250	30.4	29.8	190	180	120.4	100
Teak 4	52.62	849	103.2	101	645	650	408	370
Orange 2	9.69	156.2	19	18.6	118.6	110	76.2	70
Orange 3	14.71	237	28.9	28.3	180	180	114.4	100
Orange 4	25.46	410	50	48.9	311	330	197.8	180

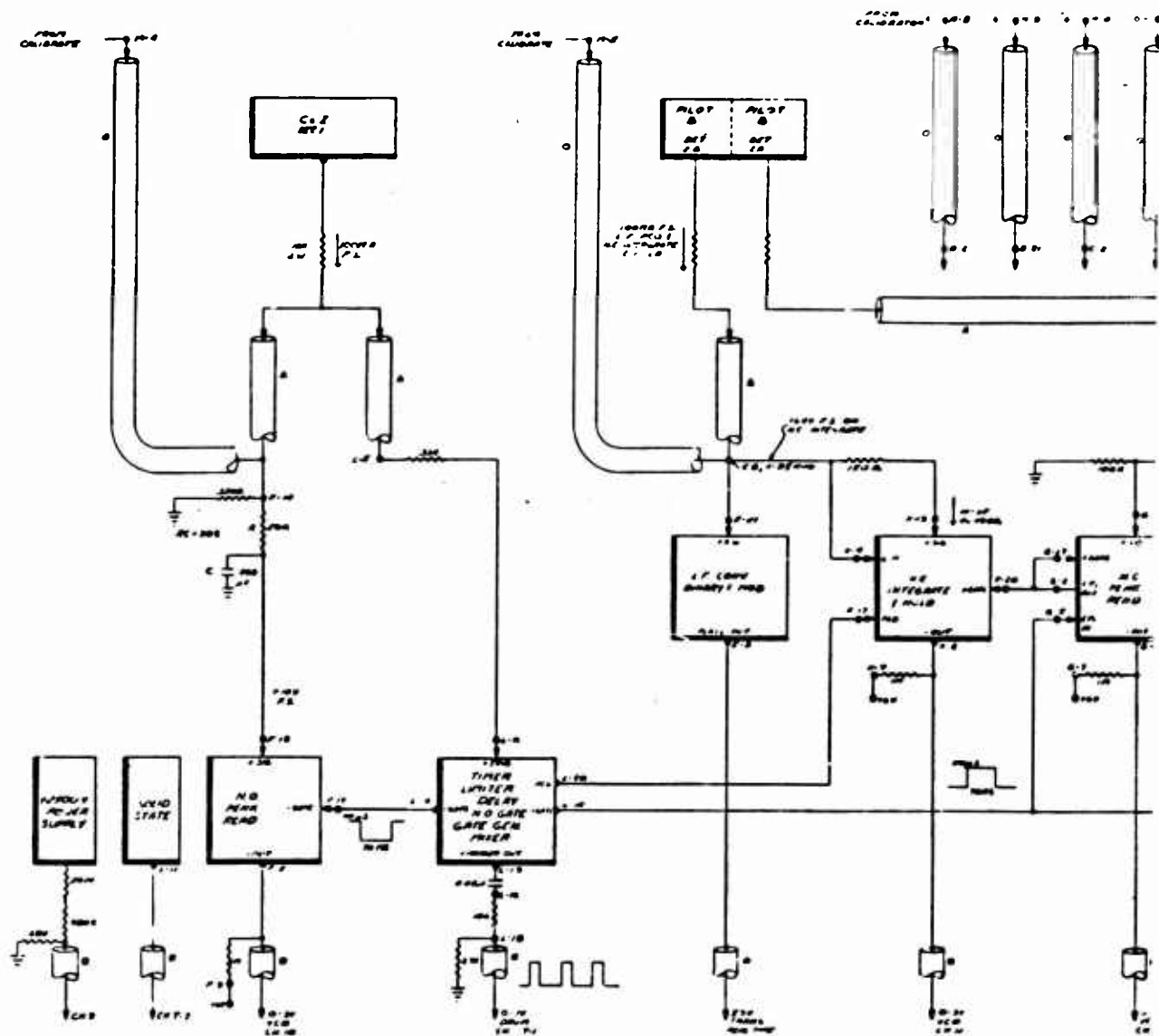
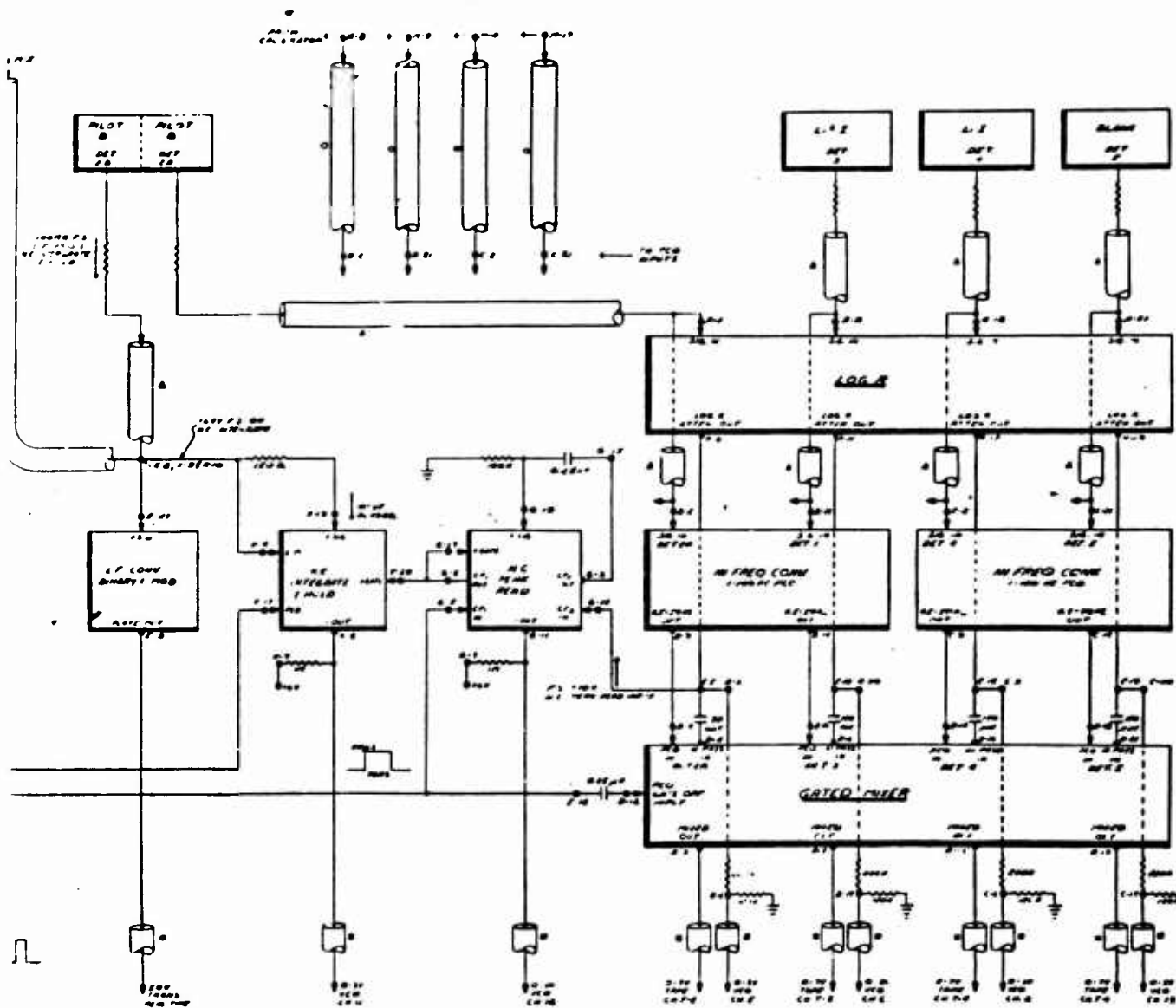


Figure C.1 Detector electronics, upper pods for Shots T





C.1 Detector electronics, upper pods for Shots Teak and Orange.







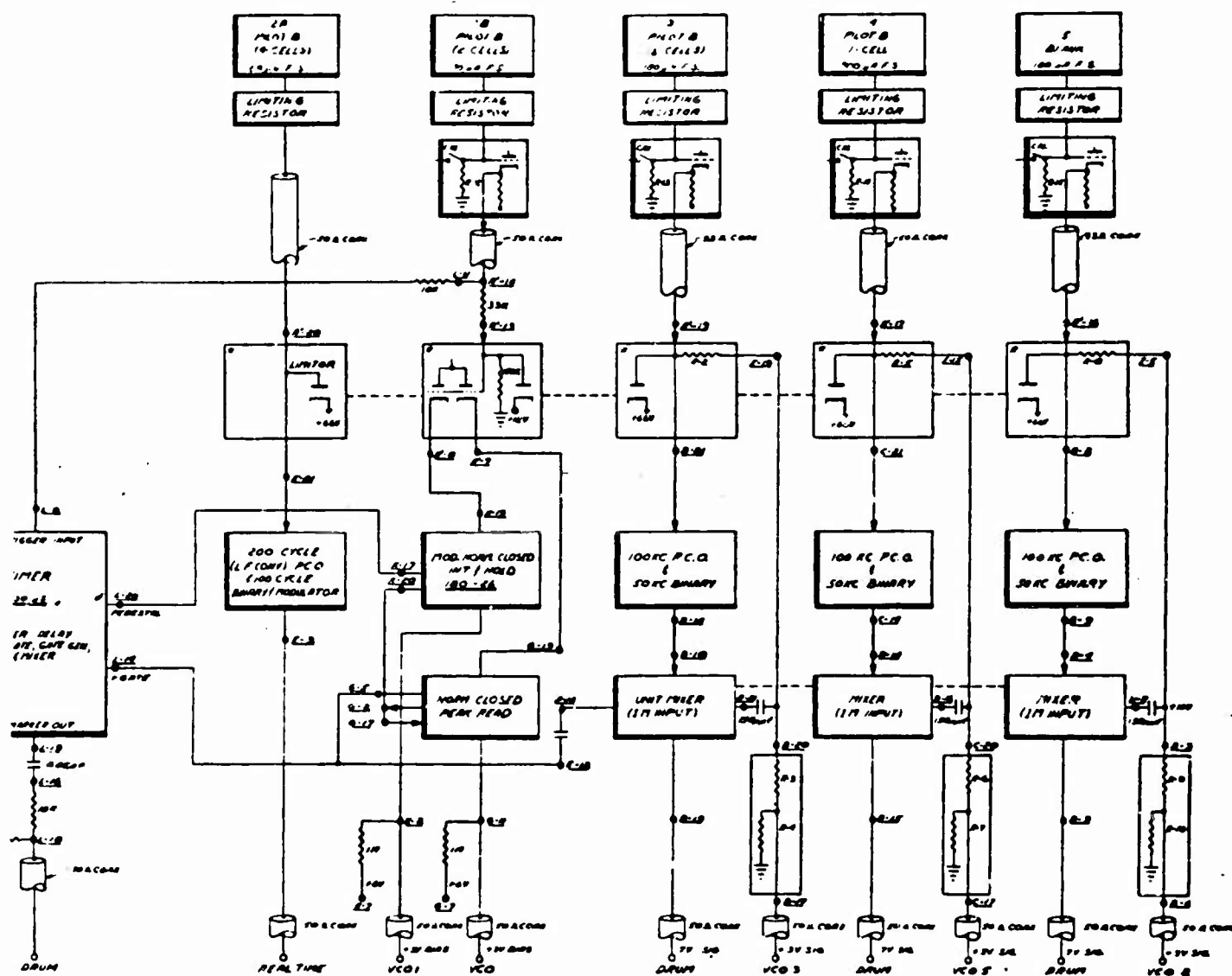


Figure C.3 Detector electronics, lower pod for Shot Orange.



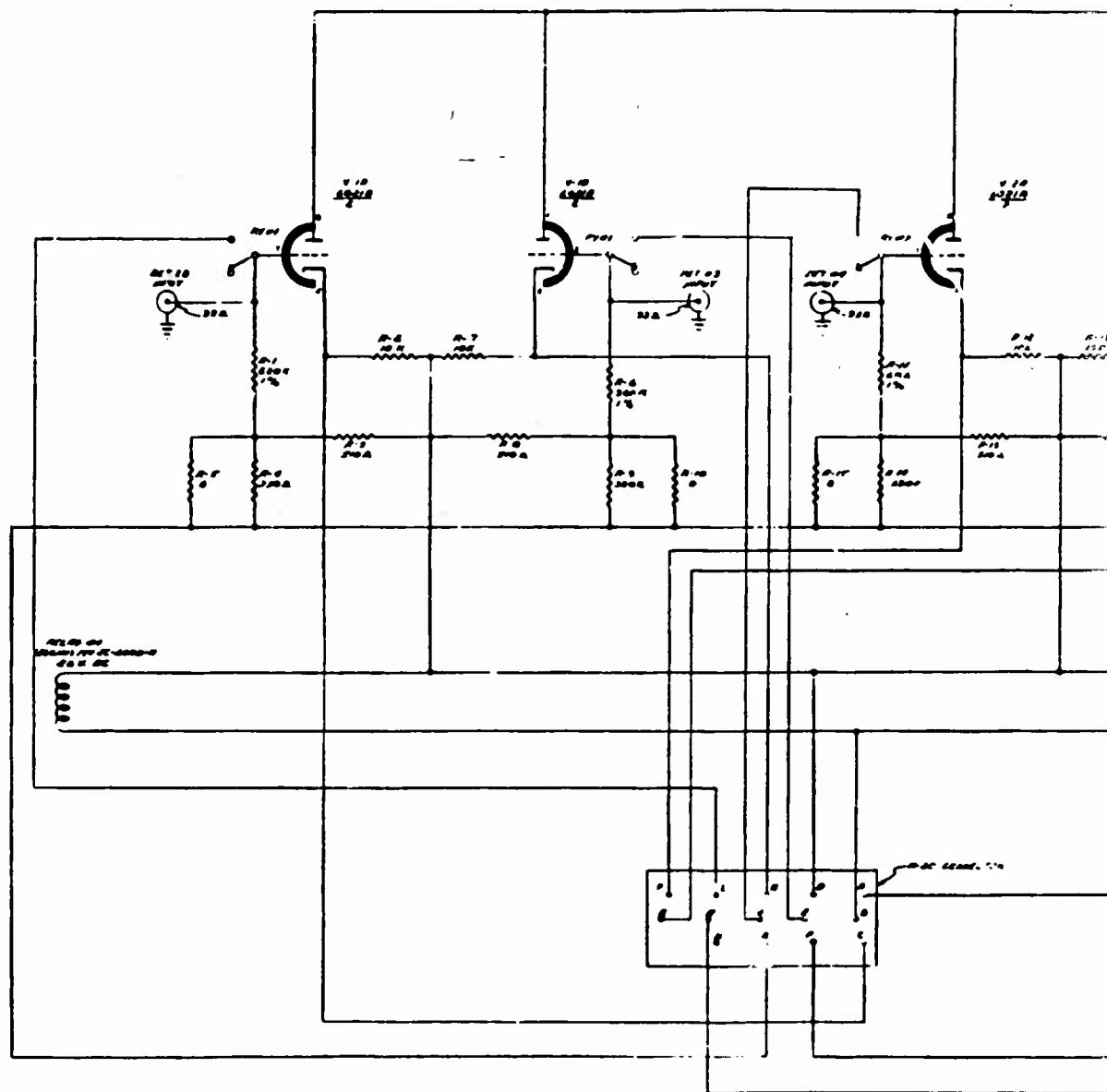


Figure C.4 Detector cathode follower.

1

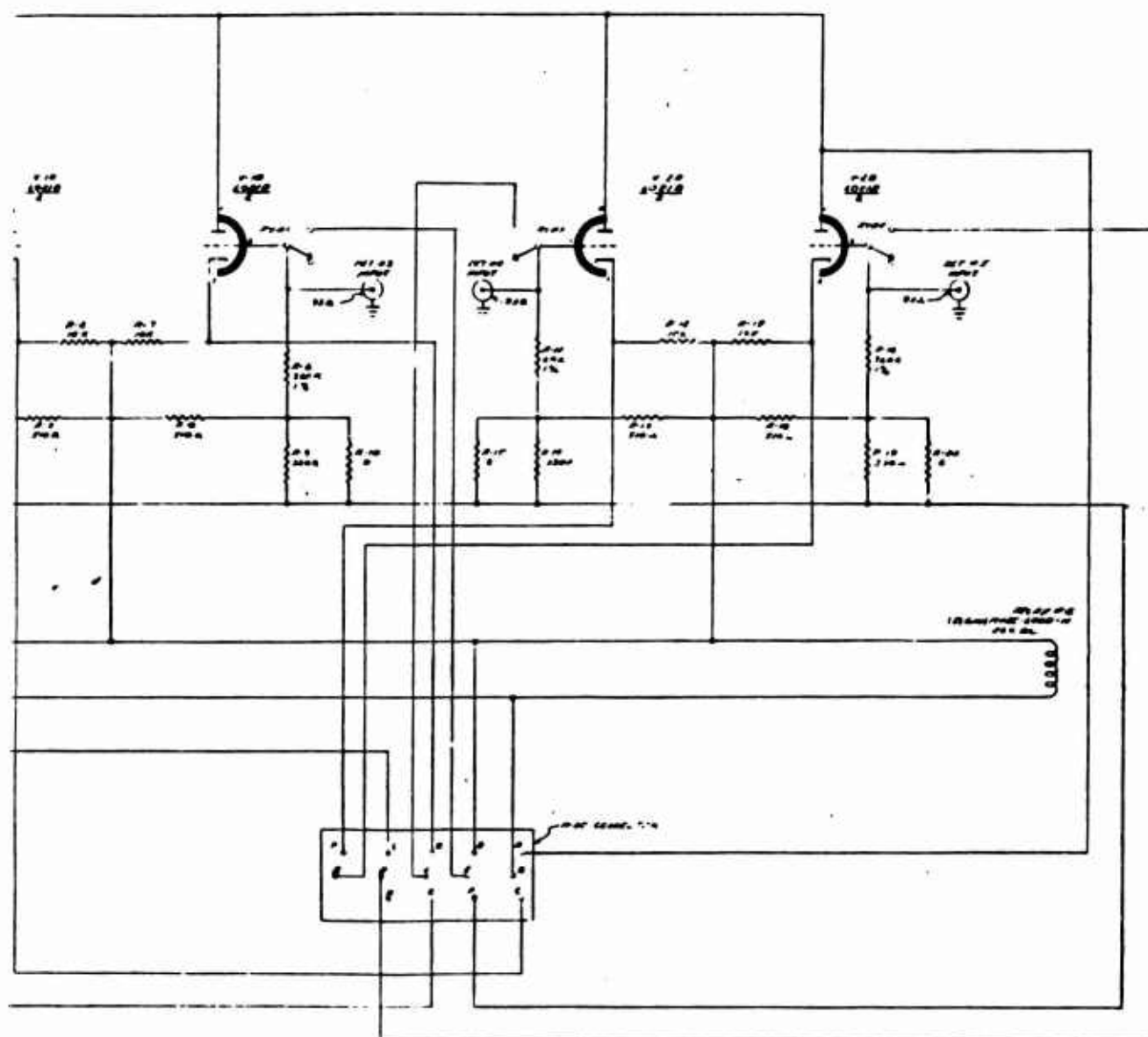


Figure C.4 Detector cathode follower.

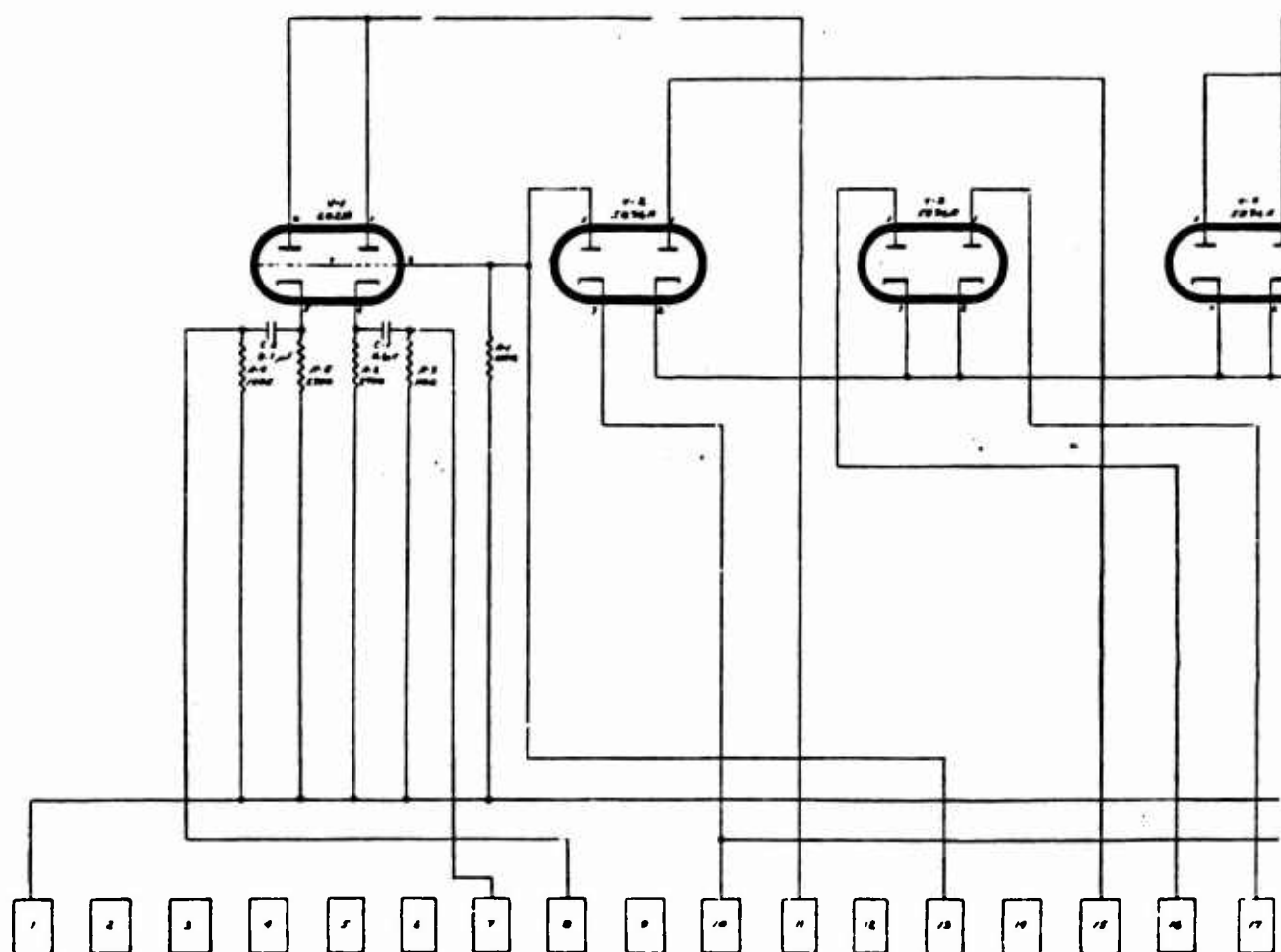


Figure C.5 Signal limiter.

1

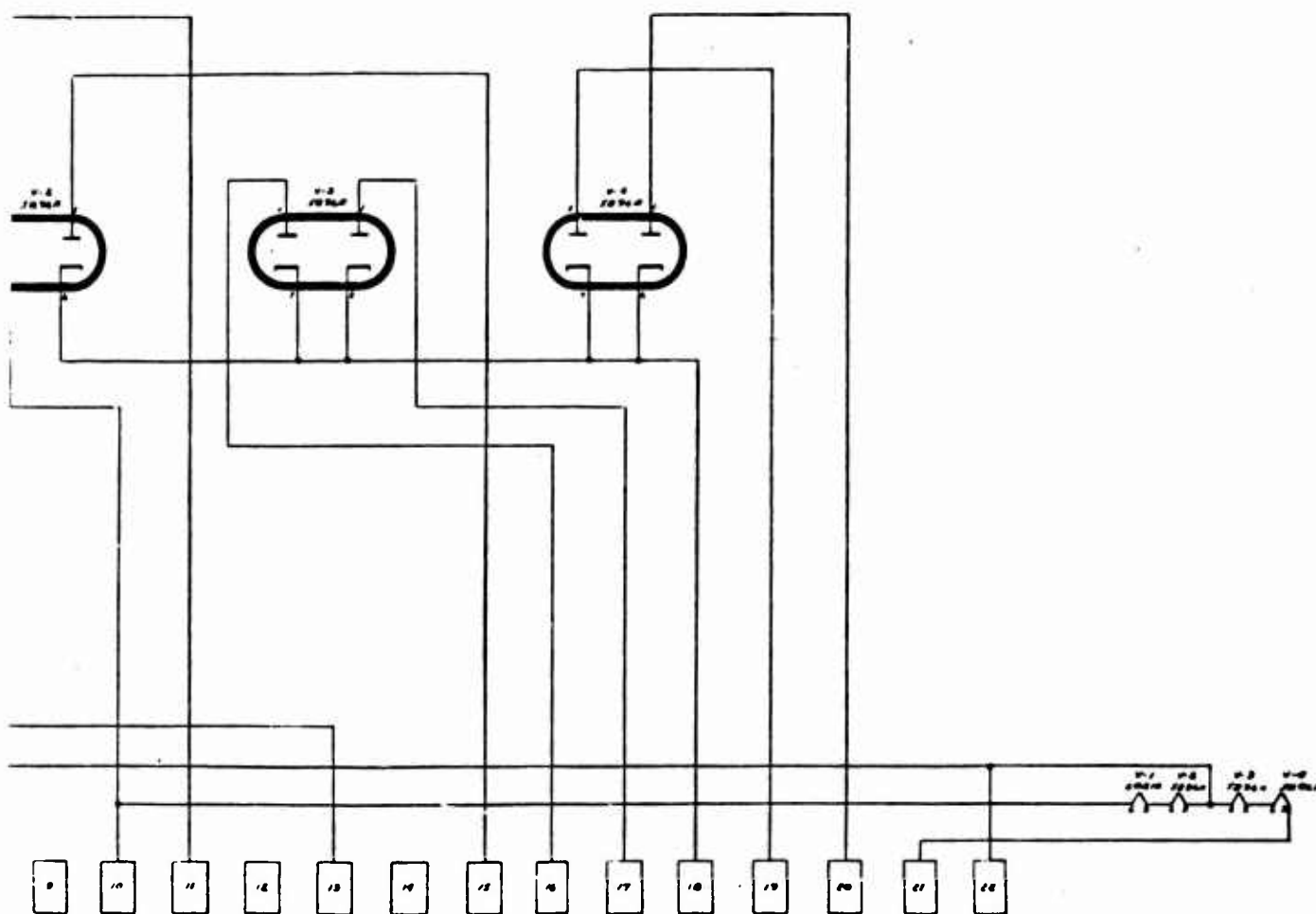


Figure C.5 Signal limiter.

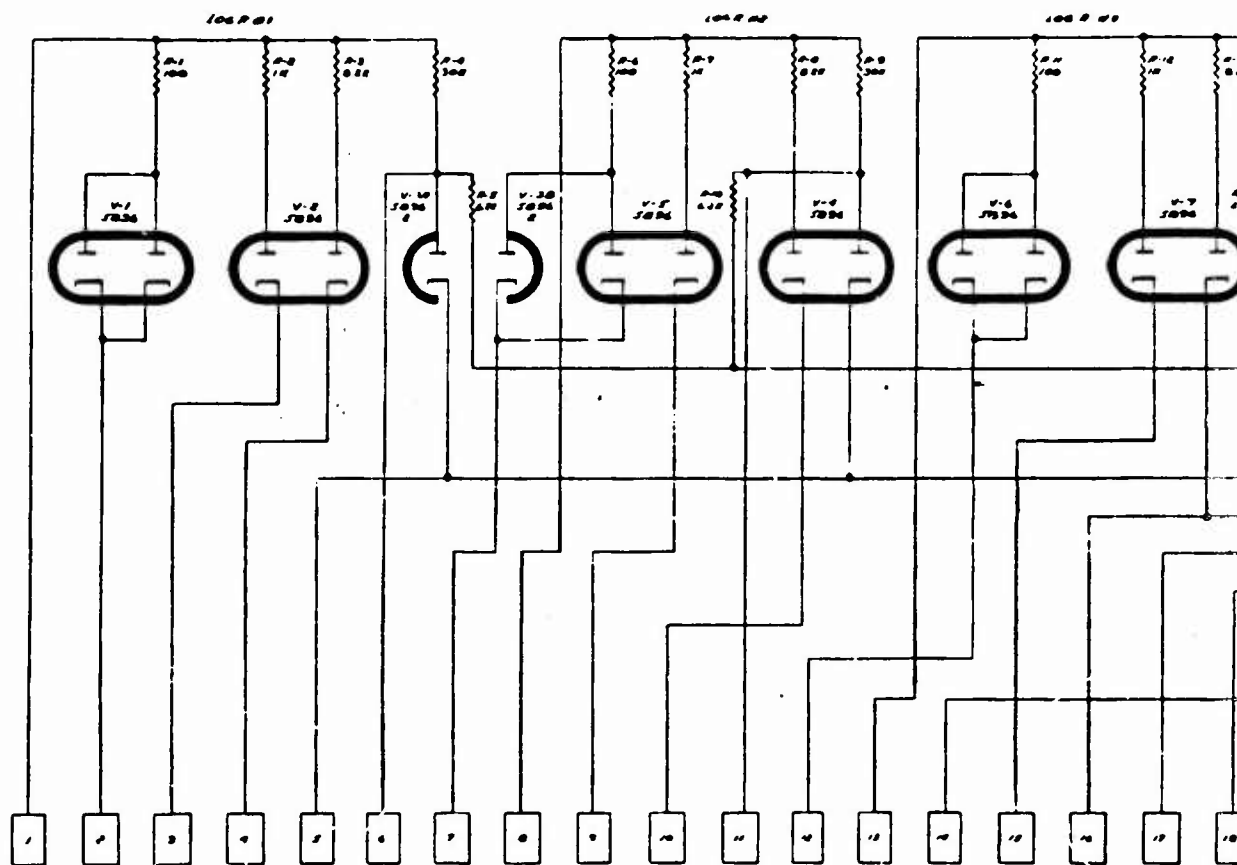


Figure C.6 Log-R circuit.

1

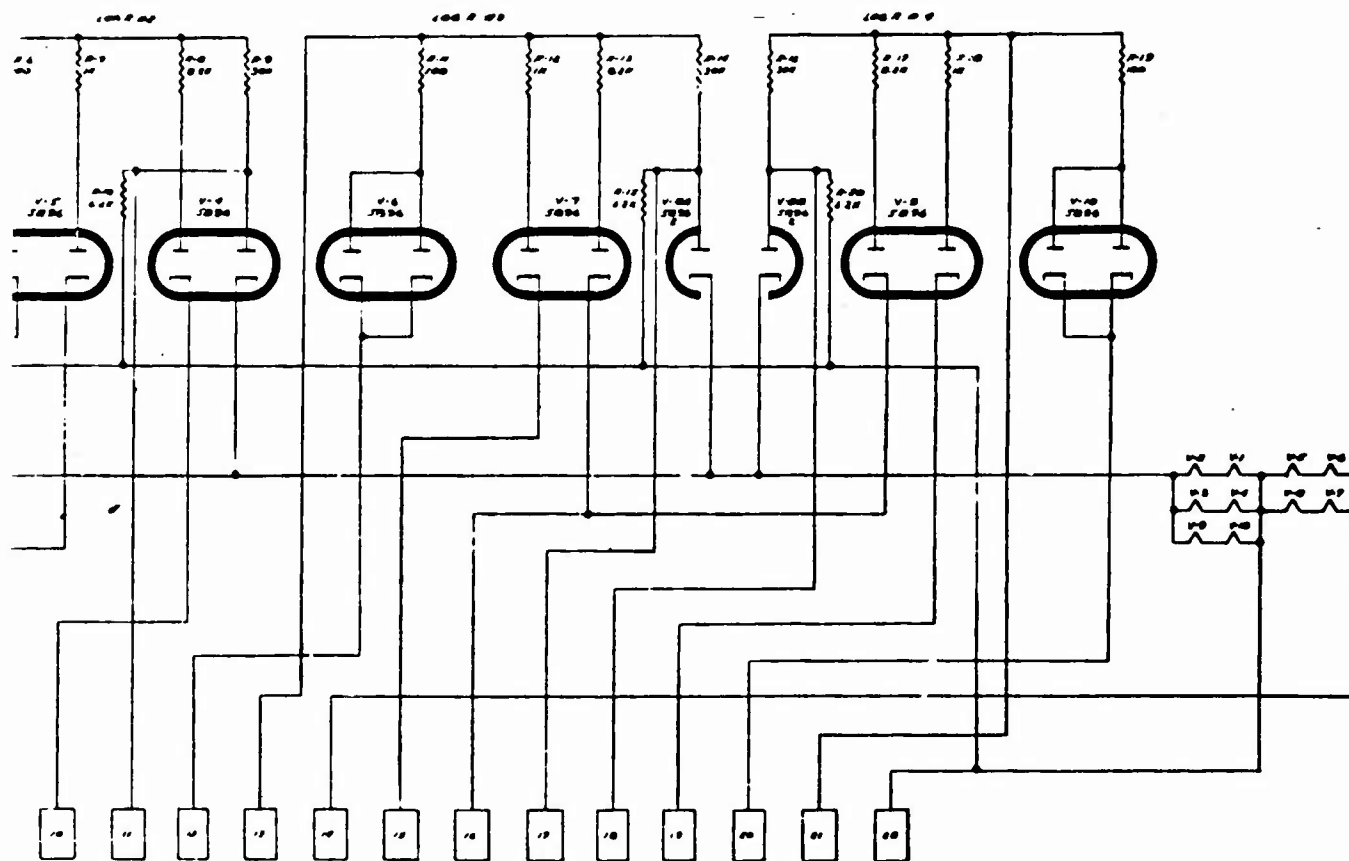


Figure C.6 Log R circuit.

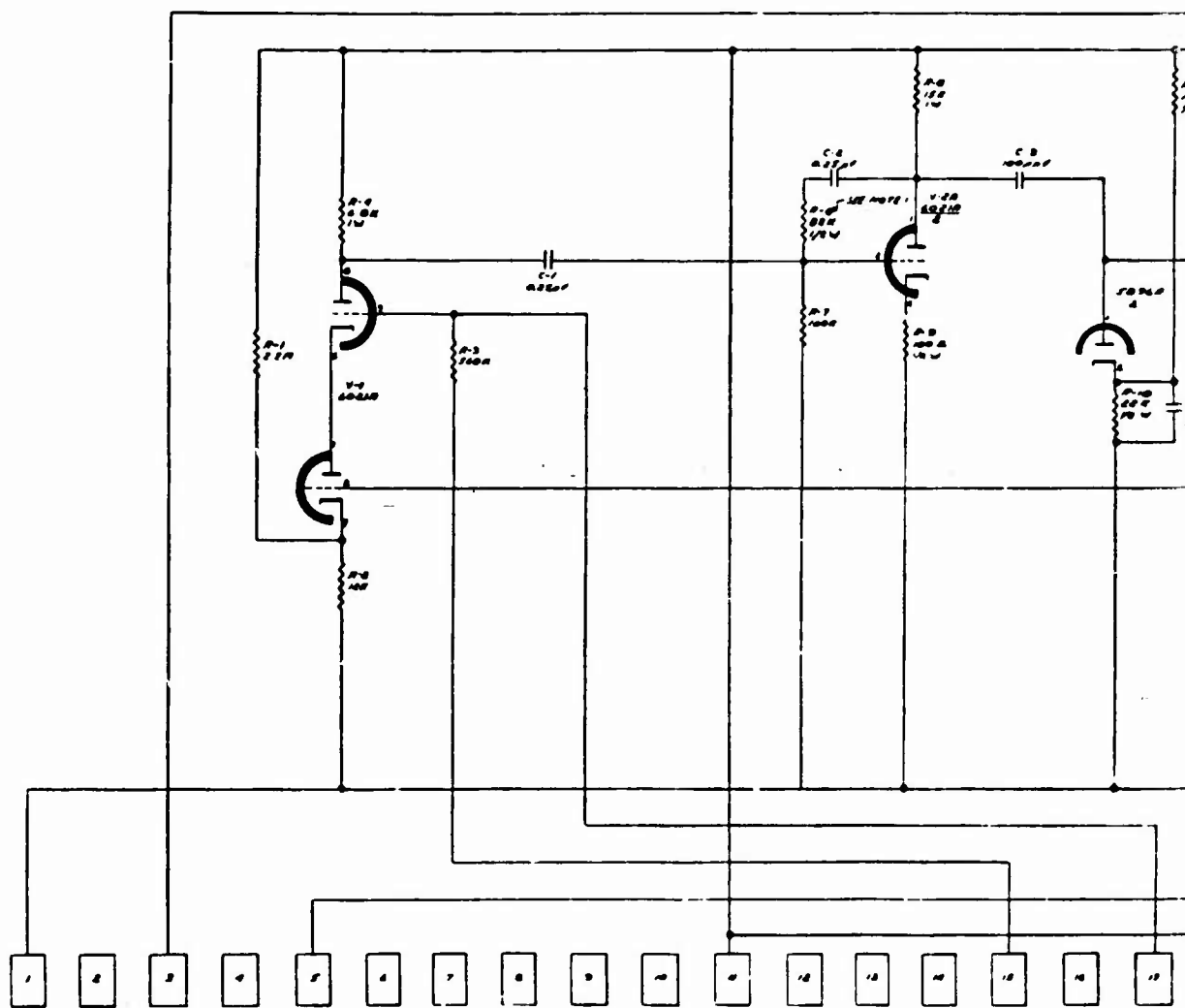
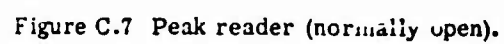
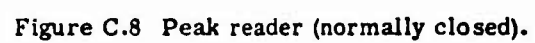


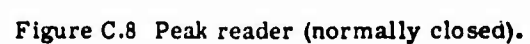
Figure C.7 Peak reader (normally open).

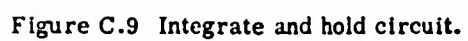
1











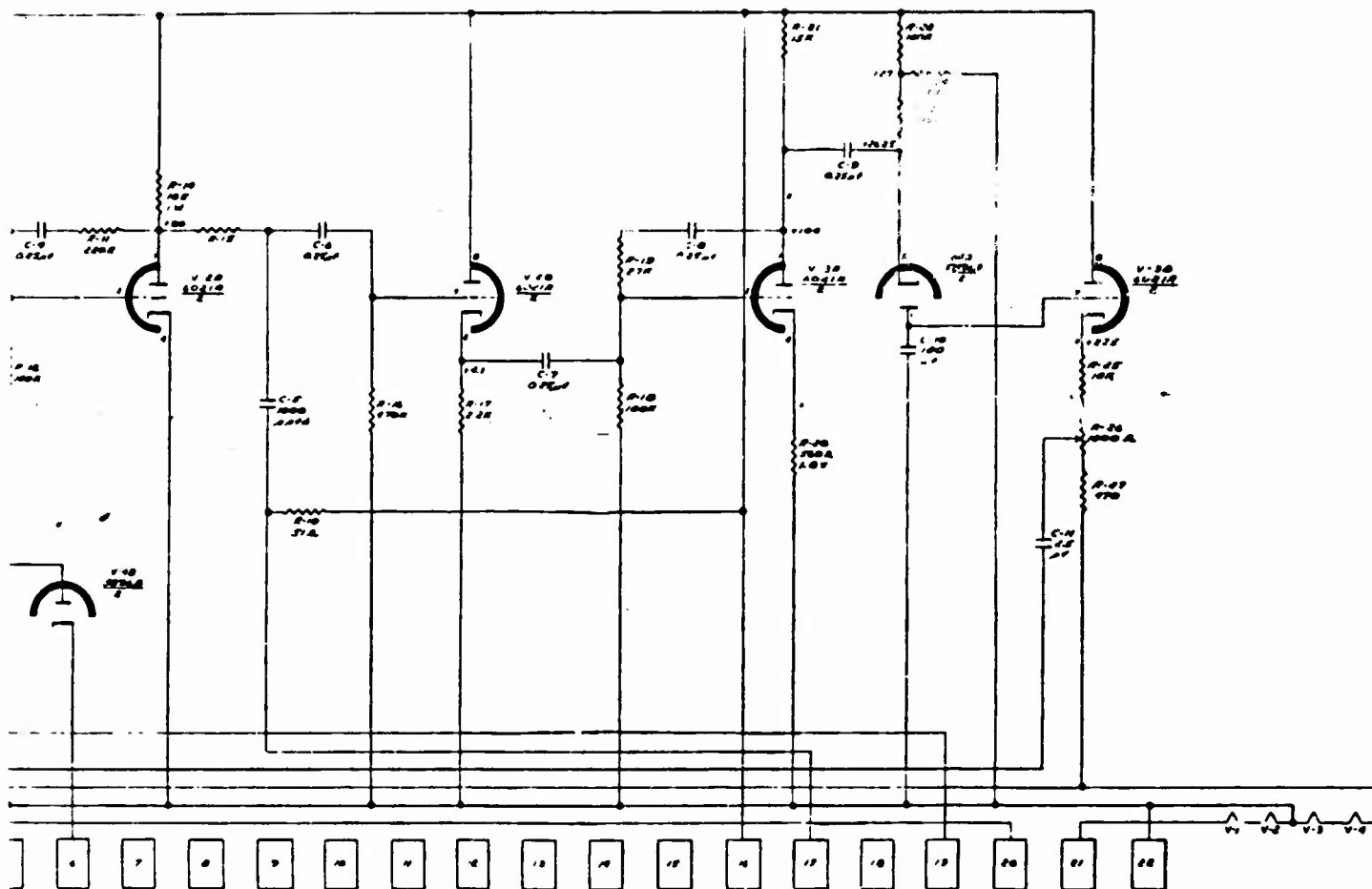


Figure C.9 Integrate and hold circuit.

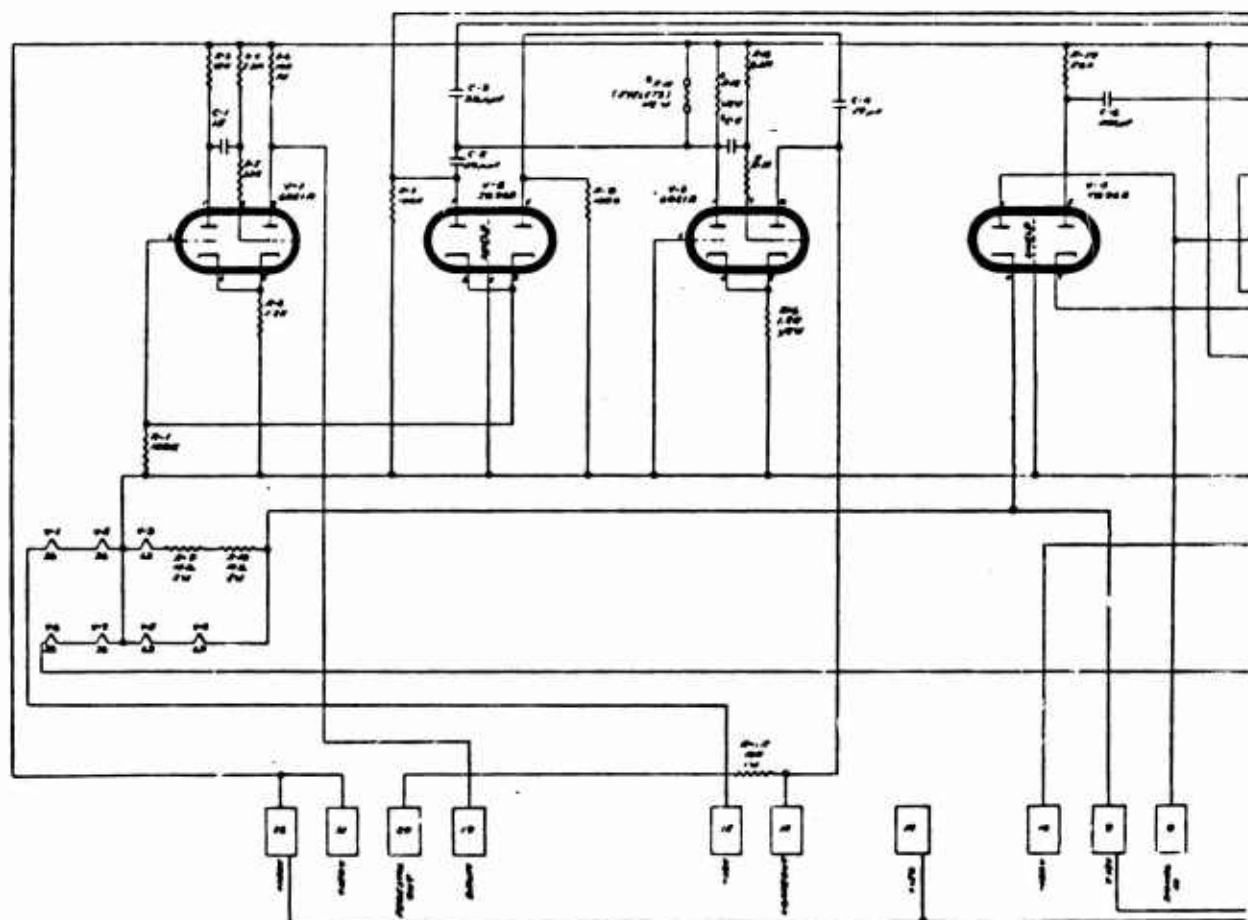
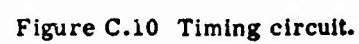


Figure C.10 Timing circuit.

1





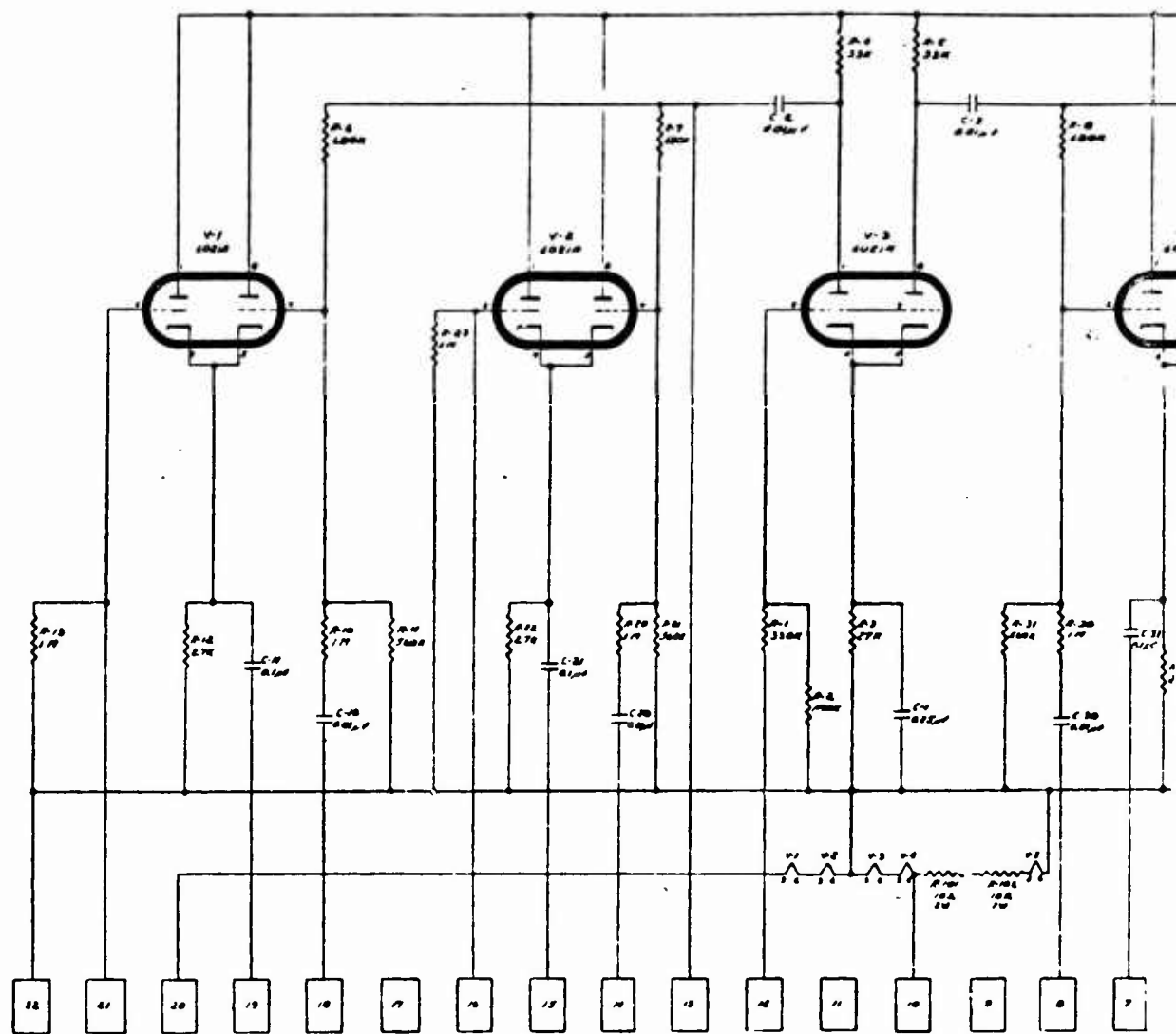


Figure C.11 Mixer gate circuit.

1

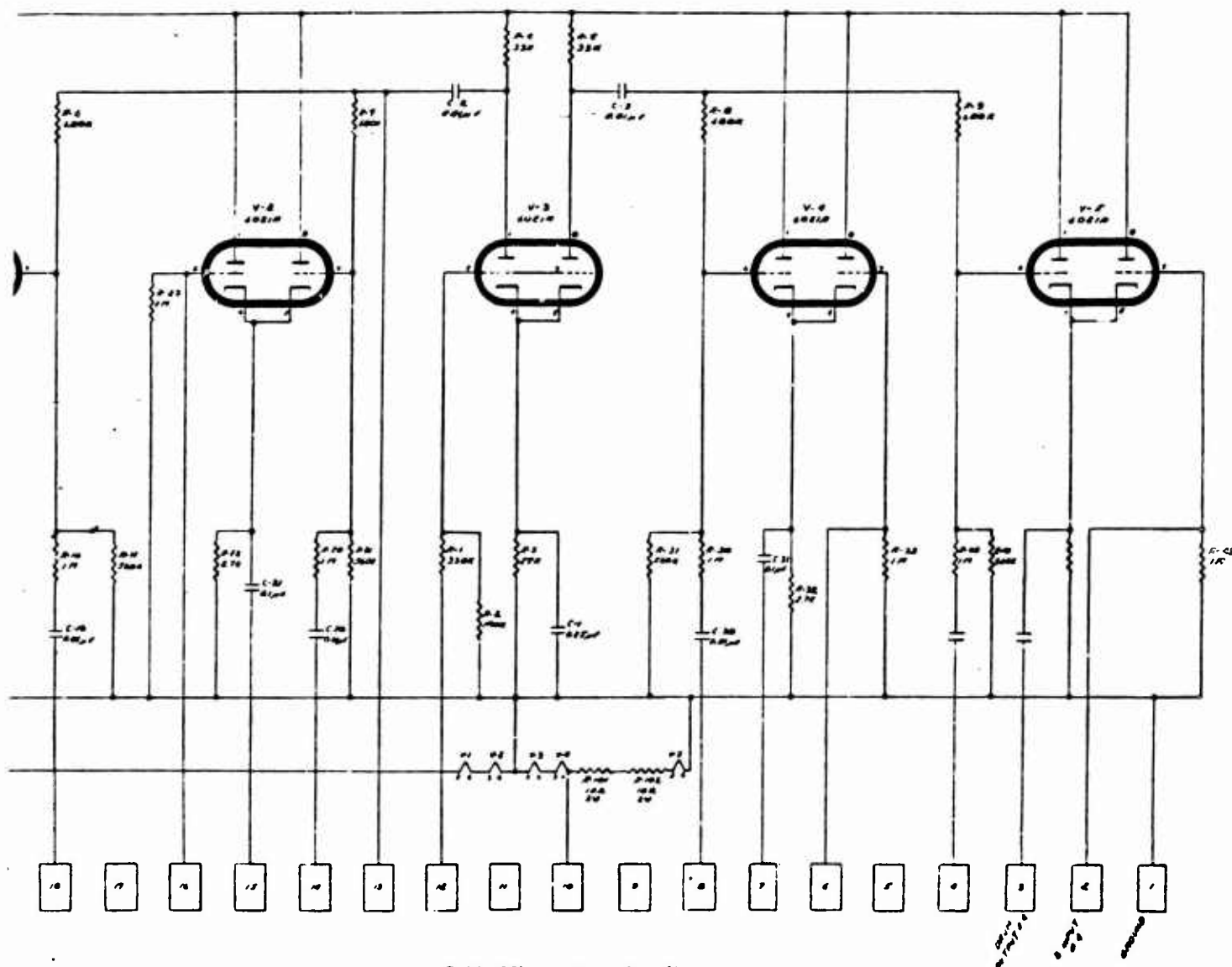


Figure C.11 Mixer gate circuit.

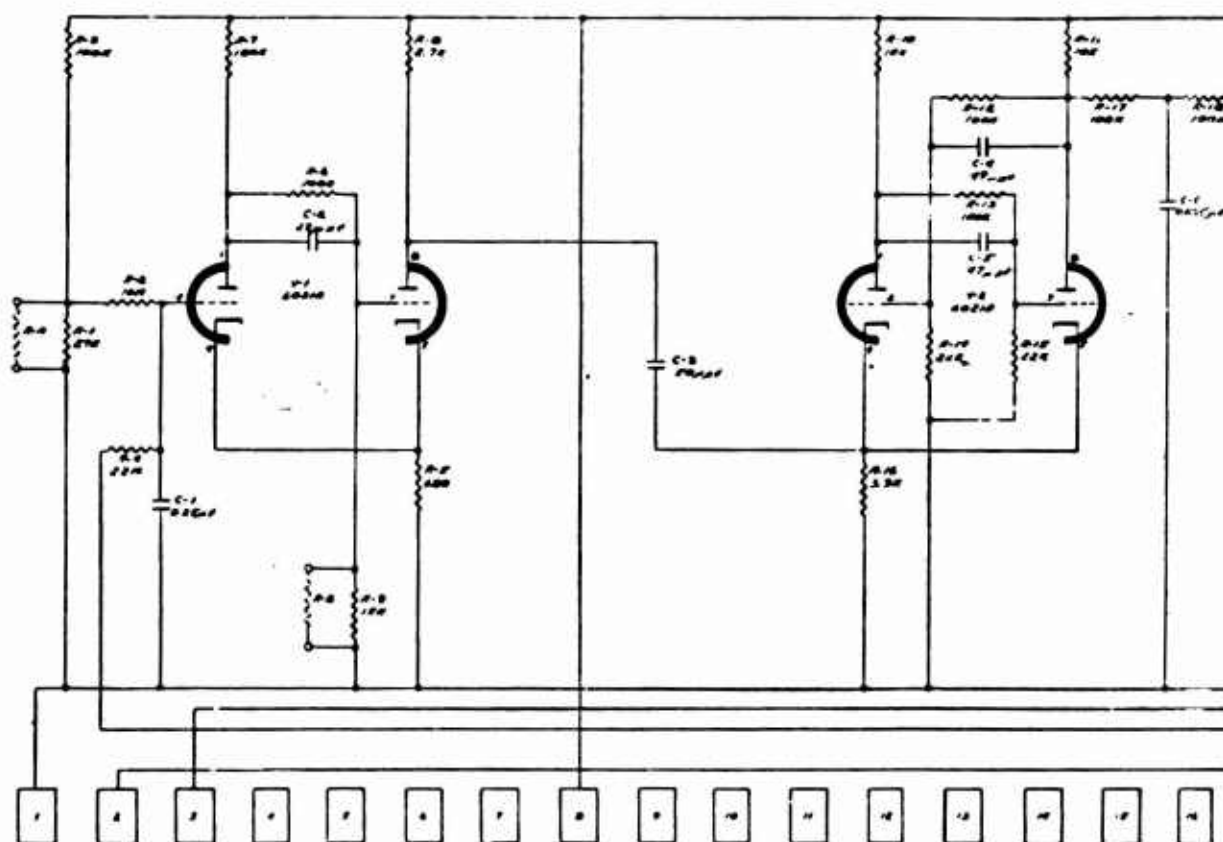


Figure C.12 PCO circuit, low frequency

1

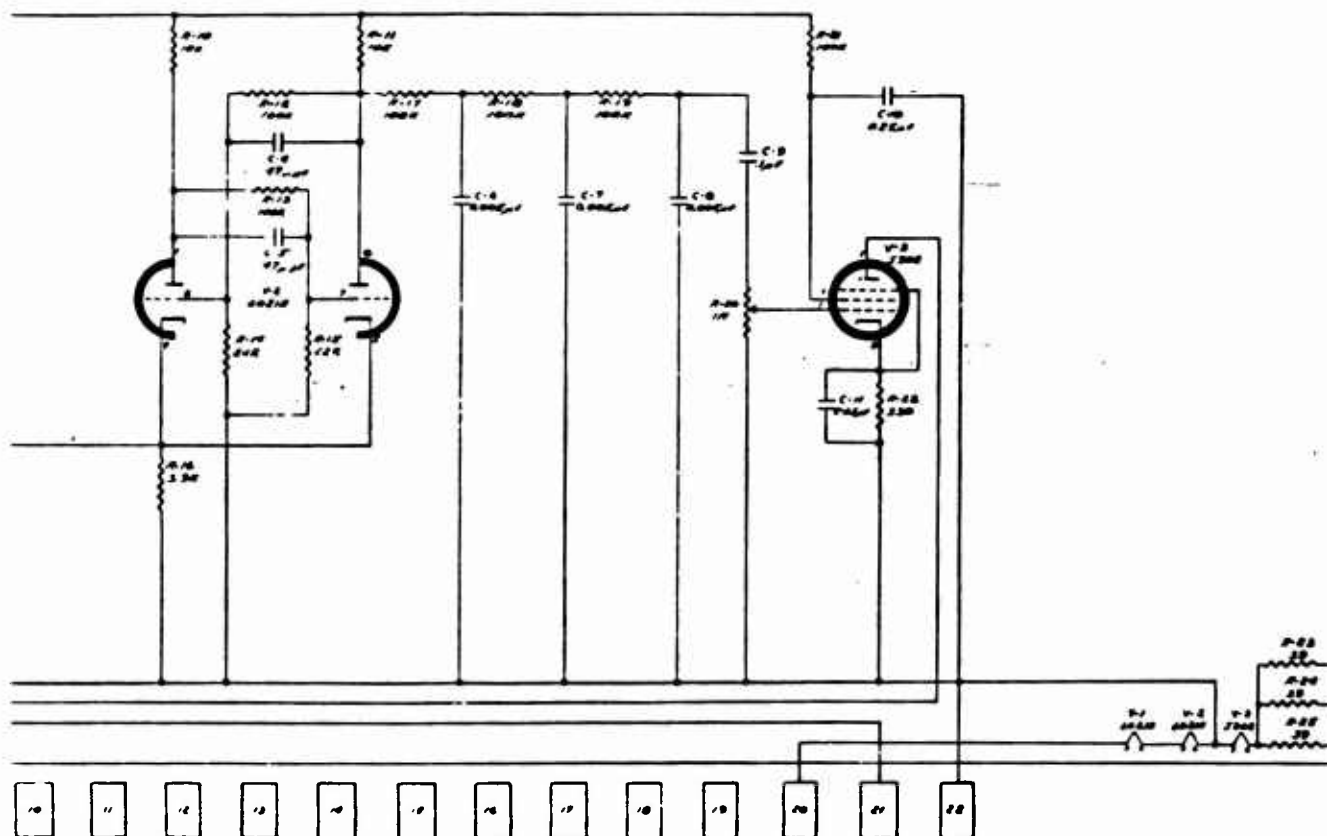


Figure C.12 PCO circuit, low frequency.

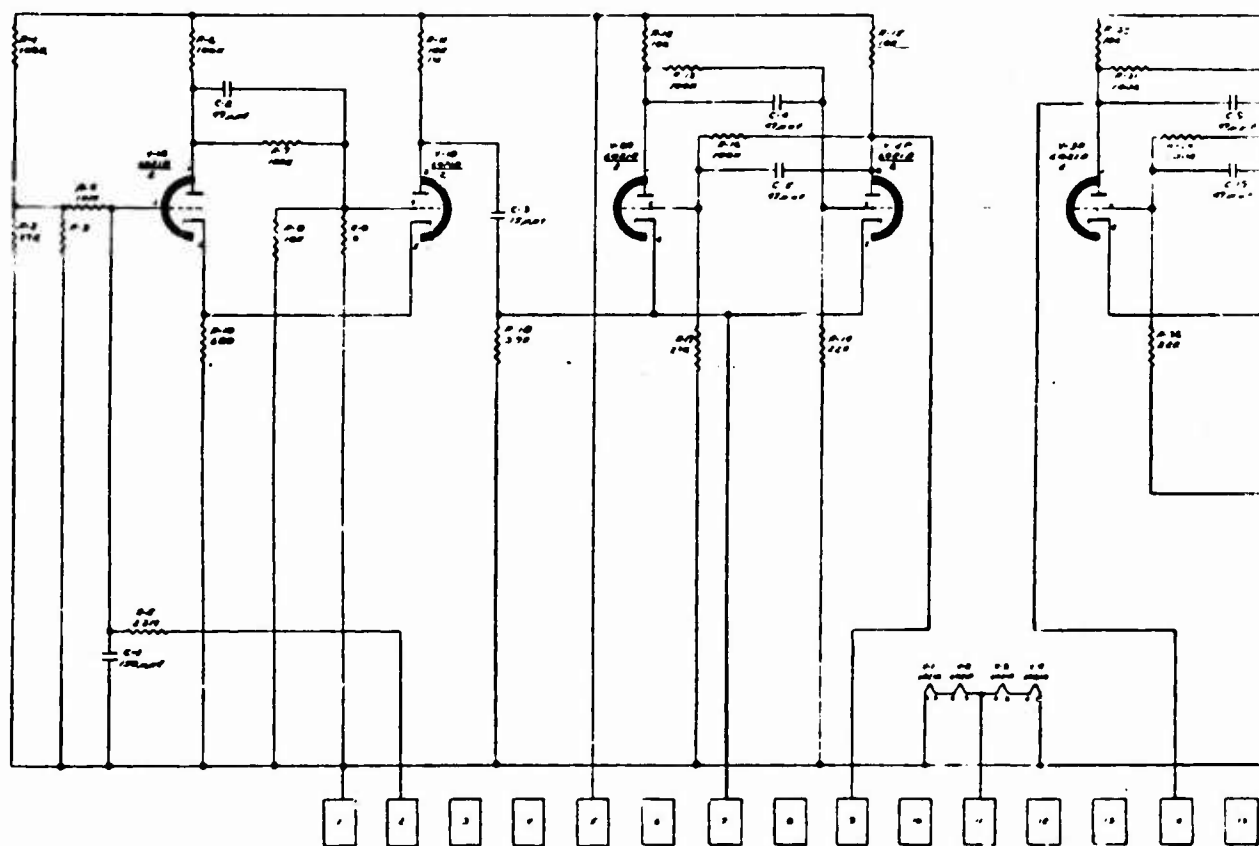


Figure C.13 PCO circuit, high frequency

1

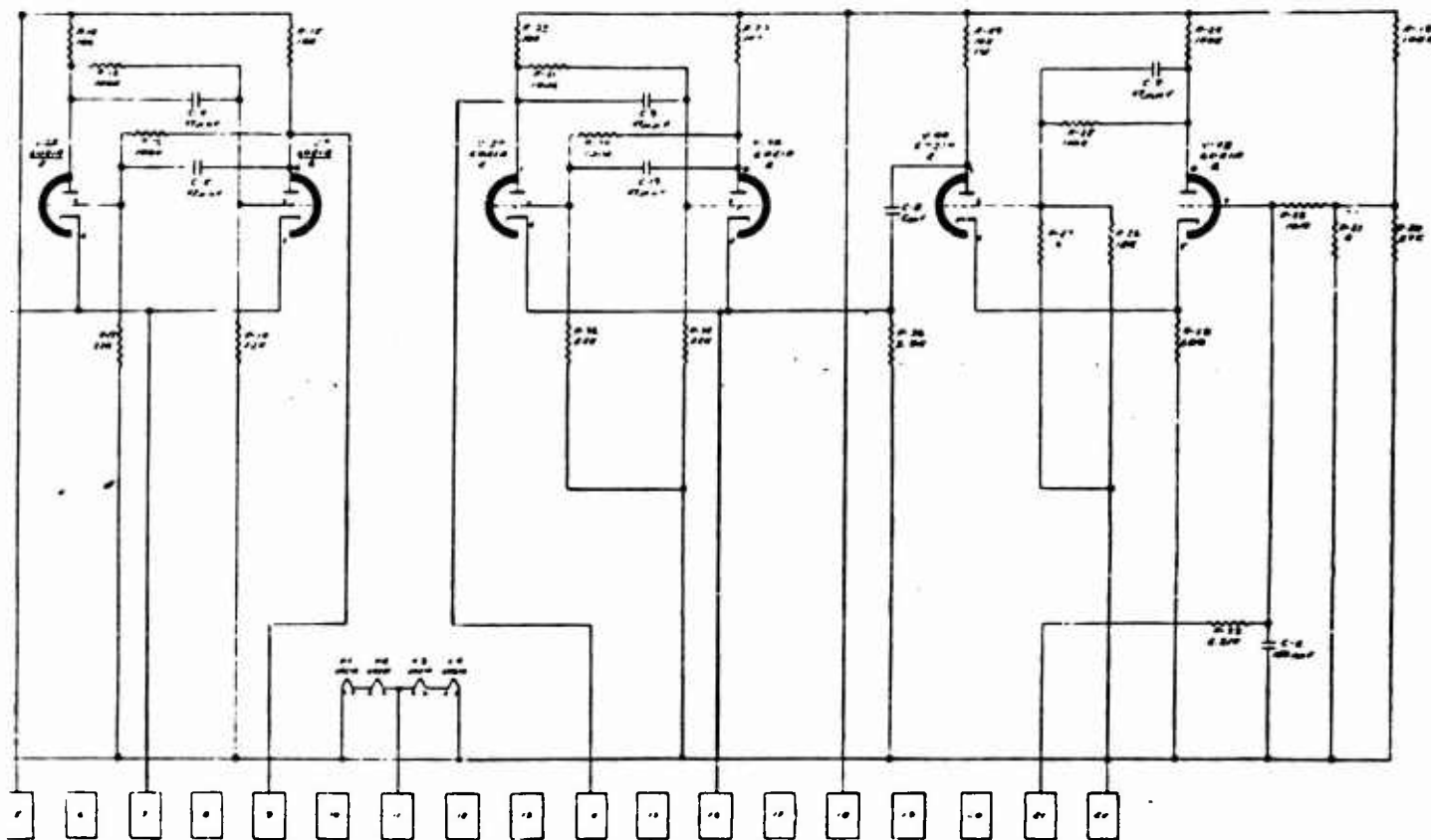


Figure C.13 PCO circuit, high frequency.

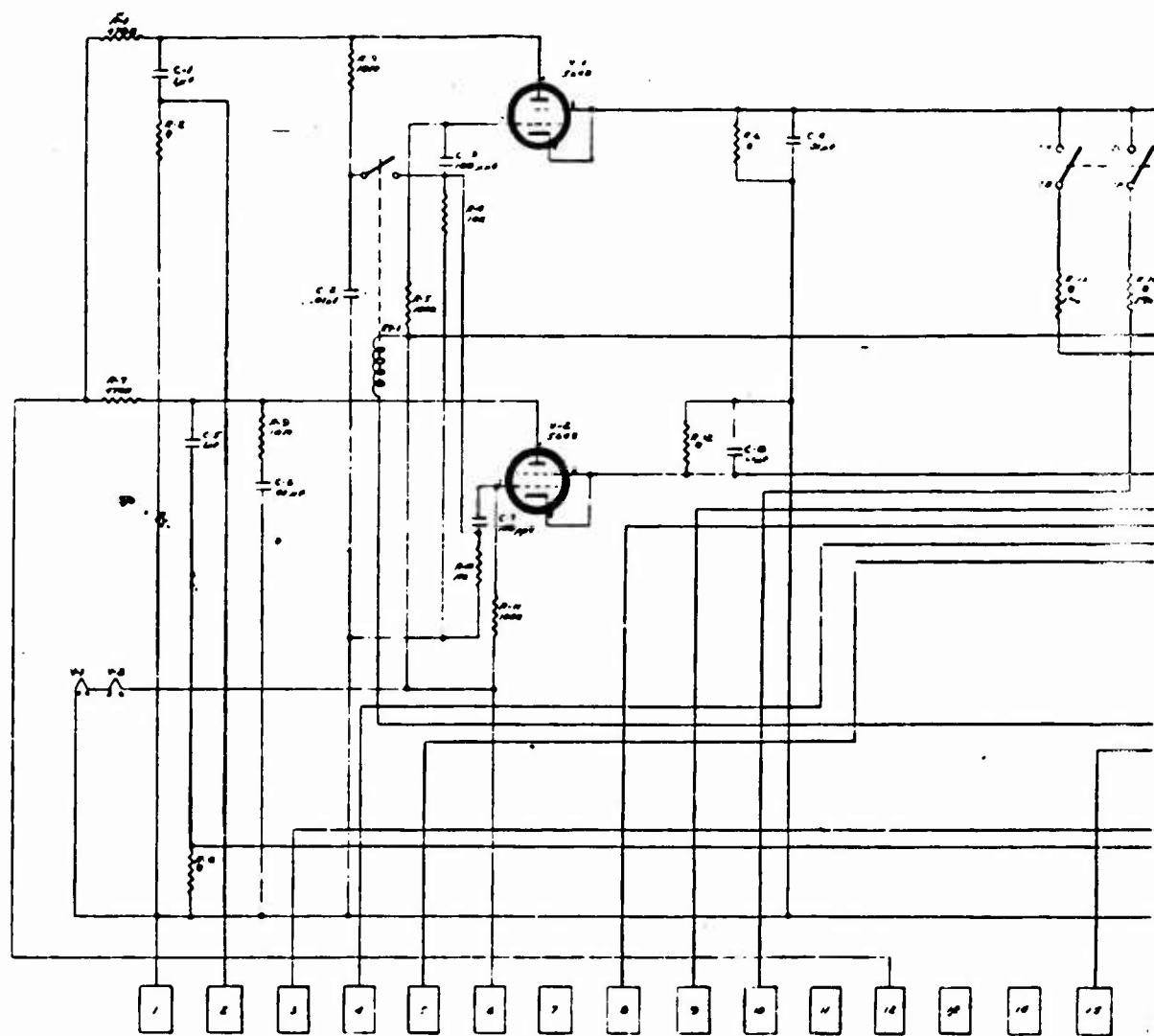


Figure C.14 Calibrator circuit.

1



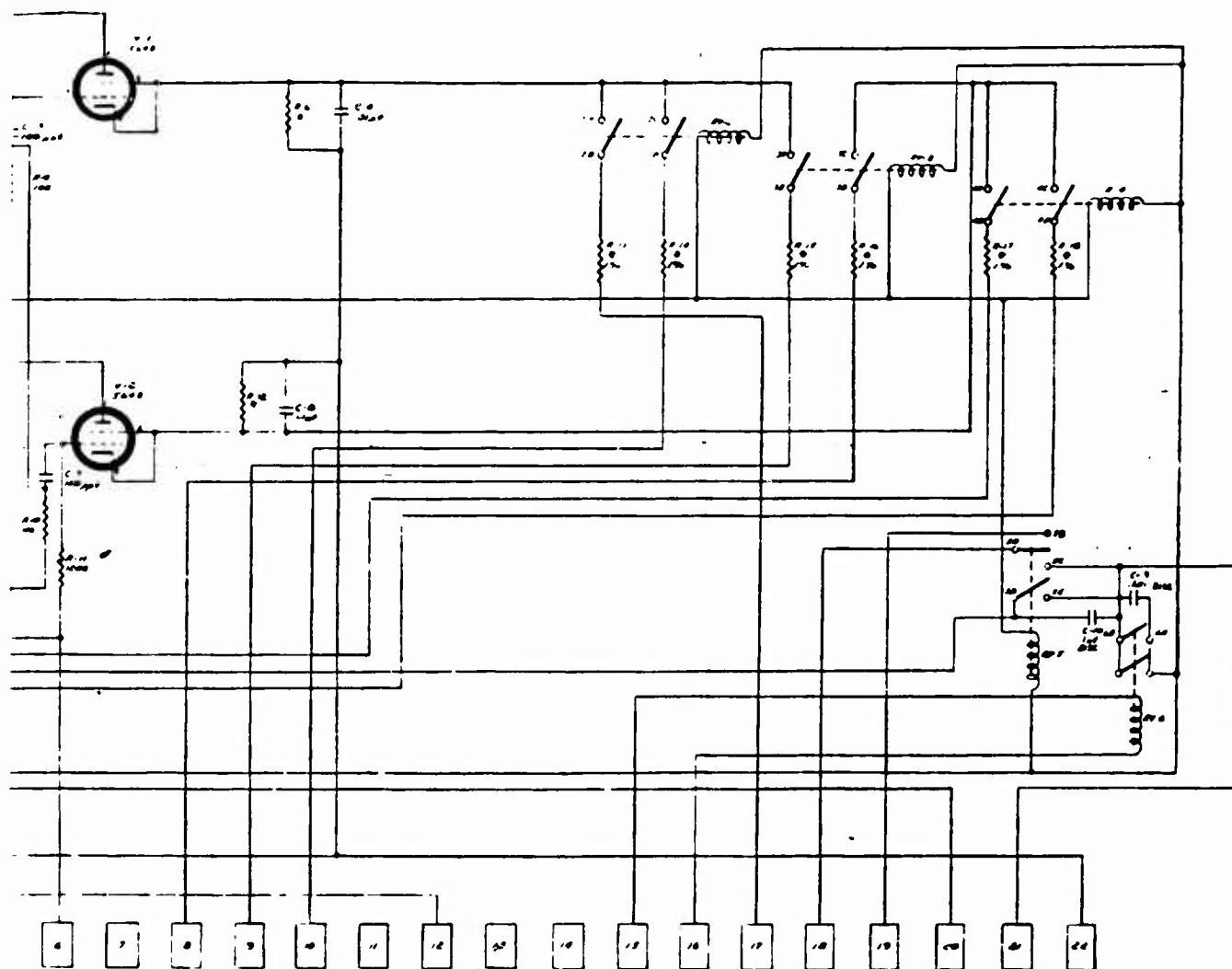


Figure C.14 Calibrator circuit.

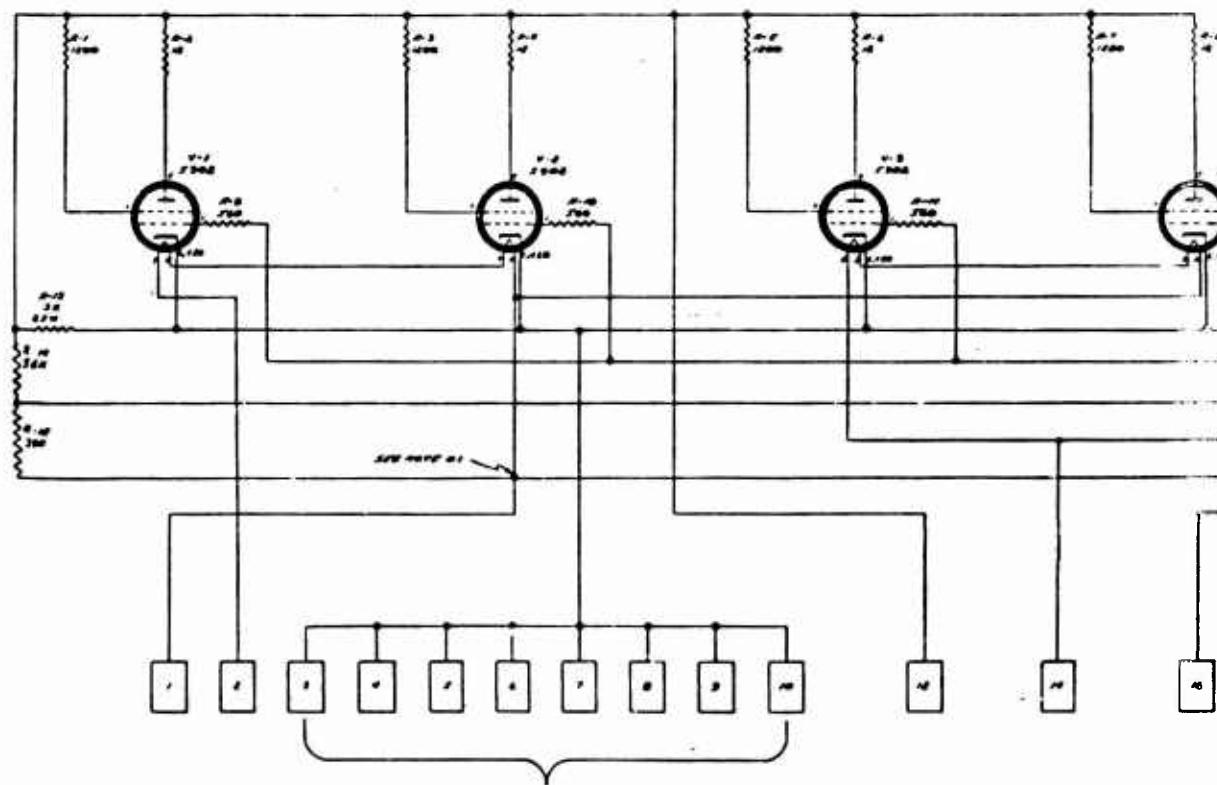


Figure C.15 Voltage regulator.

1

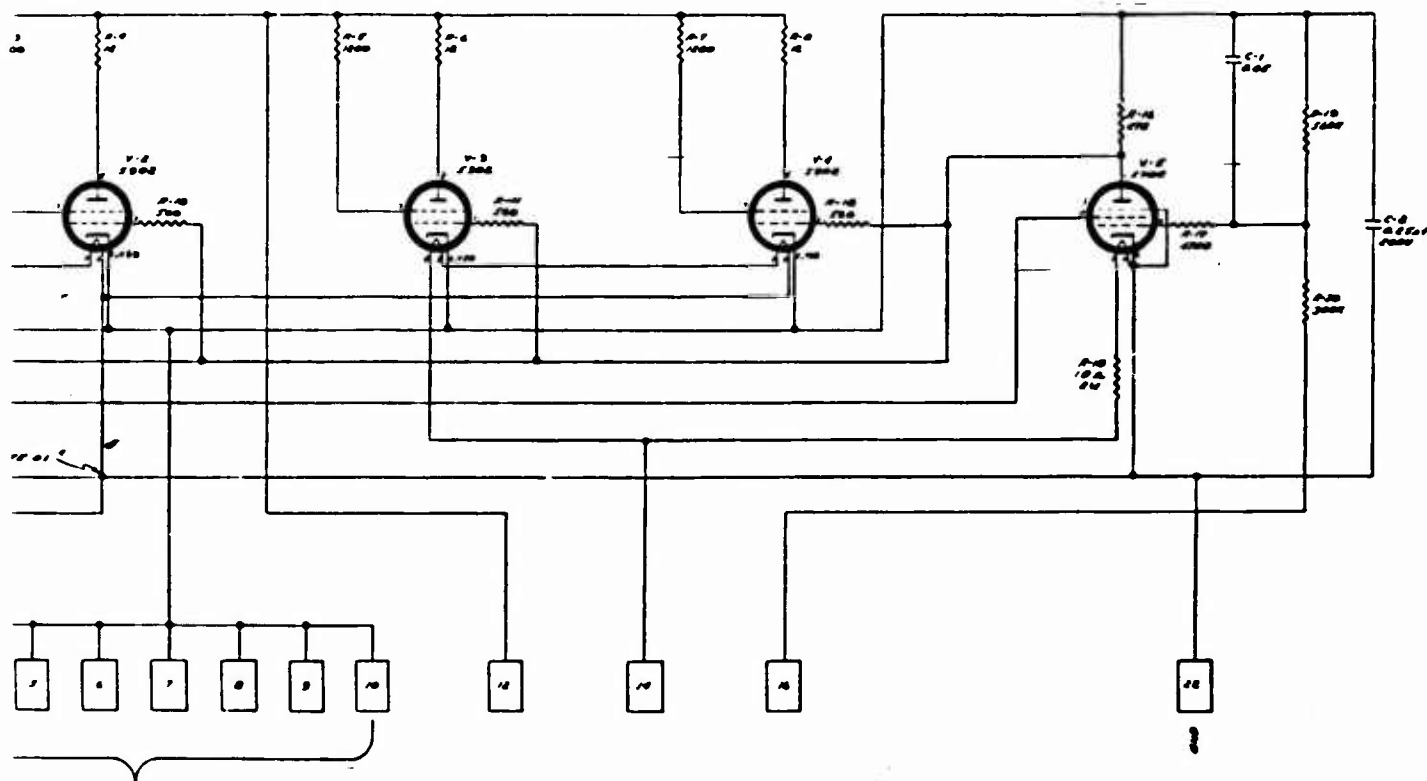


Figure C.15 Voltage regulator.

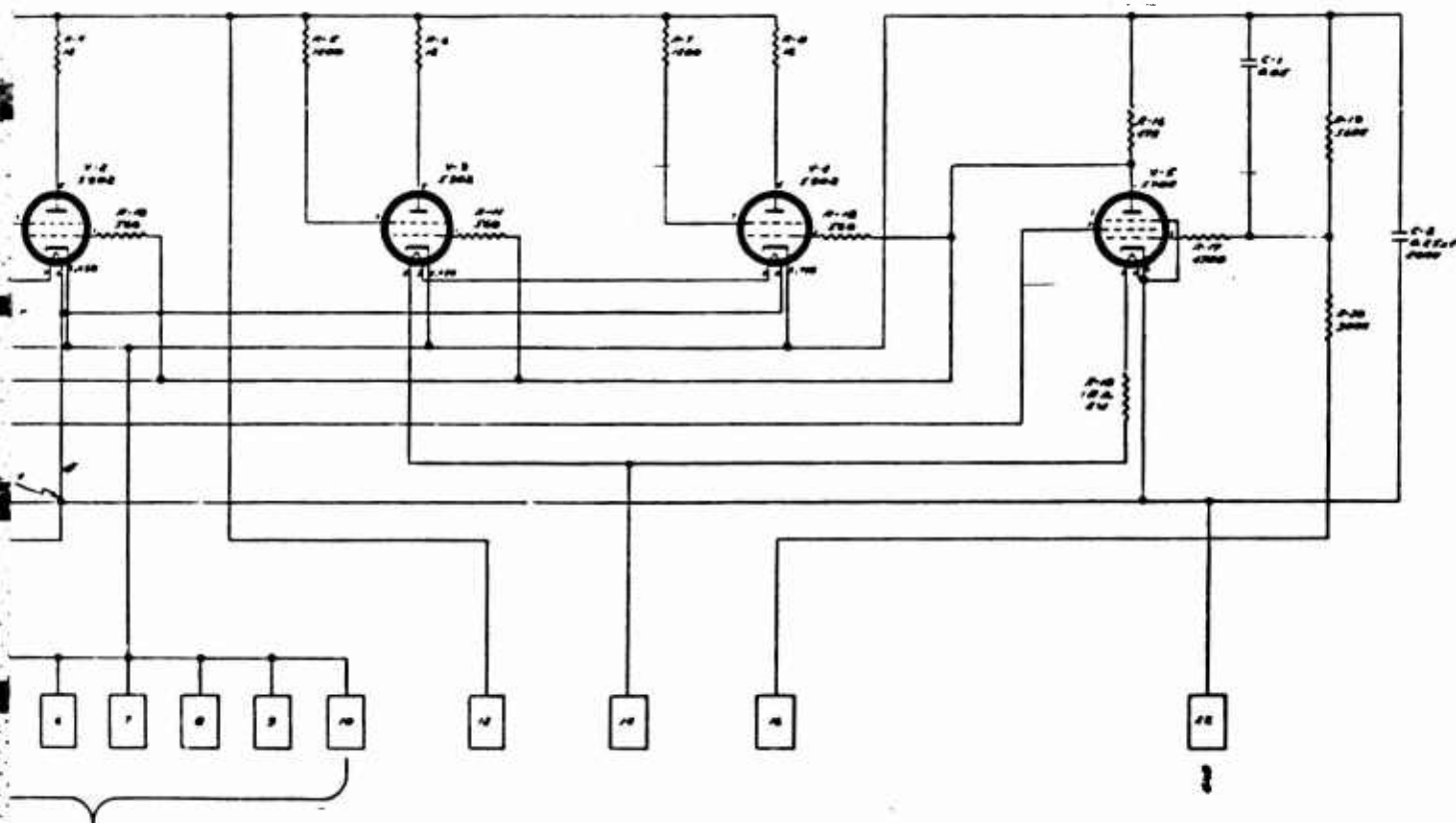


Figure C.15 Voltage regulator.

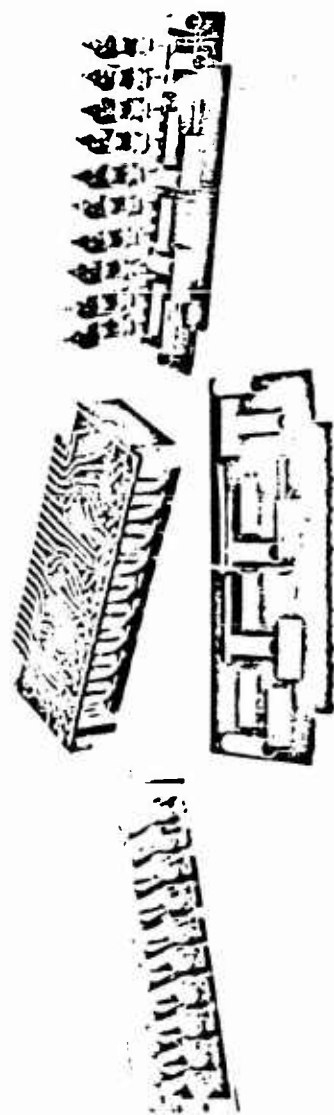


Figure C.16 Log R chassis.

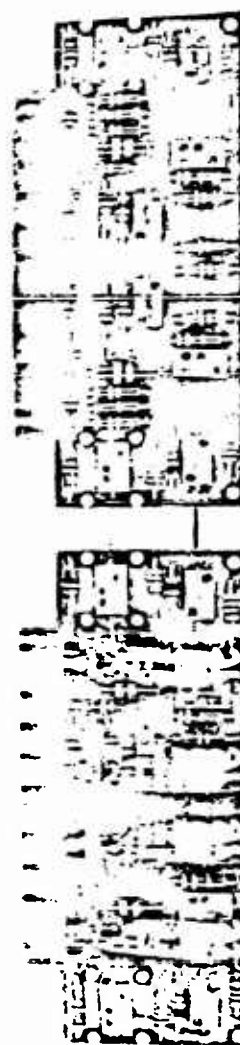
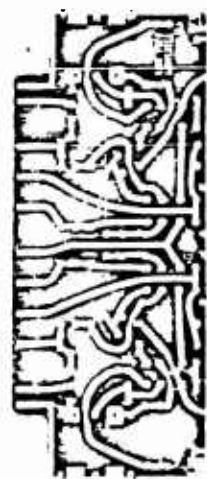


Figure C.17 PCO chassis, high frequency.

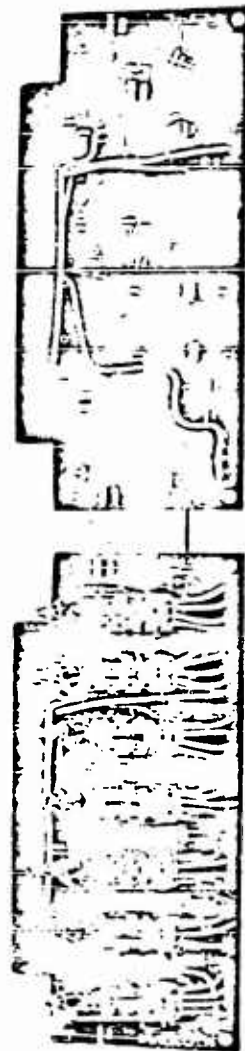


Figure C.18 Timer chassis.

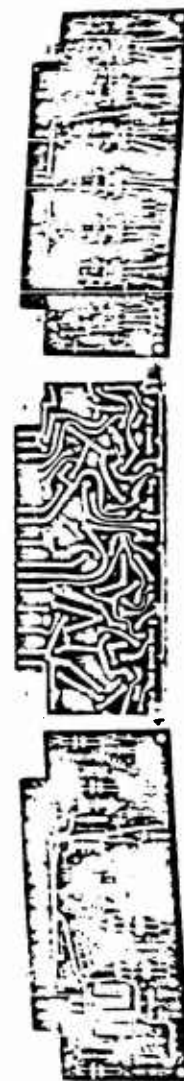


Figure C.19 Timer chassis.

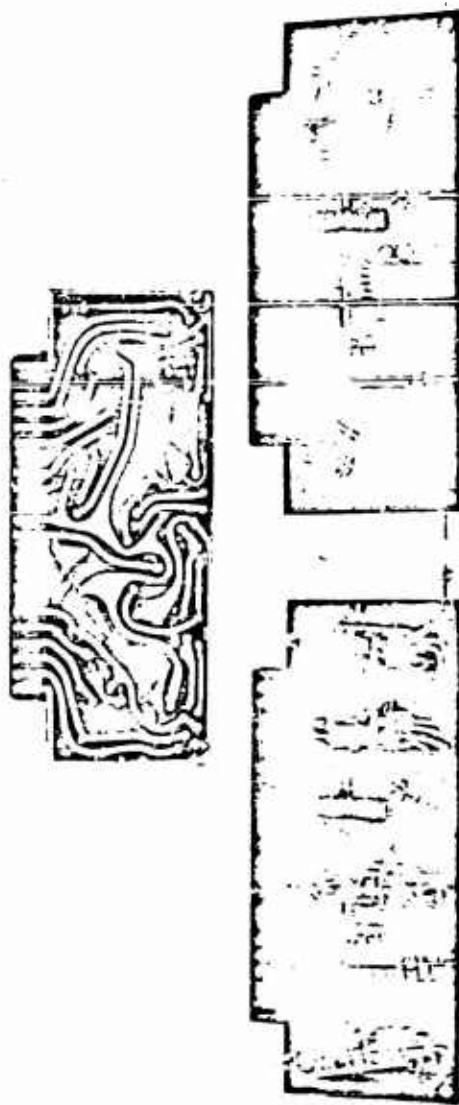


Figure C.20 Peak reader.

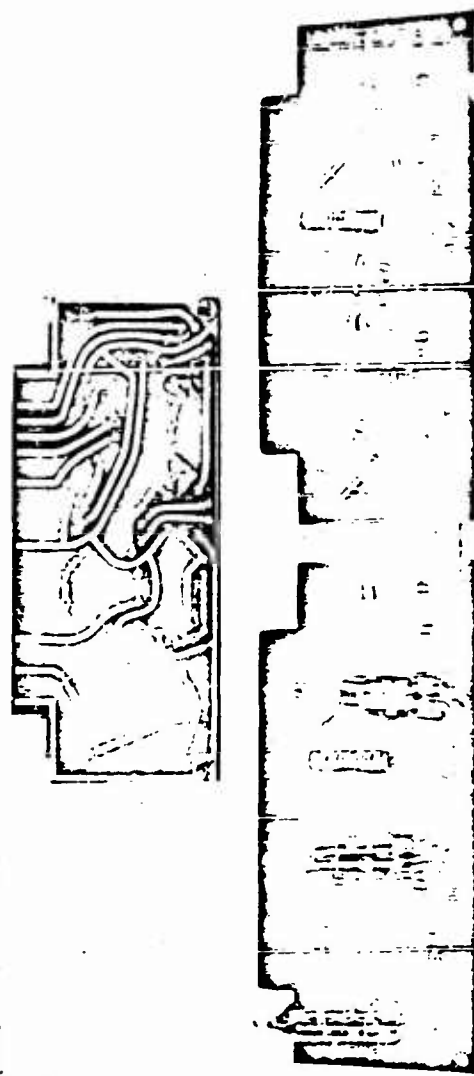


Figure C.21 Peak reader and hold chassis.



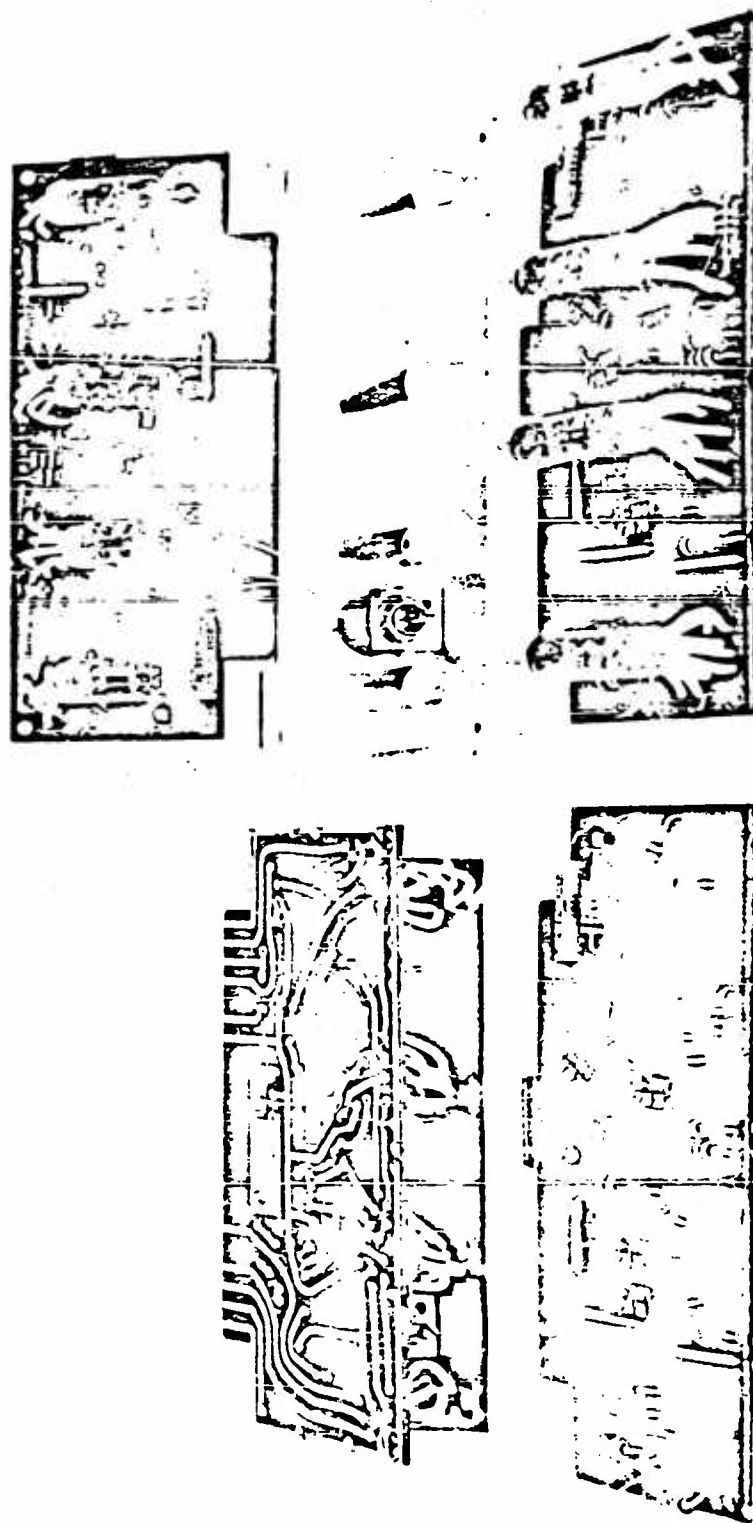


Figure C.23 Integrate and hold chassis.

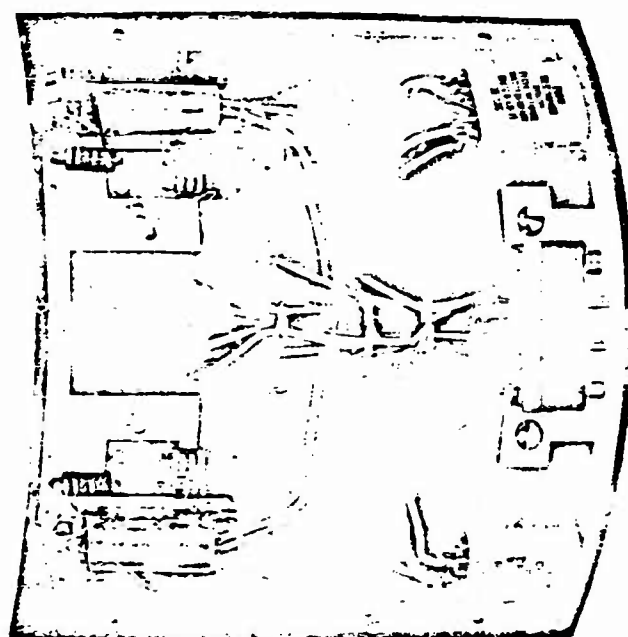


Figure C.23 Detector cathode follower.

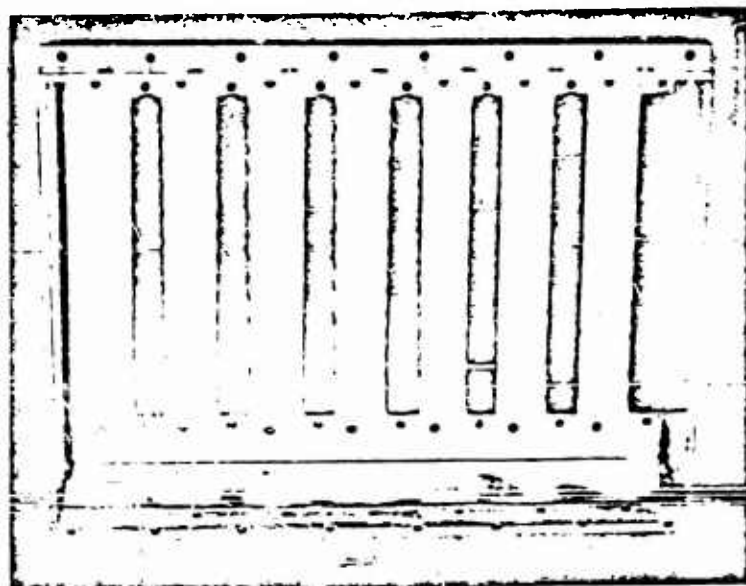


Figure C.24 Pod chassis rack.

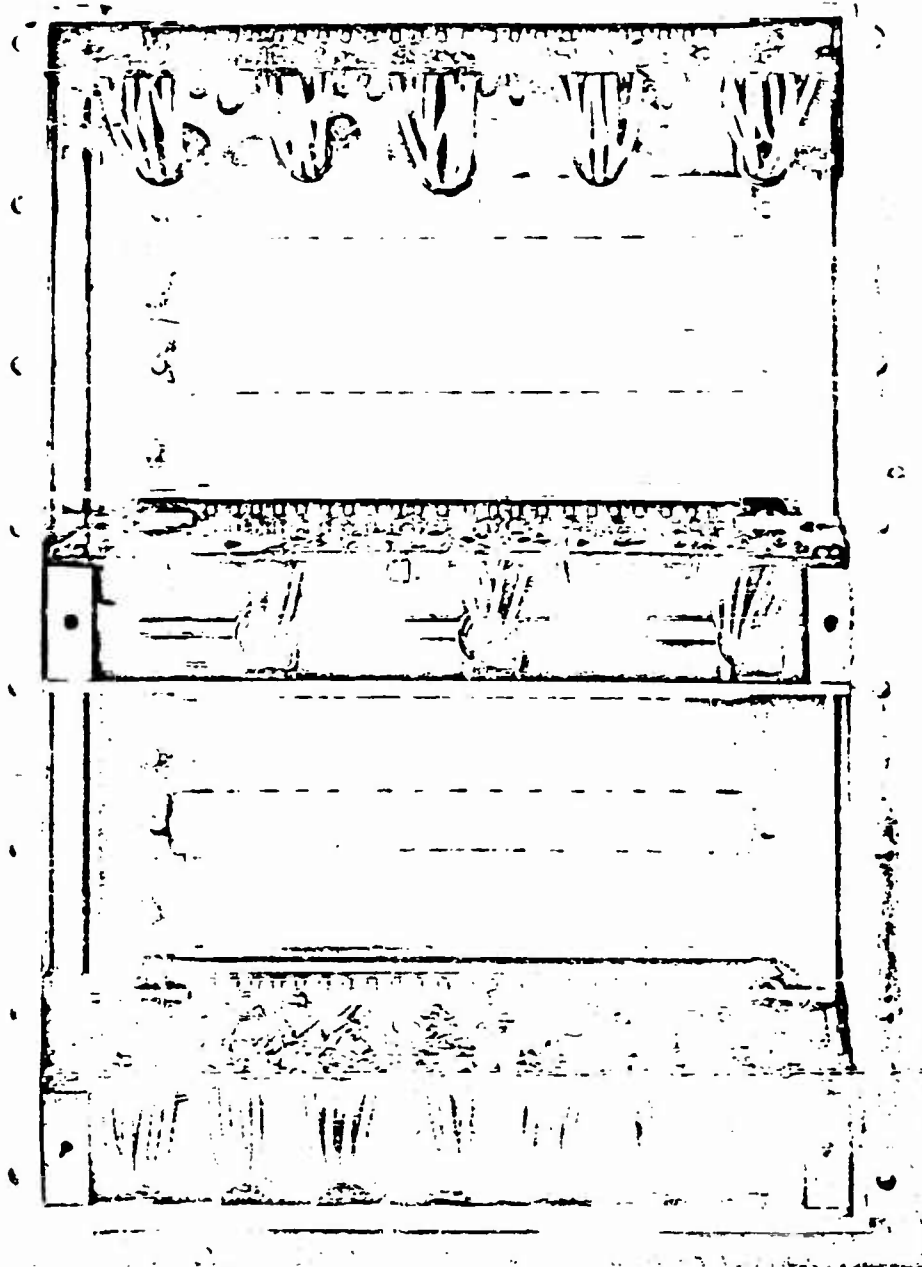


Figure C.25 Pod chassis rack.

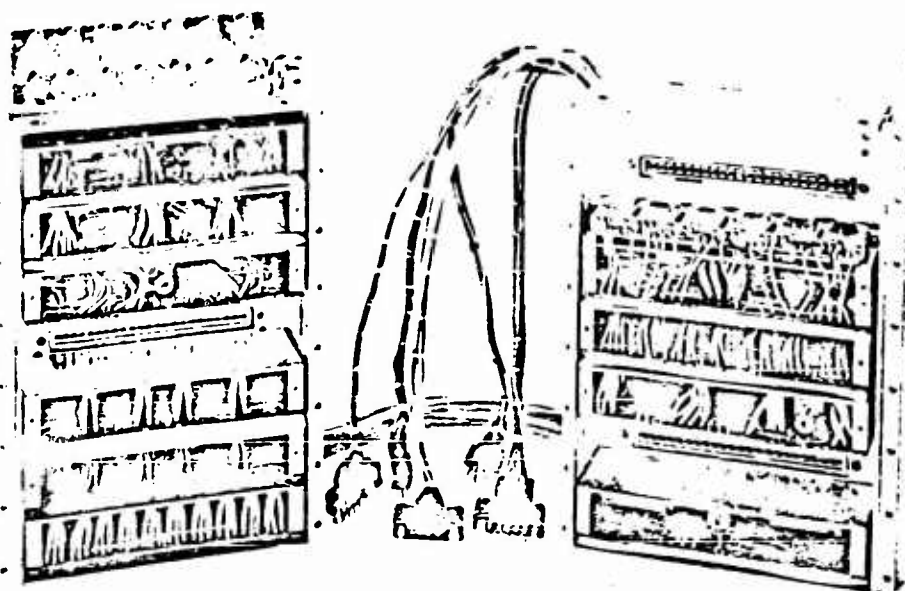


Figure C.26 Completed pod racks, front.

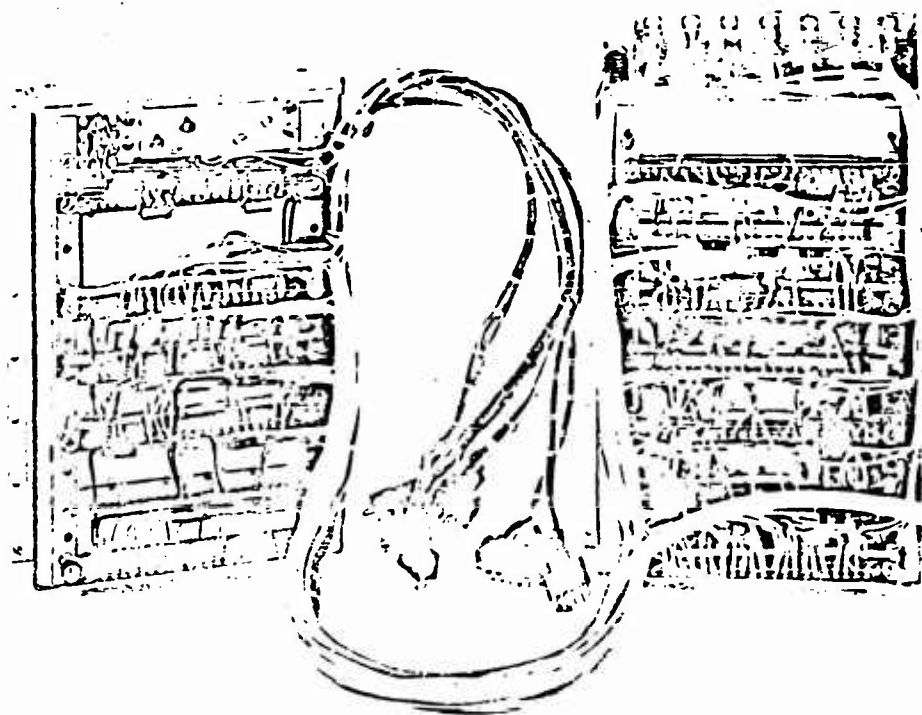


Figure C.27 Completed pod racks, rear.

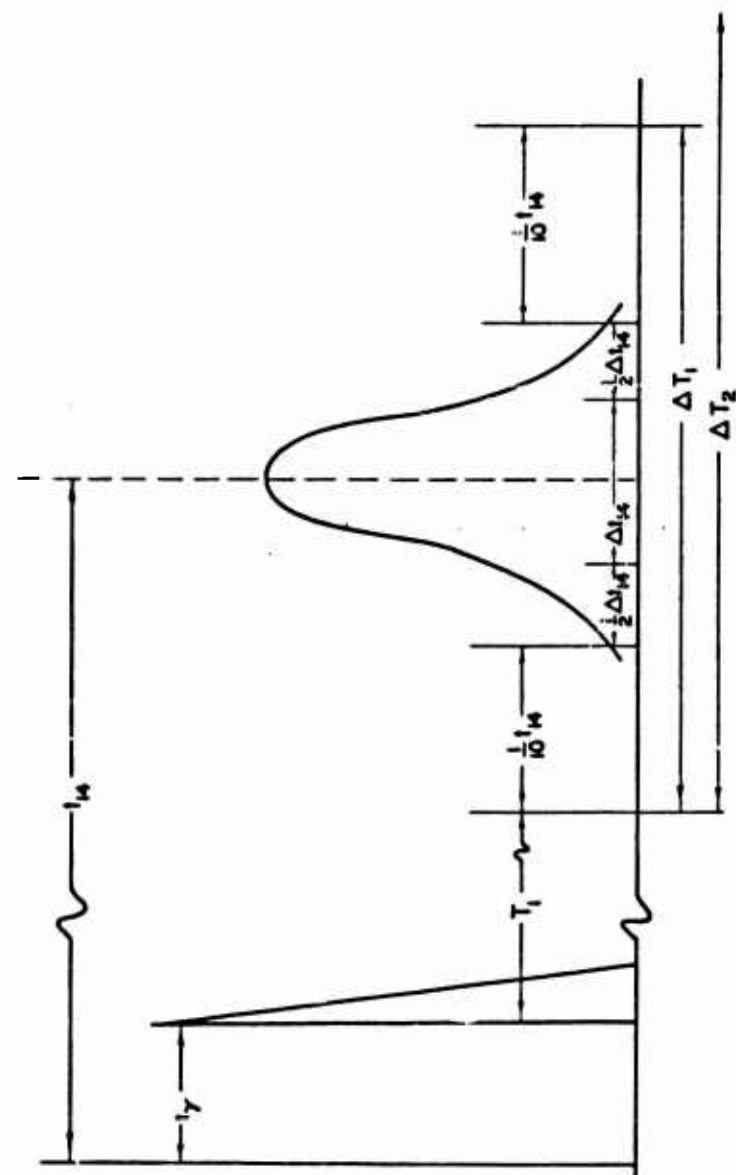


Figure C.28 Definitions of timing values.

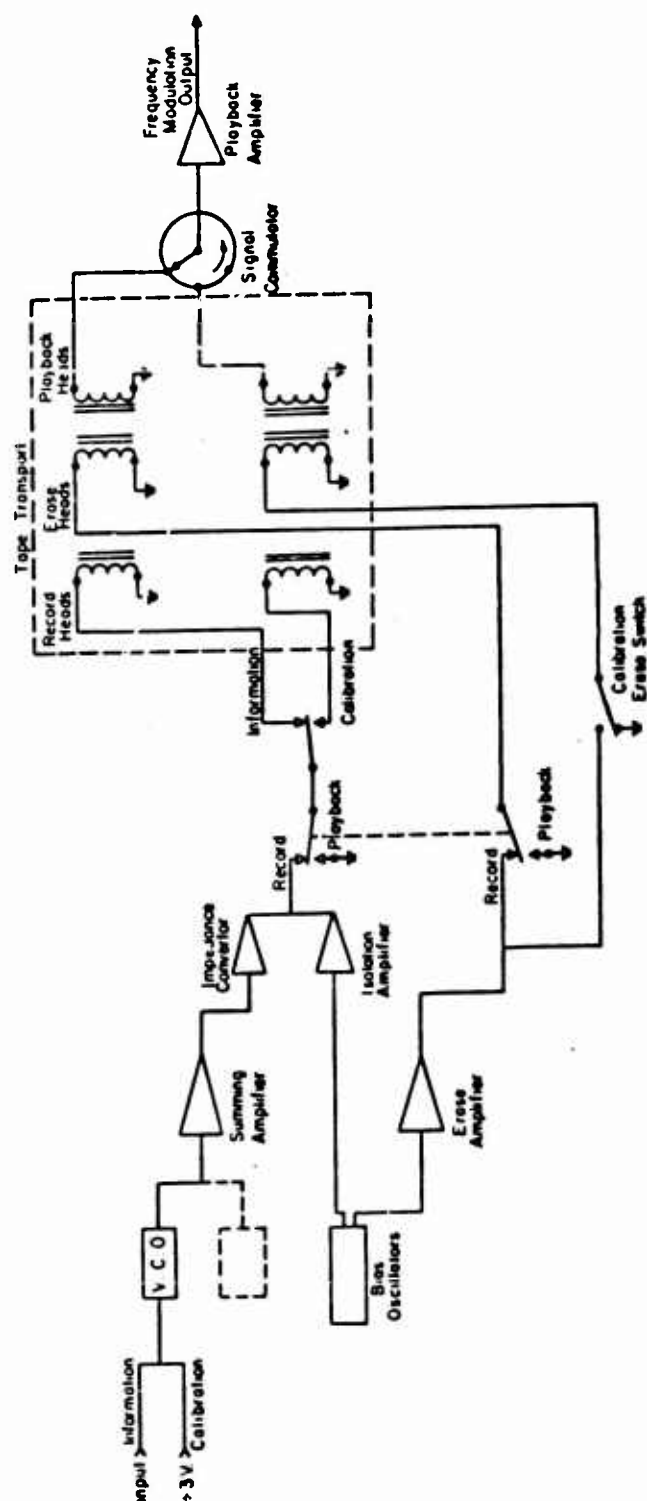


Figure C.29 Block diagram of a frequency channel shown in record mode.

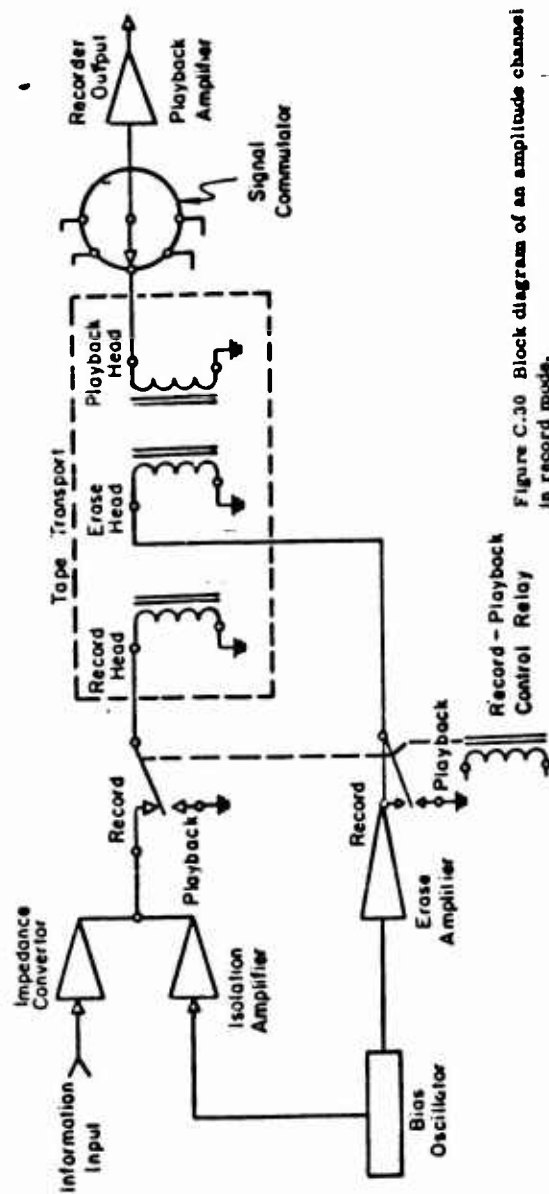


Figure C.30 Block diagram of an amplitude channel in record mode.

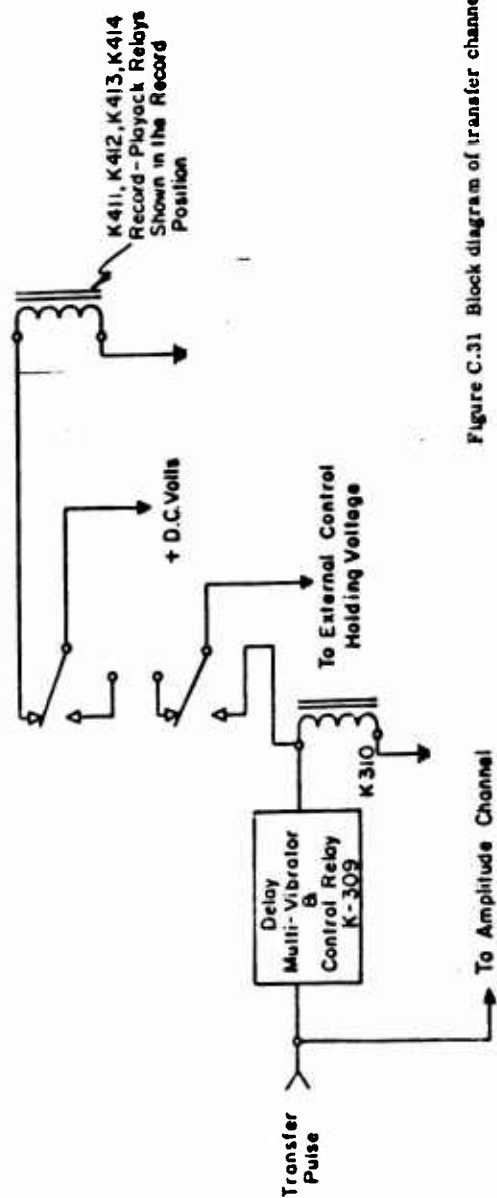


Figure C.31 Block diagram of transfer channel.



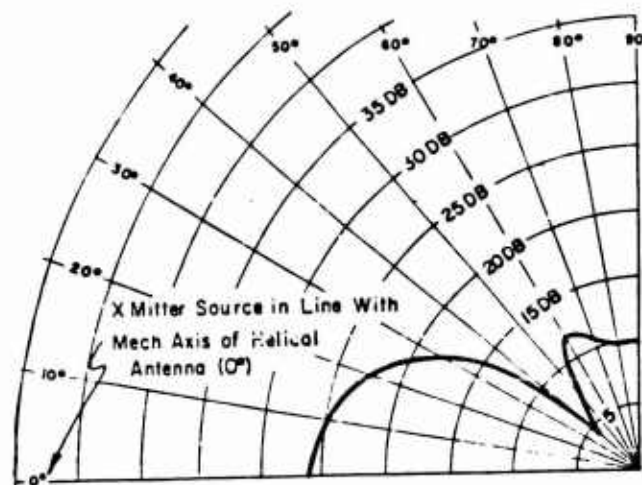


Figure C.32 Field pattern of vertical plane for 4-turn helical telemetering antenna.

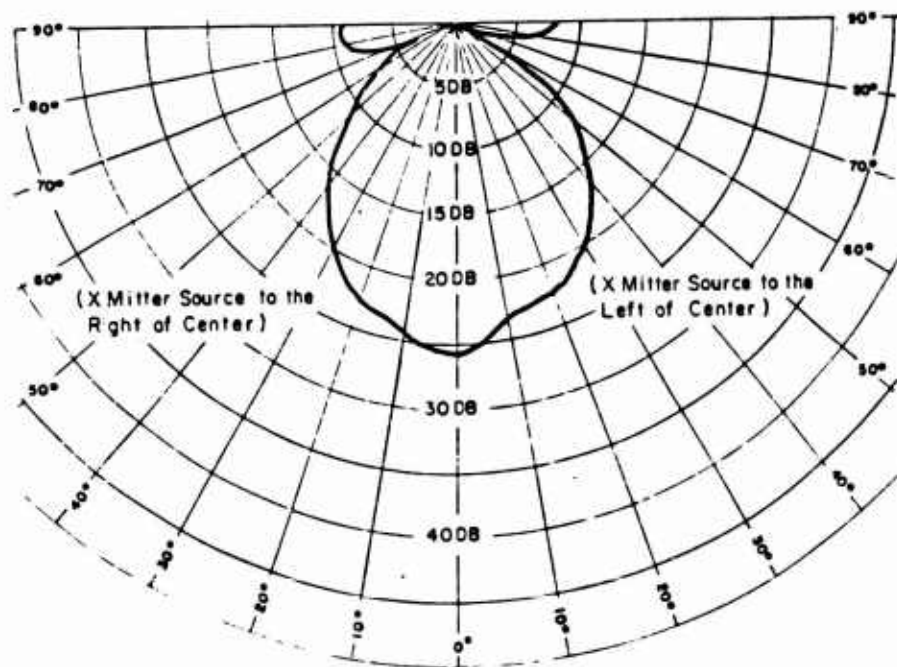


Figure C.33 Horizontal field pattern for 4-turn helical telemetering antenna.

# DATA COLLECTION

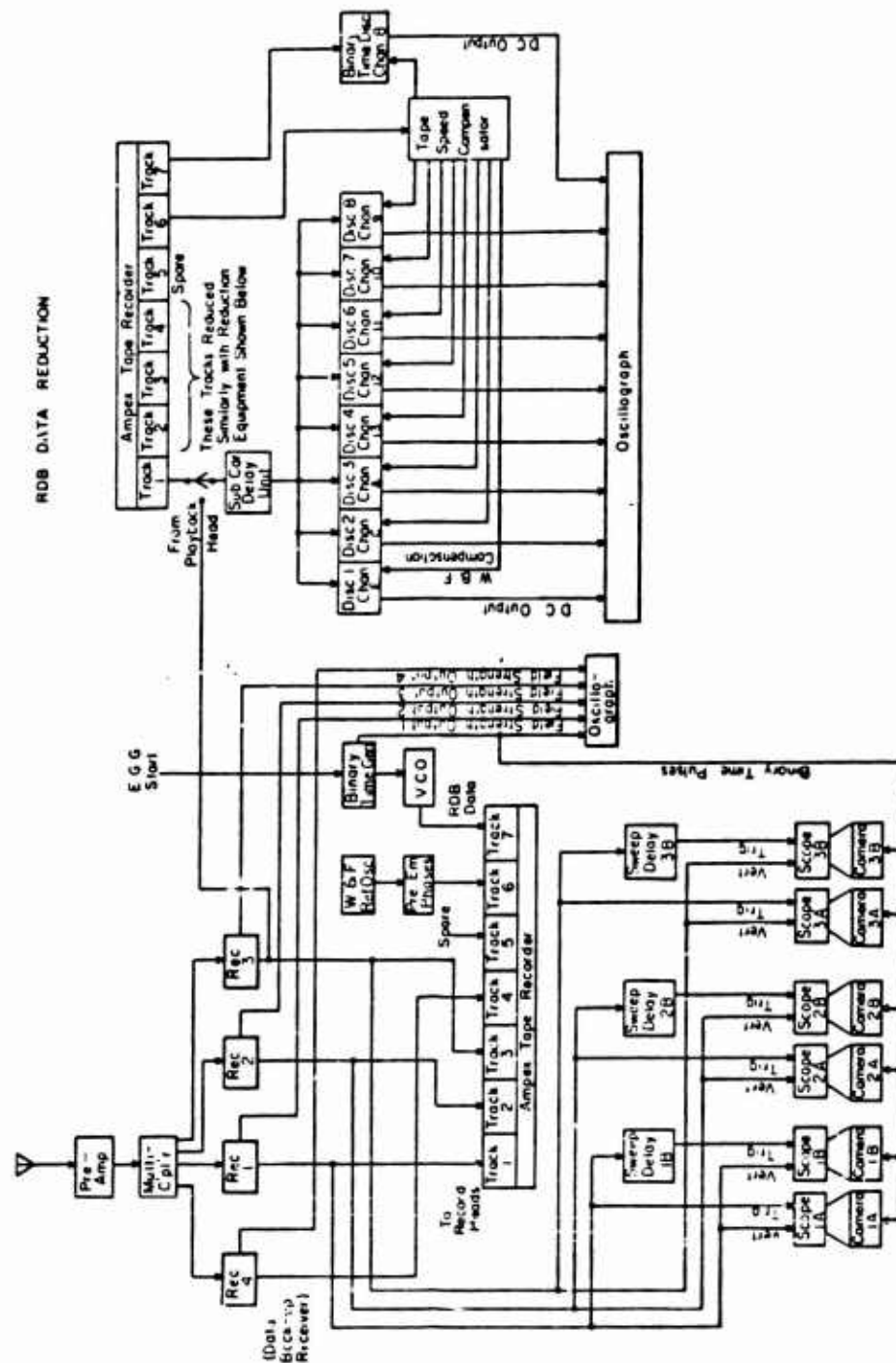


Figure 3.34 Receiving station block diagram.

## Appendix D

### CALIBRATION

The detector signals produced by the nuclear radiations of Shots Teak and Orange passed through an extended chain of instruments. Because the telemetry system required coding of signals so that they could be handled by frequency- and time-sharing techniques, the calibration process was exceedingly complex in practice. Although, in principle, the calibration should be considered for the whole system, practical necessity required that it be broken down into sections. This breakdown led to some overlap. The following discussion covers the significant features of the calibration process. Complete details are given in Reference 17.

The detector calibration, which gives output current per neutron per unit time as a function of time of arrival, is covered separately in Appendix B. This calibration was the most important from the point of view of system design.

The calibration of the detector electronics was a part of the final pod preparation procedure. Figure D.1 is a photograph of a portion of the equipment designed for this purpose. The electronics calibration is discussed in some detail in Section D.1.

The calibration of the tape recorder was interior to the electronics calibration system, but because it had to be precalibrated before it was integrated, it is discussed separately below.

The data-reduction equipment calibration involved standard equipment techniques which were modified as necessary to suit unique requirements of the pod data system.

#### D.1 POD CALIBRATION

The calibration procedure for the pod electronics was designed as a part of the final check procedure. The process for a typical pod is described below.

**D.1.1 Log-R Calibration.** It was found experimentally that the Log-R calibration could be calculated from circuit parameters. The purpose of final calibration was to determine accurately the bias-voltage taps and to check for faults by observing with a scope the drop in signal amplitude as each bias tap was grounded. The calibration (voltage-current relation) for the Log-R was a series of straight-line segments on a graph of Log-R output voltage as ordinate versus Log-R input current as abscissa. The points at the junction of the straight sections were determined at calibration by measurement of applied voltage at the bias taps. Table D.1 depicts a typical series of points for Detector 2A in Pod 2B.

The five sections of the Log-R calibration were plotted on separate graphs for ease in data reduction. Figure D.2 is a plot of the example shown.

**D.1.2 CSI Integrator Calibration.** The calibration of the CSI gamma-ray integral channel required a relation between the charge collected on a condenser and the frequency deviation of a VCO that resulted. To secure this relation, a square pulse of amplitude  $V$  and duration  $t$  was applied to the integrating network. The amplitude of the peak reader-circuit output pulse was measured with a scope. A constant voltage, equal to the amplitude of the peak reader output pulse, was applied to the VCO and its frequency measured. This was done for several values of square wave of amplitude  $V$ . Then  $q = [Vt, R_1] [1 + (R_1/R)]$  was plotted versus the VCO frequency, where  $R_1$  and  $R$  were the integrating network resistors, and  $q$  the quantity of electricity on the condenser.

D.1.3 Pilot B, Detector 2B, Calibration for Total Dose in the Real-Time Channel. The real-time-dose integral channel was calibrated by applying measured voltages  $V$  to the channel input and by counting the PCO pulses  $N$  that occurred in the time  $t$ . The calibration consisted of the graph of current  $I = V/R_g$  versus  $f = N/t$ , where  $R_g$  was the input circuit resistance to ground, 640 ohms.

D.1.4 Pilot B, Detector 2B, Fast-Neutron Integral Channel. The calibration of this channel required a three-channel pulse generator (NRL design) and an external-delay generator in order to trigger the internal timing circuit and to apply the calibration pulse during the pedestal time. When this pulse was properly applied, the calibration calculations were identical with those of Section D.1.2, except that  $q = Vt/R$  was plotted versus  $f$ , the VCO frequency.

D.1.5 Pilot B, Detector 2B, Fast-Neutron Peak-Reader Calibration. The calibration of this channel was the same as that described in Section D.1.2, except that the Log-R circuit was disconnected and the pulse amplitude was plotted against the VCO frequency. The amplitude  $V$  represented the output of a Log-R circuit; therefore, for complete calibration the data had to be combined with the associated Log-R determination.

D.1.6 Pilot B, Detector 2A, Calibration for the Radiation Time History PCO Channel. With the Log-R circuit disconnected, measured voltages  $V$  were applied at the detector terminals, and PCO frequencies were measured. The plot of  $V$  versus  $f$  was combined with the calibration of the associated Log-R circuit for the complete channel calibration.

D.1.7 Pilot B, Detector 2A, Calibration for the Radiation Time History VCO Channel. With the Log-R circuit disconnected, the VCO frequencies resulting from applied voltages  $V$  were measured. The data, combined with the calibration of the associated Log-R circuit, constituted the channel calibration.

D.1.8 Pilot B, Detector 2A, Fast-Neutron Analog Record Channel. With the Log-R circuit disconnected, the delay generator and three-channel pulse generator were used to produce a scope presentation of a pulse presented for recording. Rise time, linearity, and overload levels were observed. Because the amplitude of this pulse was normalized to the peak-reader data, an amplitude calibration was not made.

D.1.9 Li<sup>6</sup>I, Detector 3, LiI, Detector 4, and Blank Detector 5. Each of these detectors provided a signal to three channels. Each set of three channels was calibrated as described in Sections D.1.6 through D.1.8.

D.1.10 Potassium Bromide, Detector 6, Gamma-Ray Integral Channel. This channel was calibrated by applying several measured currents in the range from 0 to 3  $\mu$ a to the detector lead and observing the VCO frequencies. The calibration was a plot of  $I$  versus  $f$ .

## D.2 RECORDER CALIBRATION

The coded detector signals presented to the data-recorder system were limited, i.e., a circuit was included in each channel to prevent signals from exceeding a predetermined amplitude. The recorder system was prepared for the calibrations described above by making and checking critical adjustments of VCO sensitivity, tape speed, tape pad pressure, internal program multivibrators, and output-signal amplitudes.

D.2.1 VCO-Sensitivity Adjustment. The input to the VCO channels designed for  $\pm 7\frac{1}{2}$ -percent frequency deviation was limited to 3 volts; the input to VCO channels designed for  $\pm 15$ -percent frequency deviation was limited to 5 volts. Each VCO sensitivity was adjusted to produce a de-

viations slightly less than these design limits. Variations greater than these amounts lead to cross-talk between channels and the loss of data.

**D.2.2 VCO-Output-Signal-Amplitude Adjustment.** The output voltage from each VCO was adjusted to a value dictated by the frequency response of the telemeter transmitter. The low- and high-frequency VCO's were required to produce greater output than the midfrequency VCO's in order to give uniform response through the transmitter.

**D.2.3 Tape-Pressure-Pad Adjustment.** The output amplitude and signal-to-noise ratio of recorded signals depended critically on the pressure with which the tape was held against the record and playback heads. The pad pressure was adjusted to give the best signal-to-noise ratio compatible with tape wear and tension.

**D.2.4 Tape-Speed Adjustment.** After the pressure adjustment was made, the tape speed was set at 60 in./sec by setting the motor-speed governor control.

### D.3 DATA-REDUCTION CALIBRATION

The data coding was designed, wherever possible, to be independent of receiving-station settings. A coarse time scale (binary time record) was impressed on the data record. This time scale was recorded as a time code every 0.1 second. All other time records were a part of the received data, e. g., the 100-kc component in the RDB complex provided a time scale by indicating tape speed during playback. The calibration of recording devices was made for each playback of the data record. This calibration consisted primarily of choosing the proper oscillograph paper speed, galvanometer response, and sensitivity.

### D.4 IN-FLIGHT SYSTEM CHECKOUT

In addition to the preflight calibration described above, provisions were made in each pod to simulate signal inputs in all channels. This was done with a condenser-thyratron two-tube pulser fired at the end of the 5-second delay squib that was ignited at pod ejection. This system provided pulses to all channels and initiated the timing sequence so that any deviations from the preflight condition could be observed.

TABLE D.1 GRAPHING POINTS FOR LOG-R CALIBRATION

Denominators in the calculations of the current are the measured Log-R resistance values for each straight section of the response (Section D.1.1).

Point	V, Volts Measured	I, Current Calculated in ma
1	0	0
2	$V_{15} = 14.85$	$I_{15} = \frac{V_{15}}{36,200} = 0.41 \text{ ma}$
3	$V_{30} = 29.7$	$I_{30} = I_{15} + \frac{V_{30} - V_{15}}{6,360} = 2.57 \text{ ma}$
4	$V_{45} = 44.5$	$I_{45} = I_{30} + \frac{V_{45} - V_{30}}{1,073} = 16.36$
5	$V_{60} = 60.0$	$I_{60} = I_{45} + \frac{V_{60} - V_{45}}{169} = 108.1$

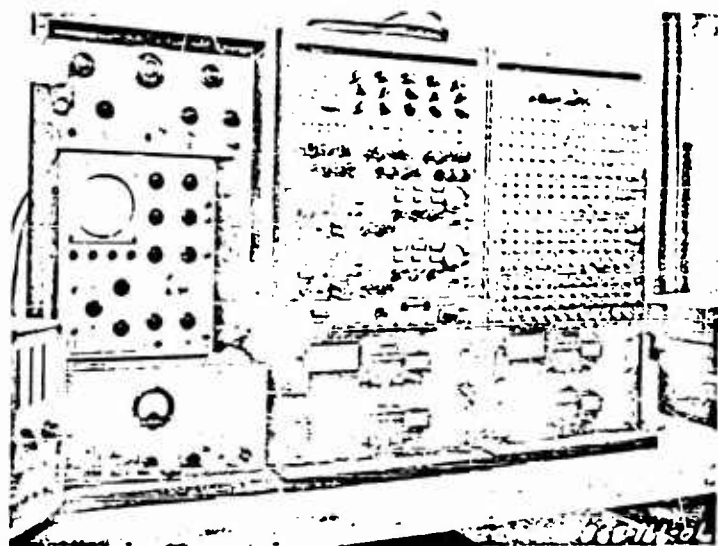


Figure D.1 Calibration equipment.

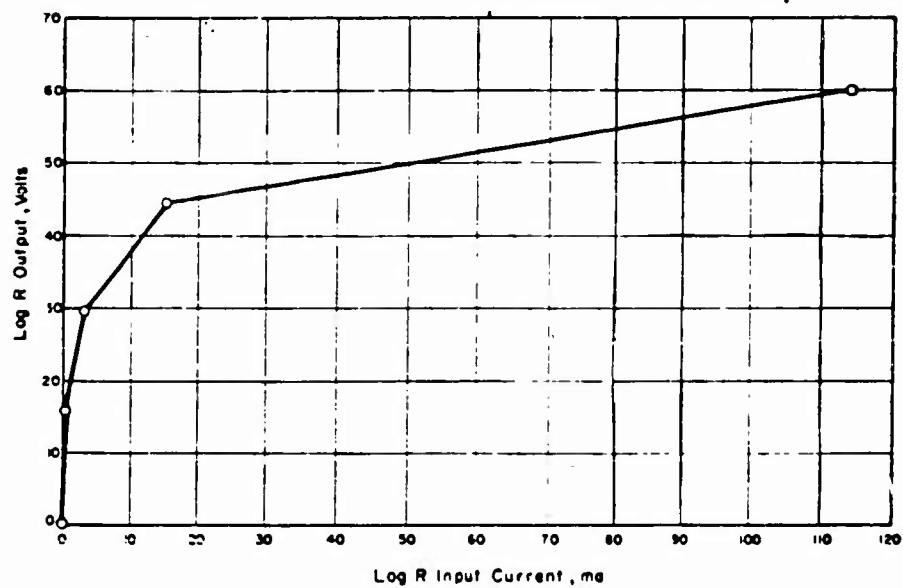


Figure D.2 Log-R calibration curve.

## REFERENCES

1. P. W. Island; "The Relative Importance of Nuclear Radiation from Atomic Weapons Detonated at High Altitudes"; AFSWP-500; Secret Restricted Data.
2. R. C. O'Rourke; "Growth of the Fireball"; NRL Report No. 4997 (AFSWP-857); U. S. Naval Research Laboratory, Washington 25, D. C.; Secret Restricted Data.
3. A. Latter and R. Latter; "Sunlamp Calculations"; RAND Corporation Report No. 1656; The RAND Corporation, Santa Monica, California; Secret Restricted Data.
4. N. A. Haskel, J. A. Fava, and R. M. Brubaker; "Measurement of Free Air Atomic Blast Pressures"; Project 1.1, Operation Teapot, WT-1101, Appendix C, 14 February 1958; Terrestrial Sciences Laboratory, Geophysics Research Directorate, Air Force Cambridge Research Center, Cambridge, Massachusetts; Confidential Formerly Restricted Data.
5. C. W. Dubs and K. H. Sen; "Electron Attachment Coefficient of Oxygen Molecules"; Convair Conference Proceedings ZPH-022, 14 to 16 August 1958; Secret Restricted Data.
6. P. A. Caldwell and others; "Attenuation of Telemetry Frequencies by Nuclear Detonations"; Project 6.6, Operation Redwing, WT-1346, 18 February 1960; U. S. Naval Research Laboratory, Washington 25, D. C.; Secret Restricted Data.
7. L. M. Chanin; "The Attachment of Slow Electrons in Oxygen"; Westinghouse Research Report 403FD317-R2; Unclassified.
8. T. D. Hanscome and others; "Parameters Affecting Design of Instrumentation to Measure Gamma and Neutron Fluxes from a Very-High-Altitude Nuclear Detonation"; Project 2.7, Operation Plumbbob, ITR-1416, 9 April 1959; U. S. Naval Research Laboratory, Washington 25, D. C.; Secret Restricted Data.
9. W. E. Ogle; LASL Report LAB-J-1337, SD-3399, 19 September 1950; Los Alamos Scientific Laboratory, Los Alamos, New Mexico; Secret Restricted Data.
10. B. R. Suydam; "Spectrum of D-T Neutrons"; LASL Report LAB-J-1417, SD-3652, 28 September 1950; Los Alamos Scientific Laboratory, Los Alamos, New Mexico; Secret Restricted Data.
11. A. J. Ruhlig; "The Energy Spectrum of the Products of a Thermal Reaction"; NRL Report No. 3775, RDS 1096, December 1950; U. S. Naval Research Laboratory, Washington 25, D. C.; Unclassified.
12. C. R. Mehl; "Neutron Measurements for Teak and Orange"; Program 32, Operation Hardtack, Sandia Corporation, NRL Report No. 5233, P. 48 (AFSWP-1101), October 1958; U. S. Naval Research Laboratory, Washington 25, D. C.; Secret Restricted Data.
13. M. Annis and C. J. Cosenza; "X-Ray, Thermal, and Neutron Measurements Taken During Teak"; Operation Hardtack, Aircraft Laboratory, Wright Air Development Center, Wright-Patterson Air Force Base, Ohio, NRL Report No. 5233, P. 64 (AFSWP-1101), October 1958; U. S. Naval Research Laboratory, Washington 25, D. C.; Secret Restricted Data.
14. F. I. Keller and C. D. Zerby; "Calibration of Fluxes and Dose Rate Resulting from Neutrons Multiple Scattered in Air"; ORNL-2375, 31 December 1958; Oak Ridge National Laboratory, Oak Ridge, Tennessee; Unclassified.



15. B. E. Watt; Los Alamos Scientific Laboratory, Los Alamos, New Mexico; private communication.

16. R. Lessler and G. Bing; University of California Lawrence Radiation Laboratory, Livermore, California; letter; Secret Restricted Data.

17. R. C. Waddel; "Hardtack Pod Calibration Instructions"; Limited Nucleonics Division Publication available at the U. S. Naval Research Laboratory; Official Use Only.

18. P. A. Caldwell and others; "Nuclear Radiation from a Detonation at Very-High Altitude"; Project 2.7 Operation Hardtack, ITR-1624, 18 July 1958; U. S. Naval Research Laboratory, Washington 25, D. C.; Secret Restricted Data.